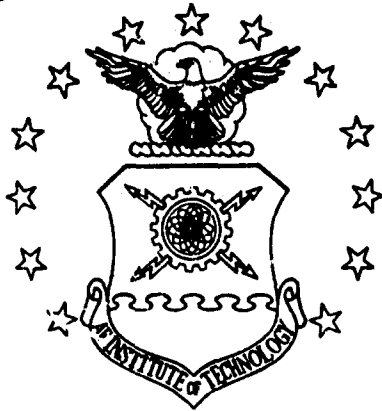


AD 748358

AIR FORCE INSTITUTE OF TECHNOLOGY



AIR UNIVERSITY
UNITED STATES AIR FORCE



EXPERIMENTAL INVESTIGATION OF INITIAL
SURFACE PARTICLE MOTION RESULTING
FROM SMALL SUBSURFACE EXPLOSIONS
IN DRY OTTAWA SAND

THESIS

ISF/MC/72-6

Floyd V. Kimberly
Major USAF

SCHOOL OF ENGINEERING

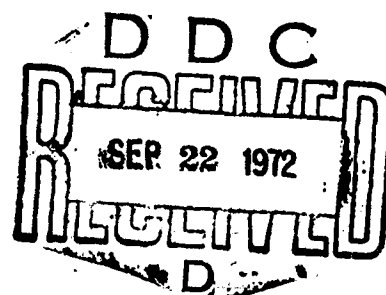
Reproduced by
NATIONAL TECHNICAL
INFORMATION SERVICE
U S Department of Commerce
Springfield VA 22151

WRIGHT-PATTERSON AIR FORCE BASE, OHIO

1

VB

122



EXPERIMENTAL INVESTIGATION OF INITIAL
SURFACE PARTICLE MOTION RESULTING
FROM SMALL SUBSURFACE EXPLOSIONS
IN DRY OTTAWA SAND

THESIS

GSF/MC/72-6

Floyd V. Kimberly
Major USAF

Approved for public release;
distribution unlimited.

1a

DOCUMENT CONTROL DATA - R & D

(Security classification of title, body of abstract and indexing annotation must be entered when the overall report is classified)

1. ORIGINATING ACTIVITY (Corporate author) Air Force Institute of Technology (AFIT-EH) Wright-Patterson AFB, Ohio 45433	2a. REPORT SECURITY CLASSIFICATION Unclassified
	2b. GROUP

3. REPORT TITLE
EXPERIMENTAL INVESTIGATION OF INITIAL SURFACE PARTICLE MOTION RESULTING FROM SMALL SUBSURFACE EXPLOSIONS IN DRY OTTAWA SAND

4. DESCRIPTIVE NOTES (Type of report and inclusive dates)

5. AUTHOR(S) (First name, middle initial, last name)
Floyd V. Kimberly
Major USAF

6. REPORT DATE June 1972	7a. TOTAL NO. OF PAGES 107	7b. NO. OF REFS 19
-----------------------------	-------------------------------	-----------------------

8a. CONTRACT OR GRANT NO.	9a. ORIGINATOR'S REPORT NUMBER(S) GSE/NO/72-6
b. PROJECT NO.	
c.	9b. OTHER REPORT NO(S) (Any other numbers that may be assigned this report)
d.	

10. DISTRIBUTION STATEMENT
Approved for public release; distribution unlimited

Approved for public release; IAW AFR 190-17 Keith A. Williams, 1st Lt., USAF Acting Director of Information	11. SPONSORING MILITARY ACTIVITY Air Force Weapons Laboratory (AFSC) Kirtland AFB, New Mexico 87117
---	---

13. ABSTRACT - An analysis was made of the relationships of surface motion to depth of burst (DOB) for 1.7 gram, spherical charges of lead azide detonated in dry Ottawa sand. Surface motion was studied by taking high-speed movies of each test. A colored sand grid pattern was laid on the surface of the test bed, so the intersections of the pattern could provide the data points for study. The films were analysed by using a film reader for data reduction and computer programs for curve fitting. Relationships of velocity vs. DOB, ejection angle vs. DOB, ejection angle vs. velocity, and mound growth vs. time were studied. (U)

For each equi-distant point from Surface Ground Zero (SGZ), a log-log plot of velocity versus DOB showed two connecting straight line segments with the change in slope at 30mm DOB. The slopes of the lines for points from SGZ to 50mm from SGZ changed systematically from negative to positive for DOB's down to 30mm. For depths greater than 30mm, all the slopes were sharply negative. The "break" in the curves at 30mm DOB was attributed to the change in the role of spallation and gas acceleration for crater formation. Ejection angle increased systematically with an increase in DOB. Ejection angle vs. velocity produced a linear relationship for each equi-distant point from SGZ. The slopes of the lines decreased systematically with increasing distance from SGZ. To study mound growth, a shape factor, the ratio of height to width of the base of the mound, was determined and plotted against time. The factor varied linearly for each DOB with decreasing slope for increasing DOB. (U)

A comparison was made with a similar study which used targets on the pre-shot surface to study surface motion. The results from the two studies varied sufficiently to question the use of targets to provide an adequate analysis of surface motion. (U)

ih

14

KEY WORDS

LINK A

LINK B

LINK C

ROLE

WT

ROLE

WT

ROLE

WT

Laboratory Cratering Experiments
Subsurface Explosions
Ottawa Sand
Gran Size Charges
Surface Ejection Topography
Initial Particle Motion
Initial Ejection Angle
Initial Velocity
Mound Growth

Unclassified

Security Classification

10

EXPERIMENTAL INVESTIGATION OF INITIAL
SURFACE PARTICLE MOTION RESULTING
FROM SMALL SUBSURFACE EXPLOSIONS
IN DRY OTTAWA SAND

THESIS

Presented to the Faculty of the School of Engineering
of the Air Force Institute of Technology

Air University

in Partial Fulfillment of the
Requirements for the Degree of
Master of Science

by

Floyd V. Kimberly
Major USAF

Graduate Space Facilities

June 1972

Approved for public release;
distribution unlimited.

id

Preface

When the subject of small scale cratering for a thesis topic was first presented to me, I was fascinated by the implications it had to problems which the Air Force is and will be facing. I was somewhat skeptical about the real applicability of the project, but since my interest was aroused, I decided to accept the challenge. Early meetings with Major Stewart Johnson of the Air Force Institute of Technology (AFIT) and Messrs. Hal Swift and D. D. "Monty" Preonas of the University of Dayton Research Institute (UDRI) enlightened me on the usefulness of the program, and they encouraged my work on the surface motion investigation.

The project was conducted in conjunction with the UDRI, Dayton, Ohio, which was under contract to the Air Force Weapons Laboratory (AFWL), Kirtland Air Force Base, New Mexico, with funds provided by the Defense Nuclear Agency. The description of the scope and importance of the project provided by Major Neal L. Mping of AFWL in the initial phase of experimentation was especially appreciated. The assistance and information on computer programs given by Captain John Kaiser of AFWL was also helpful.

I give the utmost thanks to the staff at the UDRI for their cooperation and assistance during these past 9 months. The technical expertise, manual dexterity, and conscientiousness displayed by Mr. Steve Hanchak and Mr. Andrew Piekutowski were primary factors in the success of my project. I am indebted for their experimental know-how

and help through times of need. I thank Monty Preonas for the computer programs which he adapted for my use to provide a computerized analysis of the data. I appreciate the many hours which he spent helping me understand problem areas which confronted me from time to time.

I want to thank Mr. Phil Graf of the UDRI Data Reduction Facility for the unlimited use of the film reader. His and his staff's assistance at any time I needed it were much more than I could have asked for. The assistance provided by the UDRI Graphic Arts Department was excellent.

I thank my thesis committee for the time and effort spent poring over this literary effort to make it more acceptable. Major Johnson helped me several times by listening to my problems and giving me encouragement to continue. His comments and suggestions were always appreciated. Mr. Swift provided continuing suggestions throughout the experimental phase, as well as excellent critique on the first draft. My thanks also to Dr. Peter Torvik and Captain Thomas Eastler of AFIT for the time spent in critiquing preliminary reports and the drafts of the thesis.

Finally, I wish to thank my wife and children who have endured these many months with a part-time husband and father. My wife, Sharon, showed extraordinary patience and understanding over late dinners and early morning typing.

Floyd V. Kimberly

CONTENTS

	Page
Preface	ii
List of Figures.....	iv
List of Tables.....	vii
Abstract.....	viii
I. Introduction.....	1
Purpose.....	1
Scope.....	2
Definitions	2
Assumptions.....	3
II. Theory and Background.....	6
Cratering Mechanisms.....	6
Crushing, Compaction and Plastic Deformation.....	6
Spallation	7
Gas Acceleration.....	7
Subsidence	8
Scaling Factors	10
Background Information.....	11
III. Experimental Procedure.....	13
Overview.....	13
Materials	16
Cratering Medium.....	16
Explosives	18
Photographic Materials.....	19
Equipment.....	19
Sand Laying Equipment	19
Cameras	24
Photographic Light Fixtures.....	26
Control Equipment.....	29
Procedures.....	33
Safety Precautions.....	33
Preparation of Test Bed.....	34
Final Preparations	35
Camera Techniques.....	36
Post-Shot Operations	36
Exceptions to Procedure	39

	Page
IV. Data Reduction and Analysis	40
Data Reduction.....	40
Data Points	40
Depth of Burst	41
Film Reader	42
Computer Programs	42
Sources of Error	43
Data Analysis.....	44
Particle Velocity.....	44
Ejection Angle	49
Ejection Angle vs. Particle Velocity	52
Mound Growth.....	54
Comparison Analysis	57
V. Conclusions	60
Laboratory Procedures	60
Particle Velocity.....	60
Ejection Angle	61
Velocity vs. Ejection Angle	61
Mound Growth	61
Comparison Observations	62
VI. Recommendations.....	63
Bibliography	64
Appendix A: Materials	66
Appendix B: Equipment.....	76
Appendix C: Cratering Facility Checklist - Before Firing.....	83
Appendix D: Examples of Computer Printouts for One Particle Trajectory	85
Appendix E: Graphs of Ejection Angle vs. Velocity for Depths of Burst from 5.08 mm to 50.8 mm.....	92
Appendix F: Graphs of Mound Growth for Shots at Depths of Burst from 2.54 cm to 5.08 cm	100

LIST OF FIGURES

Figure		Page
1.	Typical Explosion Crater Cross-Section and Nomenclature.....	4
2.	Relative Contributions of Cratering Mechanisms to Apparent Crater Depth as A Function of Depth of Burst.....	9
3.	Positions of Equipment in Laboratory Test Area...	14
4.	Ottawa Sand Grains Magnified 20 Times	17
5.	Lead Azide Charge with Detonator Wires	17
6.	Test Bed With Sand Leveling Apparatus.....	21
7.	Conveyor with Hose Assembly	22
8.	Squirrel Cage in Nozzle.....	23
9.	Scraper for Leveling Sand.....	23
10.	Typical Grid Pattern on Sand Surface.....	25
11.	Laser-Mirror System	25
12.	Schematic Diagram of Photo-equipment Positions..	27
13.	Hycam and Graflex Camera Systems	28
14.	Photoflash Lamps with Fresnel Lenses	28
15.	Fiducial Light Assembly	30
16.	Schematic of Fiducial Light Operation	30
17.	Collimated Light from Side Lights	31
18.	Typical Firing Sequence Diagram.....	32
19.	Film Sequence of Mound Growth	37
20.	Illustration of Data Points on the Horizon of the Mound Along with the Velocity Vector and Corresponding Ejection Angle for Each Point.	40

Figure		Page
21.	Velocity vs. Depth of Burst for Surface Particles at Specified Distances from Surface Ground Zero (First Order Curve Fit)	47
22.	Velocity vs. Depth of Burst for Surface Particles at Specified Distances from Surface Ground Zero (Second Order Curve Fit)	48
23.	Ejection Angle vs. Depth of Burst for Surface Particles at Specified Distances from Surface Ground Zero (First Order Curve Fit)	50
24.	Ejection Angle vs. Depth of Burst for Surface Particles at Specified Distances from Surface Ground Zero (Second Order Curve Fit)	51
25.	Family of Curves of Ejection Angle vs. Velocity for Surface Particles at Specified Distances from Surface Ground Zero	53
26.	Definition of Shape Factor	54
27.	Example of Mound Growth for Shot S-5-19	55
28.	Shape Factor (H/W) vs. Time for 1.7 gm Charge at Varying Depth of Burst	56
29.	Average Grain Size Distribution for White Sand ..	68
30.	Average Grain Size Distribution for Colored Sand	69
31.	Computer Tabular Print for x-Velocity	86
32.	Computer Graph Plot for x-Velocity	87
33.	Computer Tabular Print for y-Velocity	88
34.	Computer Graph Plot for y-Velocity	89
35.	Computer Tabular Print for Ejection Angle	90
36.	Computer Graph Plot for Ejection Angle	91

Figure		Page
37.	Ejection Angle vs. Particle Velocity for DOB of 5.08 mm	93
38.	Ejection Angle vs. Particle Velocity for DOB of 10.15 mm	94
39.	Ejection Angle vs. Particle Velocity for DOB of 15.25 mm	95
40.	Ejection Angle vs. Particle Velocity for DOB of 25.4 mm	96
41.	Ejection Angle vs. Particle Velocity for DOB of 35.6 mm	97
42.	Ejection Angle vs. Particle Velocity for DOB of 45.7 mm	98
43.	Ejection Angle vs. Particle Velocity for DOB of 50.8 mm	99
44.	Mound Growth of Shot S-101-12	101
45.	Mound Growth of Shot S-104-24	102
46.	Mound Growth of Shot S-25-6	103
47.	Mound Growth of Shot S-5-19	104
48.	Mound Growth of Shot S-7-28	105
49.	Mound Growth of Shot S-9-7	106

LIST OF TABLES

Table		Page
I.	Physical Properties of Ottawa Sand	18
II.	Photo-equipment Distances Correlating to Figure 12	27
III.	Mean Crater Dimensions for Varying Depths of Bursi. of 1.7 g Charges	38
IV.	Particle Motion Data (First Order Least Squares Fit).....	45
V.	Particle Motion Data (Second Order Least Squares Fit).....	46
VI.	Comparable Motion Data from Galbraith's and Present Studies	58
VII.	Weights of Lead Azide Charges Used in Experiments.....	73
VIII.	Physical Properties of Lead Azide.....	75

Abstract

An analysis was made of the relationships of surface motion to depth of burst (DOB) for 1.7 gram, spherical charges of lead azide detonated in dry Ottawa sand. Surface motion was studied by taking high-speed movies of each test. A colored sand grid pattern was laid on the surface of the test bed, so the intersections of the pattern could provide the data points for study. The films were analysed by using a film reader for data reduction and computer programs for curve fitting. Relationships of velocity vs. DOB, ejection angle vs. DOB, ejection angle vs. velocity, and mound growth vs. time were studied.

For each equi-distant point for Surface Ground Zero (SGZ), a log-log plot of velocity versus DOB showed two connecting straight line segments with the change in slope at a DOB of 30 mm. The slopes of the lines for points from SGZ to 50 mm from SGZ changed systematically from negative to positive for DOB's down to 30 mm. For depths greater than 30 mm, all the slopes were negative. The "break" in the curves at a DOB of 30 mm was attributed to the change in the role of spallation and gas acceleration for crater formation. Ejection angle increased systematically with an increase in DOB. Ejection angle vs. velocity produced a linear relationship for each equi-distant point from SGZ. The slopes of the lines decreased systematically with increasing distance from SGZ. To study mound growth, a shape factor, the

ratio of height to width of the base of the mound, was determined and plotted against time. The factor varied linearly for each DOB with decreasing slope for increasing DOB.

A comparison was made with a similar study which used targets on the pre-shot surface to study surface motion. The results from the two studies varied sufficiently to question the use of targets to provide an adequate analysis of surface motion.

EXPERIMENTAL INVESTIGATION OF INITIAL
SURFACE PARTICLE MOTION RESULTING
FROM SMALL SUBSURFACE EXPLOSIONS
IN DRY OTTAWA SAND

I. Introduction

In the past several years, studies of cratering phenomenology have been prompted for two basic reasons. The advent of nuclear explosives gave impetus to programs such as Plowshare, which investigated the engineering capabilities of these explosives. A military interest in cratering, both conventional and nuclear, was fairly obvious. The threat to the survivability of personnel, structures, and even silo-housed, retaliatory missiles has intensified the need for in-depth studies of explosively formed craters. Many studies have been made in determining the size and shape of such craters to be able to adequately predict possible future craters. Few investigations, however, have been made in determining the initial surface motion of the earth media. It is hoped that this study can provide some definite steps in the fulfillment of this task.

Purpose

The primary purpose of this investigation is to analyse and determine the relationships of initial velocity and ejection angle to

initial position of ejecta particles set in motion by subsurface explosions at varying depths of burst. The determination of these parameters for ejecta particles should provide sufficient data to predict the distance these particles will travel and the velocity at which they will impact. A secondary purpose is to analyse the mound growth with relation to time. The determination of the growth of the mound may be of use in refining existing computer hydrocodes, which are computer simulations of explosion cratering events. Currently these programs do not accurately describe the particle motion corresponding to the final ejecta patterns. Similar work was done by Galbraith in 1970 (Ref 8), and an attempt is made to correlate the data from the two studies.

Scope

Ten, 1.7 gram, lead azide, explosive charges were detonated at various depths in dry Ottawa sand. High-speed motion pictures were taken of the immediate area around surface ground zero to study particle motion, and mound growth by following intersection points of a grid which was laid on the surface. A digital film reader was used to provide data for determining ejection angles and velocities of the intersection points.

Definitions

Several pioneers in the investigation of craters have suggested some standard terms for discussing cratering phenomenology (Ref 9:2).

The following terms are those which will be used in this discussion.

They are also noted in Figure 1 which shows a typical crater cross-section.

Surface Ground Zero (SGZ). That point in space, directly above the center of the explosion, on the plane of the original surface. Most crater dimensions are measured from this point or from a plane passing through it.

Apparent Crater Surface (S_a). The crater formed by the rock-air or rubble-air interface below the pre-shot surface.

Apparent Radius (R_a). The distance measured from SGZ, along the plane of the pre-shot surface, to the apparent crater wall.

Apparent Depth (D_a). The distance measured from SGZ, along a line normal to the pre-shot surface, to the bottom of the apparent crater.

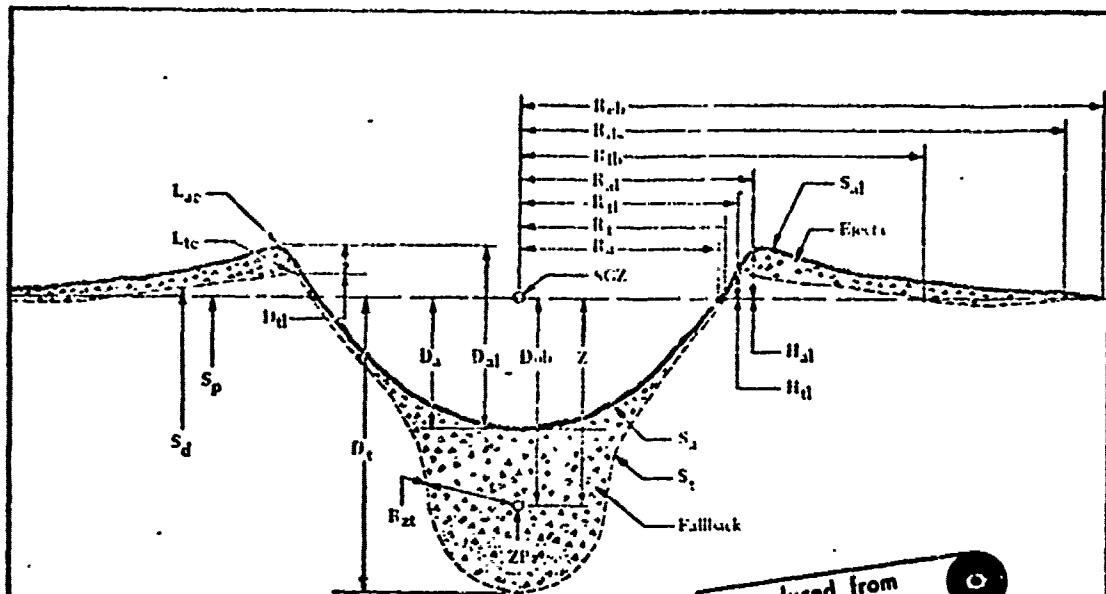
Depth of Burst (DOB). The distance below SGZ to the effective center of the charge.

Ejecta. That material which is thrown clear of the crater walls.

Fallback. That material which returns to the area within the crater walls.

Assumptions

The cratering medium was assumed to be a semi-infinite half-space to eliminate the problems associated with accounting for boundary effects other than the sand-air interface. This assumption has been examined previously and found to be a reasonable one (Ref 8:2,



Reproduced from best available copy.

- D_a . . . Maximum depth of apparent crater below preshot ground surface measured normal to the preshot ground surface.*
- H_{d1} . . . Depth of apparent crater below average apparent crater lip crest elevation.
- D_{ob} . . . Normal depth of burst (measured normal to preshot ground surface).
- D_t . . . Maximum depth of true crater below preshot ground surface.
- H_d . . . Depth of true crater lip crest below apparent crater lip crest.
- Ejecta . . . Material above and or beyond the true crater and includes: (1) fallback; (2) breccia-ballistic trajectory; (3) dust-aerosol transport; etc.
- Fallback . . . Material fallen inside the true crater and includes: (1) slide blocks; (2) breccia and stratified fallback-ballistic trajectory; (3) dust-aerosol transport; (4) talus; etc.
- H_{d1} . . . Apparent crater lip crest height above preshot ground surface.
- H_d . . . True crater lip crest height above preshot ground surface.
- L_{ac} . . . Apparent crater lip crest.
- L_{tc} . . . True crater lip crest.
- R_a . . . Radius of apparent crater measured on the preshot ground surface.
- Note: The radius measurements pertain only to single charge craters and represent average dimensions. If crater shape deviates substantially from circular, the direction of measurement must be specified. An average radius value can also be determined by dividing the plan area by π and taking the square root.
- R_{d1} . . . Radius of apparent lip crest to center.
- R_{d2} . . . Outer radius of displaced surface.
- R_{eb} . . . Radius of outer boundary of continuous ejecta.
- R_{eh} . . . Outer radius of true lip boundary.
- R_t . . . Radius of true crater measured on the preshot ground surface.
- R_d . . . Radius of true lip crest to center.
- R_{zt} . . . Distance between the zero point and the true crater surface measured in any specified direction. When measured in a direction below the zero point is equivalent to lower cavity radius.

- S_a . . . Apparent crater surface, e.g. rock-air or rubble-air interface.
- S_{a1} . . . Apparent lip surface.
- SGZ . . . Surface ground zero.
- S_d . . . Displaced ground surface.
- S_p . . . Preshot ground surface.
- S_t . . . True crater surface, e.g. rock air or rock rubble interface.
- V_a . . . Volume of apparent crater below preshot ground surface.
- V_{a1} . . . Volume of apparent crater below apparent lip crest.
- V_t . . . Volume of true crater below preshot ground surface.
- V_{t1} . . . Volume of true crater below true crater lip crest.
- Z . . . Vertical depth of burst (equivalent to D_{ob} when crater is formed on a horizontal surface).
- ZP . . . Zero Point—effective center of explosion energy.
- Note: The following definitions apply to linear craters only. Linear crater refers to the excavation formed by overlapping crater effects resulting from a row of charges. All above terms applicable to single craters apply also to linear craters with the exception of the radius terms which are replaced by the width terms below.
- W_a . . . Width of apparent linear crater measured on the preshot ground surface.
- W_{a1} . . . Width of apparent lip crest measured across linear crater.
- W_d . . . Width of displaced surface measured across linear crater.
- W_{eb} . . . Width of outer boundary of continuous ejecta measured across linear crater.
- W_{eh} . . . Width of true crater outer lip boundary measured across linear crater.
- W_t . . . Width of true linear crater measured on the preshot ground surface.
- W_{t1} . . . Width of true linear crater lip crest measured across crater.
- * All distances, unless specified otherwise, are measured parallel or perpendicular to preshot ground surface.

Figure 1. Typical Explosion Crater Cross-Section and Nomenclature (Ref 9:2)

Ref 12:4840). These past experimenters used charges and containers which were about the same size as those used in the present study. No apparent variations in craters were observed with depths of sand greater than 35 cm. In the current study, sand depths were 61 cm. Since the experiments were conducted inside an air-conditioned building, humidity and temperature were considered to be constant.

II. Theory and Background

Cratering Mechanisms

In general, all craters formed by subsurface explosions induce the same effects on the surrounding material. The material properties and the depth of the burst will cause the intensity and extent of the effects to vary. In 1961, Nordyke presented a theory on the mechanisms involved in crater formation, based on empirical data and theoretical calculations (Ref 14). This theory has been tested and found to be very accurately stated. There are essentially four distinct phenomena related to a subsurface explosion in terms of the effects on the cratering medium. They are: (1) crushing, compaction, and plastic deformation; (2) spallation; (3) gas acceleration; and (4) subsidence (Ref 14:3448-51).

Crushing, Compaction, and Plastic Deformation. When an explosion occurs underground, a shock wave forms and radiates into the surrounding material, causing pressure increases ranging from thousands of atmospheres to 100 million atmospheres in the case of a nuclear explosion. Very high pressures will melt and vaporize the material. The pressure decreases as work is done on the material, causing the effects on the material to vary from melting to crushing to plastic deformation. As the pressure falls below the plastic strength of the material, the shock wave no longer distorts the medium and the shock is attenuated throughout the remainder of the material.

This mechanism is the primary cratering cause in surface or near surface events.

Spallation. The second mechanism of prime importance is that of spallation. Nordyke says it is "probably the most important phenomenon in cratering, especially for shallow depth of burst..." (Ref 14:3450). Spallation is a direct result of the shock wave produced by the explosion. As the compressive wave reaches the free surface, the boundary condition of zero normal stress at that surface must be maintained. A negative stress wave or rarefaction is generated at the interface and propagates back into the medium. At some depth, the sum of the compression and tension stress waves equals the tensile strength of the medium. A tensile failure in the medium occurs at this point and a piece of the medium flies off at a velocity proportional to the momentum trapped in it. This process continues until the tensile strength of the medium exceeds the sum of the stress waves currently active in it. For a cohesionless material such as Ottawa sand, nearly every near-surface particle is affected by spall. In rock, however, slabs of material fly off, depending on the joints or weakened planes present in the rock. As the depth of the explosion increases, the effect of spalling decreases until it ceases to be of consequence when compared to the gas acceleration phase.

Gas Acceleration. The gas acceleration of material is primarily a consequence of a moderate depth of burst. It is of relatively long

duration when compared to the duration of the first two cratering mechanisms. Gases formed by the explosion expand adiabatically in the explosion cavity. The gas bubble rises, pushing the overlying material ahead of it, forming a surface mound in less competent material and causing cracks along the joints and fractures in rock. The bubble continues to rise and the surface stretches into a large, head-like shape, until the rising gas bursts through the surface. This rising mound of earth is given sufficient momentum by the gas to cause the mound to disintegrate and be ejected in all directions. This mechanism is significant from moderate depths of burst to some critical depth where the effect abates to a negligible particle acceleration and subsidence becomes apparent.

Subsidence. Subsidence is most evident in cases of deep explosions. After material surrounding the explosion is crushed by the shock wave, the gaseous products of the explosion percolate into the cracks and fissures in the cavity walls and ceiling. The broken material in the ceiling falls into the cavity. The extensive pressures produced during the gas expansion cause the ceiling to break and fall, until the entire overlying strata has subsided into the cavity (Ref 14:3450).

The relative contributions of these phenomena to crater depth as a function of depth of burst is shown in Figure 2. Of the four mechanisms, two are of prime interest in studying ejecta particle motions--spallation and gas acceleration. The effects of these two phenomena are easily seen on high-speed motion pictures of a subsurface explosions.

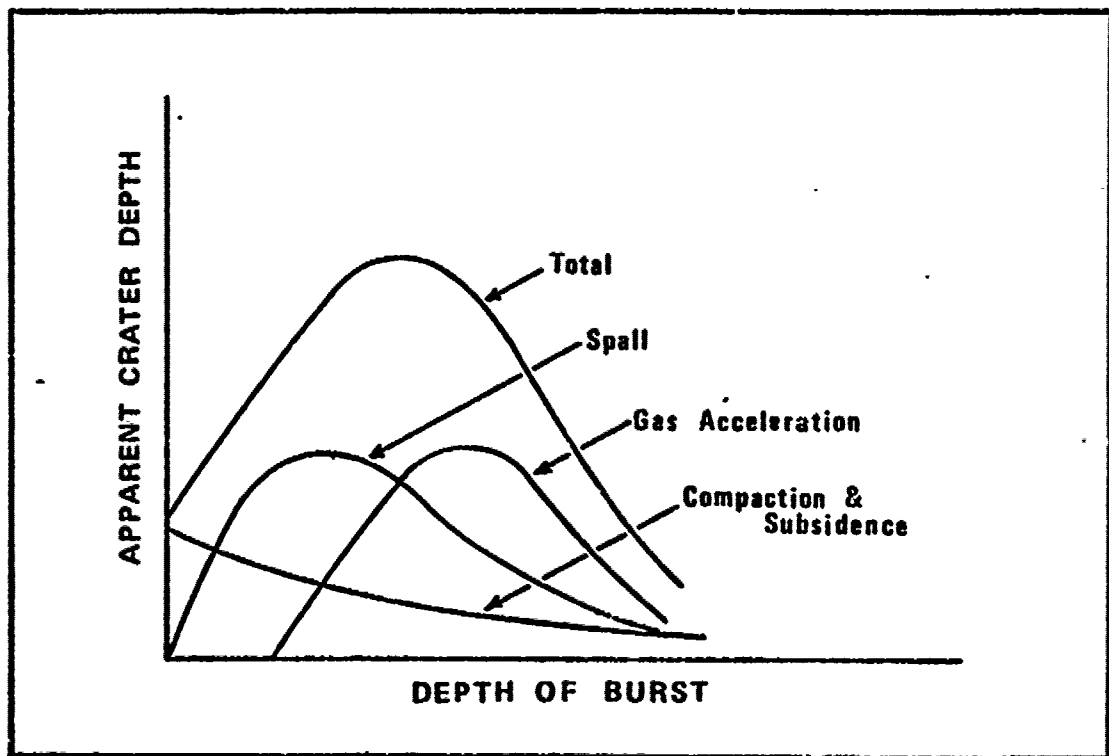


Figure 2. Relative Contribution of Cratering Mechanisms to Apparent Crater Depth as a Function of Depth of Burst (Ref 14:3457)

Scaling Factors

Since the concept of using smaller chemical explosives to simulate nuclear effects in cratering was proposed, several methods of scaling the results of small scale tests have been tried. Initially, linear dimensions of the crater were empirically determined to scale as the cube root of the explosive weight, $W^{1/3}$. As more data became available, scaling factors ranging from cube root to fourth root were tried and in 1959, Chabai determined by regression analysis that the $3/10$ power of explosive energy was the most viable scaling factor. Although the small difference between $1/3$ and $3/10$ is negligible in energy ratios of 10 or less, when the ratios become greater than 10^3 , appreciable differences are observed in crater dimensions. These early empirically determined theories usually neglected the effects of material properties and sometimes neglected gravity effects (Ref 5:5075-76).

More recent investigations have determined the importance of these neglected areas. The effect of gravity has been studied by Johnson, et al (Ref 12) and Herr (Ref 10) and proven to be a necessary consideration in scaling crater dimensions. Westine (Ref 18) has determined a scaling formula using material properties in conjunction with explosive weight and depth of burst. Data previously collected was plotted by Westine using his formula, and excellent correlation was observed in the yield range of 256 lb (116.12 kg) to 100 kilotons (90.72×10^6 kg) of TNT and in several different types of soil (Ref 18:12-17).

Background Information

Particle velocity is a function of energy released, the properties of the material in which the explosion takes place, depth of burst, and initial radial distance from the explosion. Studies of this particle motion have been relatively few in number.

There have been some investigations, however, tracking discrete targets which were used to estimate induced ground motion. These targets have been of varying sizes and shapes and were either buried or placed on the surface. Hess and Nordyke, in a large scale test (Ref 11), used radioactive pellets which were placed at various depths and distances from SGZ. Vortman, in a large scale test (Ref 17), and Christopher, in a small scale test (Ref 6) used wooden targets which were driven into the ground. These investigators used high-speed photography to follow their targets from the initial position to various stages from the beginning of ballistic flight to final impact. Using the resulting photographs they were able to plot displacement, velocity and acceleration curves for the targets.

Wisotski (Ref 19) and Sogge (Ref 15) tracked chunks of rock visible in motion pictures of large scale cratering tests. Galbraith (Ref 8) traced the paths of small glass beads recorded by time lapse photography of small scale laboratory tests. These investigators followed the ballistic flight of the targets and calculated a drag coefficient, an initial velocity and initial ejection angle for each target.

In the small scale tests, the targets did not adequately couple with the ground motion because of the inertia of the relatively large targets (Ref 6:A-7, Ref 8:13). Nevertheless, data collected using these techniques may be significant if subsequent data on discrete soil particles can be correlated with it. In the present study, an attempt is made to follow the actual ground surface of the sand from detonation to the beginning of ballistic flight.

Because of the large amount of data generated by Galbraith, an effort to duplicate his laboratory setup was made to allow for correlation between the two studies. Several experimental refinements were made to facilitate a more detailed study of mound growth and discrete particle motion.

III. Experimental Procedure

Overview

The cratering laboratory was located in the Kettering Engineering and Research Building on the campus of the University of Dayton. The laboratory was divided into a test area and a control room/office. All of the equipment necessary for performing the experiments was located in the test area, as shown in Figure 3. The circular tank was filled with Ottawa sand with the use of a conveyor. Spherical lead azide charges were placed at various depths below the sand bed surface and detonated for investigation. Ten different experiments, or shots as they were commonly called, were performed for this study.

A grid pattern of colored and white sand was laid on the surface of the sand bed so that specific points on the surface of the mound formed by the explosion of the charge could be followed. The grid line intersections were fairly easy to follow as the lines crossed the horizon of the mound, so these were the points chosen to determine surface motion.

For each of the shots, three different cameras were used to record data and to document the events. Two cameras were high speed, motion picture cameras and the third was a format camera. One of the movie cameras took pictures of the immediate surface area above the charge and the resulting films were analysed to study surface particle motion

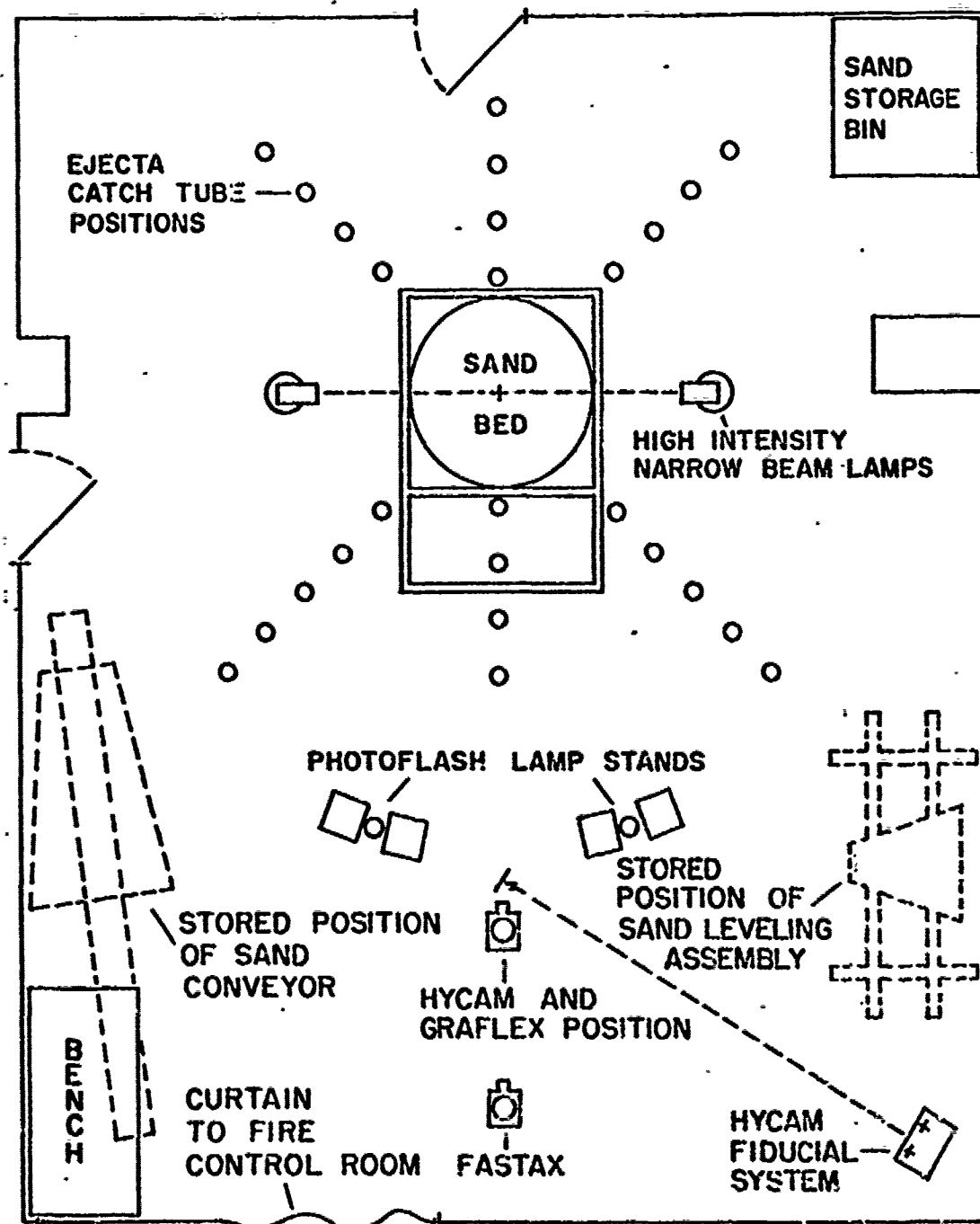


Figure 3. Positions of Equipment in Laboratory Test Area

and mound growth. The second movie camera viewed the entire sand bed and the resulting films were used mostly for documentary purposes. The format camera was used to capture particle trajectories by taking a time exposure through a fan-like wheel which was mounted in front of the camera lens. This procedure could be likened to a time exposure of moving lights which were chopped by the wheel.

Lighting was provided for the movies by two sets of photo-flash lamps which were synchronized and sequenced. Lighting for the format camera was provided by two banks of two specially-designed lamps. Each of these lamps collimated light from two quartz lamps through waterfilled, semi-cylindrical, lenses to light a narrow area vertically above the sand bed. To minimize reflection of light during the filming operation, the walls and equipment within camera range were painted flat black.

The control equipment for the test operation was centrally located in the control room portion of the laboratory. Most of the test equipment was operated through a single panel. The following sections of this chapter describe the equipment, materials, and procedures used in these experiments. Detailed dimensions and explanations are included in Appendixes A and B.

Materials

The materials used in the experiments can be separated into 3 groups: (1) the cratering medium, (2) explosives and (3) photographic materials.

Cratering Medium. Ottawa sand was chosen for use as the cratering medium for several reasons. The primary reason was to facilitate correlation of data obtained in this study with data obtained in previous studies. Dry, cohesionless sand is a simple medium to work with, and is easy to handle. Its uniform particle size coupled with its lack of cohesion permit highly symmetric craters to be formed. The high degree of optical reflectance is of prime importance to the photographic techniques which were used. The uniformity of Ottawa sand grain is illustrated in Figure 4.

In these experiments, an attempt was made to follow individual sand grains set in motion by the explosion. For ease in following these grains, some of the white sand was dyed different colors and a grid pattern was made on the surface. The sand colors available for use were green, black, blue, red, and pink. No significant changes in physical properties resulted from the coloring operation.

Standard soil property tests conducted as described in Appendix A yielded the results shown in Table I.

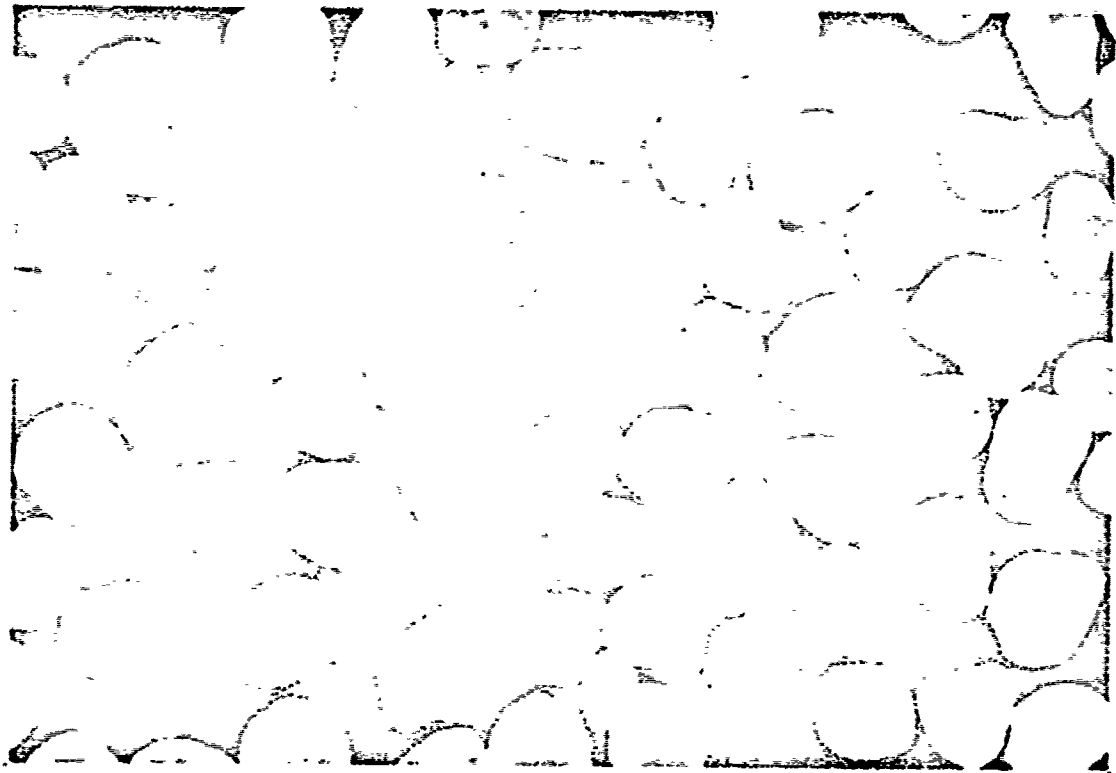
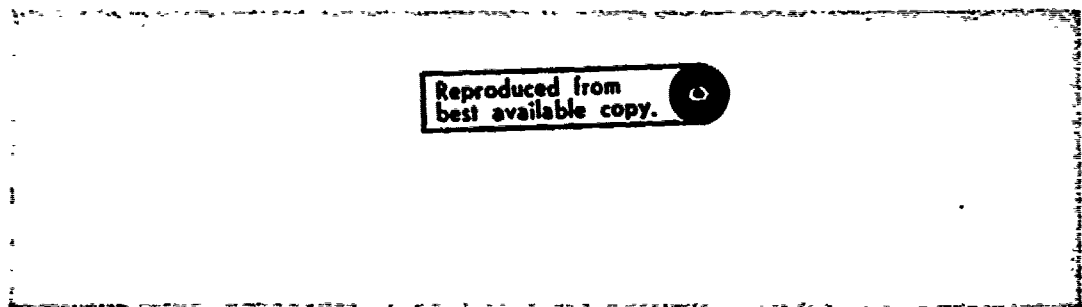


Figure 4. Ottawa Sand Grains Magnified 20 Times



Reproduced from
best available copy.



Figure 5. Lead Azide Charge with Detonator Wires

Table I
Physical Properties of Ottawa Sand

In-situ Density	
old test bed:*	1.75 g/cc
new test bed:	1.80 g/cc
Angle of Internal Friction:	37.5°
Coefficient of Uniformity:	1.39
Coefficient of Gradation:	0.95
Specific Gravity:	2.65
Void Ratio:	0.47
Porosity:	31.97%
Moisture Content:	0.0%
*Explained on page 39	

Explosives. Spherical charges of lead azide (Figure 5) were chosen for the explosive primarily to facilitate correlation of data. The decision to lead azide was also influenced by its consistent behavior as a primary explosive (Ref 7:285). Following ignition, it is second only to mercury fulminate in ease of transition from deflagration to detonation (Ref 7:284).

The charges weighed 1.7 grams \pm 0.01 gram and had a diameter of 10.16 mm. They were coated with a 50 micron layer of nitrocellulose and packaged in aluminum foil to provide protection from moisture, abrasion, and static electricity. The charges were centrally ignited

by a notched tungsten wire. The explosive properties of lead azide are given in Table VIII in Appendix A.

Photographic Materials. Both black-and-white and color film were used in the 16 mm, high-speed cameras. The Graflex still camera used a black-and-white cut film pack. General Electric No. 22 and No. 50 flashbulbs were used for the photoflash lamps. The No. 22 bulbs used early in the study provided about 55 msec of useful light. The No. 50 bulbs were used later in the study and provided about 70 msec of useful light.

Equipment

The equipment necessary for the experiments can be divided into four separate groups: (1) sand laying equipment, (2) photographic light fixtures, (3) cameras and (4) control equipment.

Sand Laying Equipment. A circular steel tank, 76.2 cm high and 148.6 cm in diameter, was built to hold the sand bed. Concrete was poured into the bottom 15.2 cm of the tank and the remainder of the tank was filled with sand. The tank was marked with radial degree designations to facilitate the taking of measurements and the referencing of points in the sand bed. The zero degree radial was along the camera line of sight on the farthest edge of the tank. The remaining radials were designated clockwise from zero. A railed frame was welded to the outside of the tank. This frame

supported a rolling frame used for leveling the sand (Figure 6).

The rolling frame was removed after the sand bed was leveled.

The tank was filled and emptied by using a conveyor with a removable flexible hose and nozzle, shown in Figure 7. The conveyor had a cleated rubber belt for moving the sand. The pulley shaft at the top of the conveyor was used to drive a flexible shaft which turned a "squirrel cage" located in the nozzle (Figure 8). The "squirrel cage" broke up the flow of sand and gave it an even distribution at a uniform density throughout the tank. Sand falling from an elevated sand storage bin was used to feed the conveyor at a constant rate.

A scraper, shown in Figure 9, was designed and built to accurately scrape the sand bed at predetermined surface levels. It could be adjusted vertically to scrape at different depths. For scraping the sand, it was mounted on the aforementioned rolling frame and moved across the sand bed. An industrial vacuum cleaner was used to keep the blade free of an accumulation of sand.

An aluminum grid with 12.7 mm square cells was used to lay a colored sand pattern on the sand surface. A typical pattern is shown in Figure 10.

The geometric center of the tank was determined and a laser-mirror system was installed above the tank to provide a readily available reference which could be used for placing the charge and centering the grid pattern. A laser light beam, 5 mm in diameter

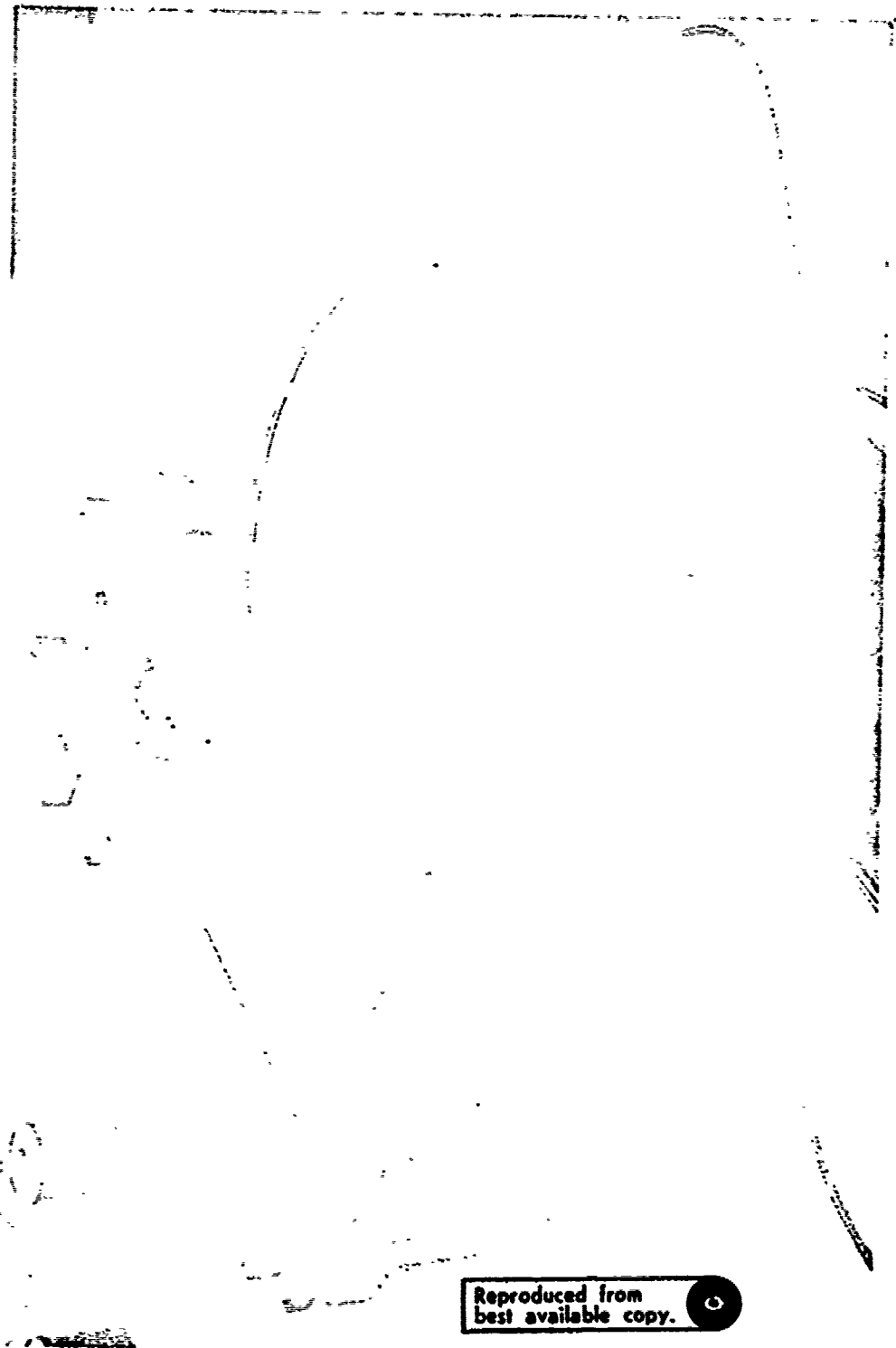


Figure 6. Test Bed with Sand Leveling Apparatus

Reproduced from
best available copy.

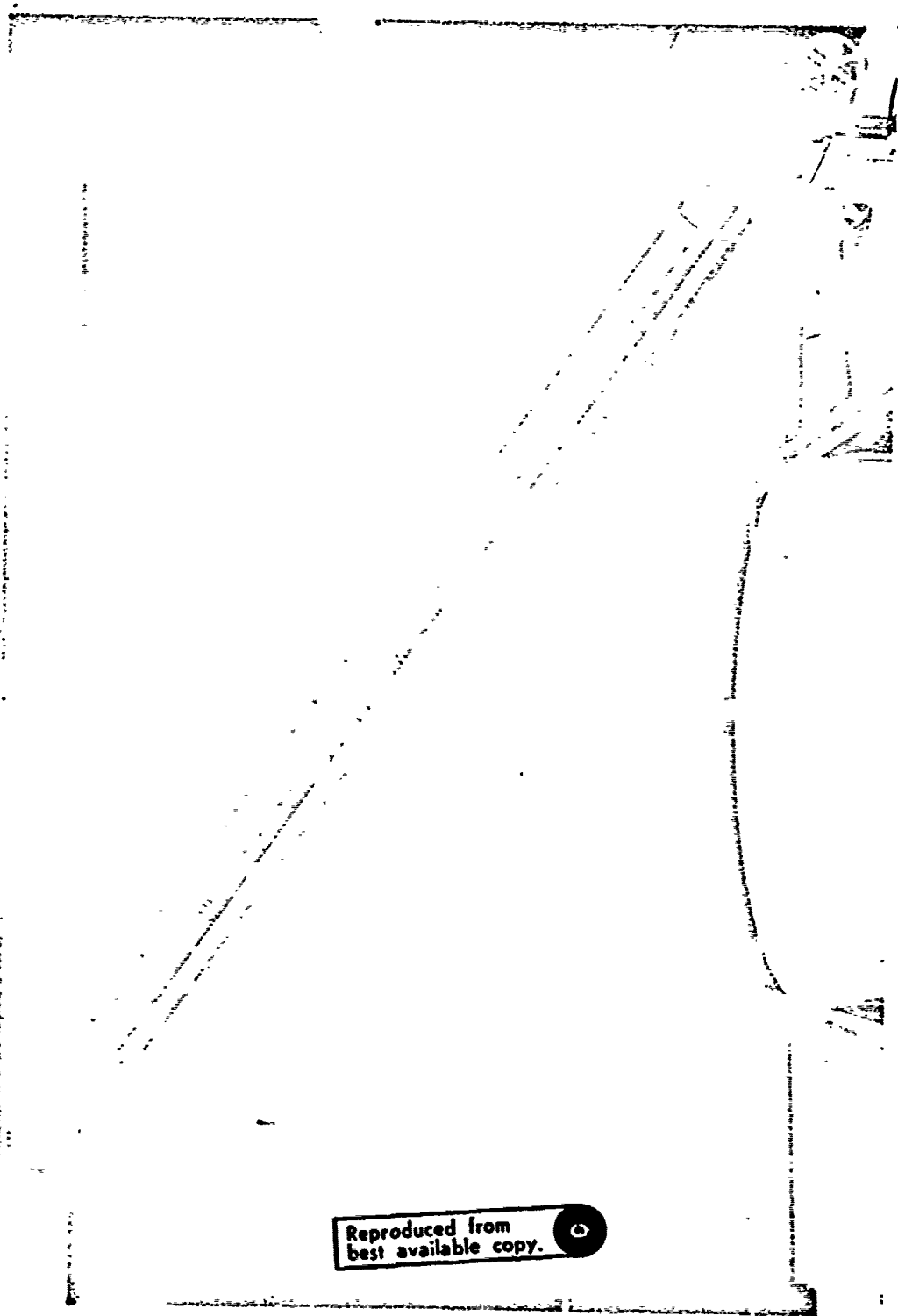


Figure 7. Conveyor with Hose Assembly

Reproduced from
best available copy.

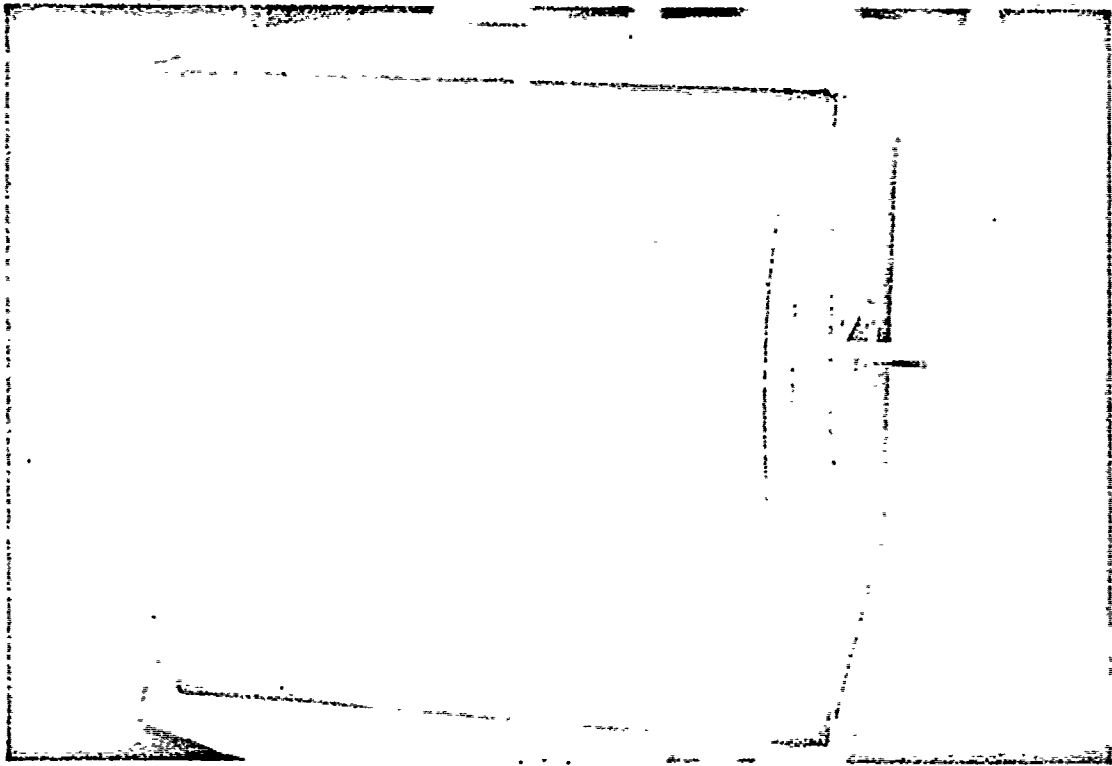


Figure 8. Squirrel Cage in Nozzle

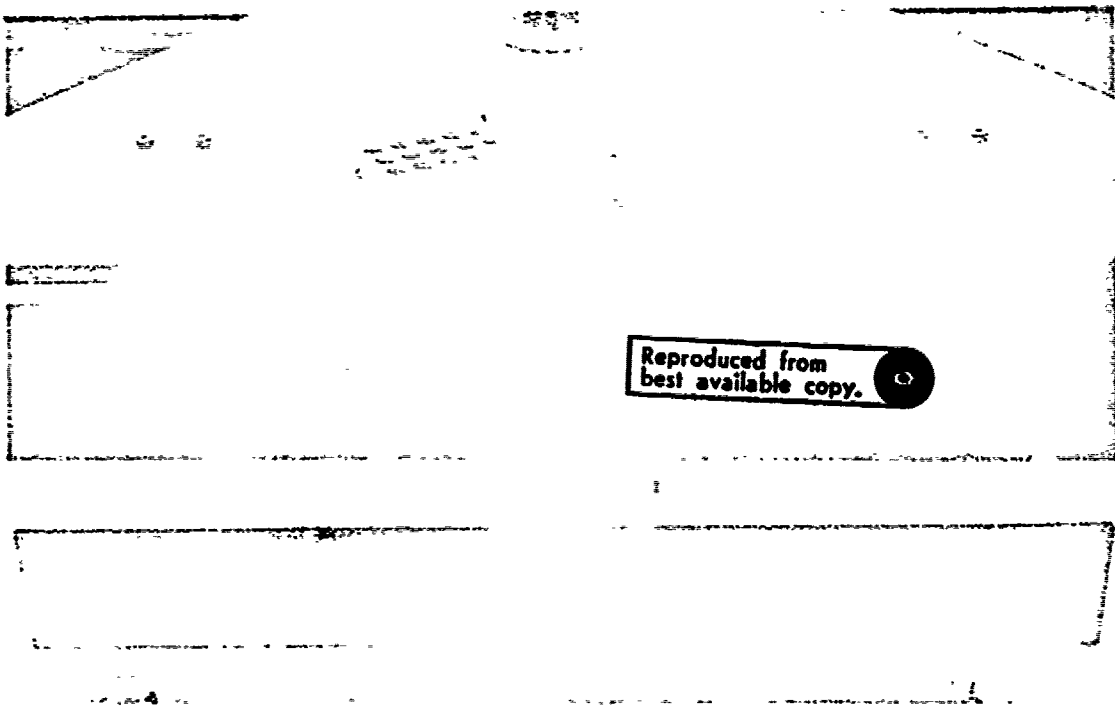
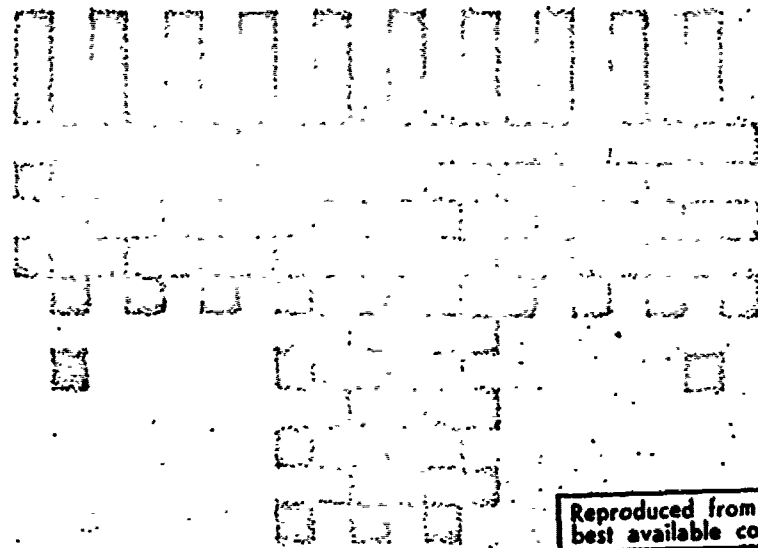


Figure 9. Scraper for Leveling Sand

was reflected downward by a mirror which was adjusted to reflect the light at true vertical onto the center of the tank as indicated in Figure 11.

Another item of importance used during the sand laying operation was an air exhaust system installed over the tank. A centrifugal blower was installed in a duct which was connected to the building exhaust system. This exhaust fan was operated when filling or emptying the tank to keep the test area clear of silica dust. It was also operated to remove dust and toxic fumes from the area when a charge was detonated in the sand bed.

Cameras. Three cameras were used to record information during the experiments. The primary camera for recording mound growth and initial particle motion was a Hycam, high-speed, 16 mm, motion picture camera equipped with a 102 mm, f2.7 lens. The first two events were filmed, using a half-frame viewing head, at approximately 14,000 frames per second (fps). The remaining films were taken with a full-frame head at approximately 7000 fps. Film speed was determined from 1 msec timing marks placed on the edge of the film by a pulse generator. Fiducial marks, described in the next section, and a mark generated by the firing pulse were also recorded on the film. The camera was mounted on a stationary stand with the axis of the lens slightly higher than the surface of the sand and parallel to it to allow a maximum field of view in each frame. However, because of the desired close-up pictures, the realized field



Reproduced from
best available copy.

Figure 10. Typical Grid Pattern on Sand Surface

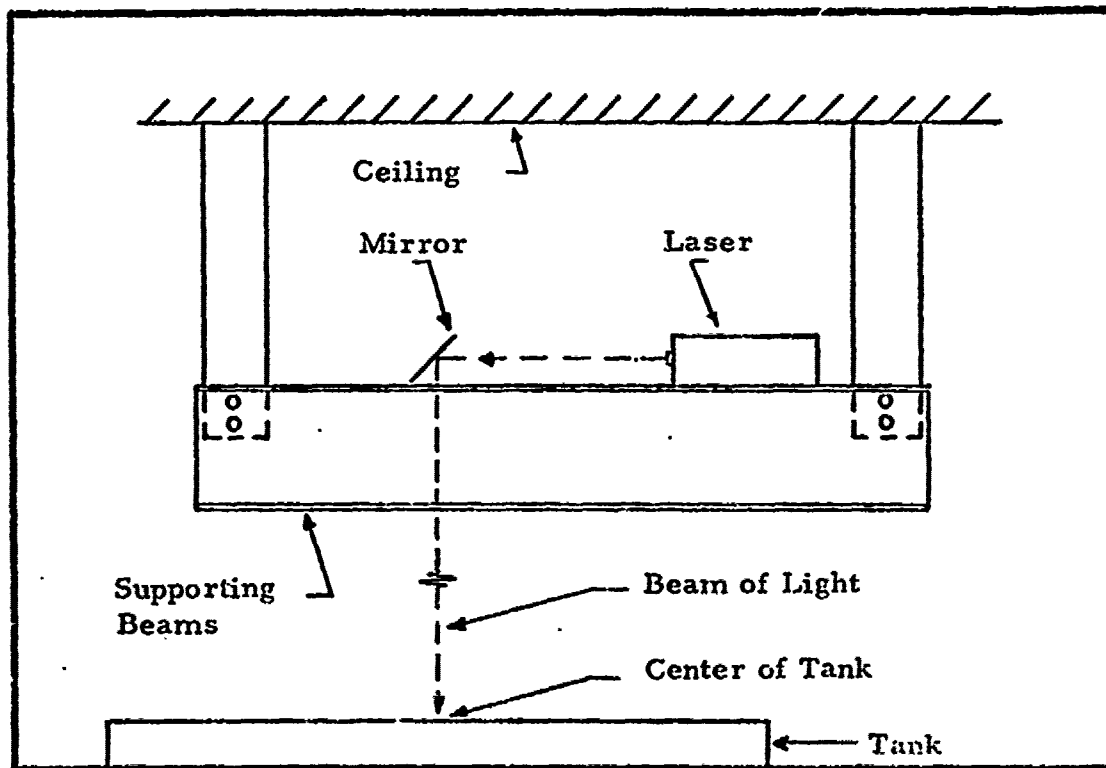


Figure 11. Laser-Mirror System

of view was only 31 cm wide by 22.5 cm high. Figure 12 is a schematic diagram of the photo-equipment and Table II gives the photo-equipment distances in relation to SGZ and the floor.

A Graflex XL camera with an-80 mm, f2.8 lens was used to record a "chopped" 1-sec, exposure of the event. It was mounted on the same stand as the Hycam. A four-bladed chopper wheel directly in front of the Graflex lens caused ejecta motion to be recorded at 120 fps. Figure 13 shows the Hycam and Graflex camera systems.

A Fastax, 16 mm high-speed motion-picture camera with a framing rate of approximately 6700 fps was used as a documentary camera and viewed the entire sand bed. It had a 51 mm, f2.0 lens. A pulse generator produced timing marks at a rate of 1000 per sec on the film from this camera also.

Photographic Light Fixtures. Three types of lighting were used for the photographic work. To illuminate the grid pattern for the high-speed cameras, two banks of three synchronized photoflash lamps were used (Figure 14). Each lamp had a fresnel lens to focus light from the flash onto the grid. The flashbulbs were mounted inside the lamp box at the focal point of the lens. The three lamps on each bank were timed to illuminate in rapid succession providing the 55 or 70 msec of useful light previously described.

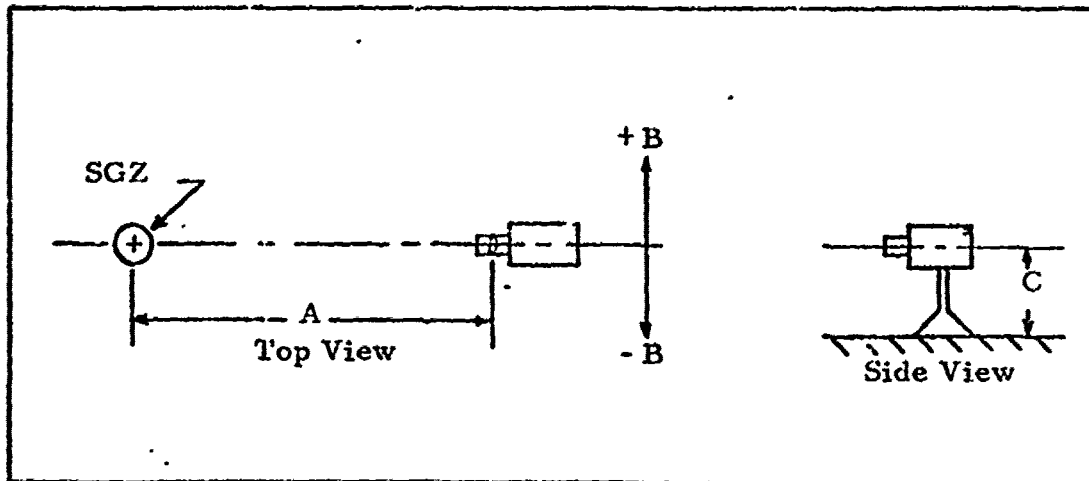


Figure 12. Schematic Diagram of Photo-equipment Positions

Table II

Photo-equipment Distances Correlating to Figure 12

Item	A Distance (cm)	B Off Axis (cm)	C Elevation (cm)
Hycam Camera	414	0	80
Fastax Camera	571	0	221
Graflex Camera	411	0	117
Side Lights	0	±160	120
Flash Bulbs			
A	352	-127	166
B	to Center	- 81	146
C	of Group	- 81	186
D	352	49	165
E	to Center	79	145
F	of Group	79	184

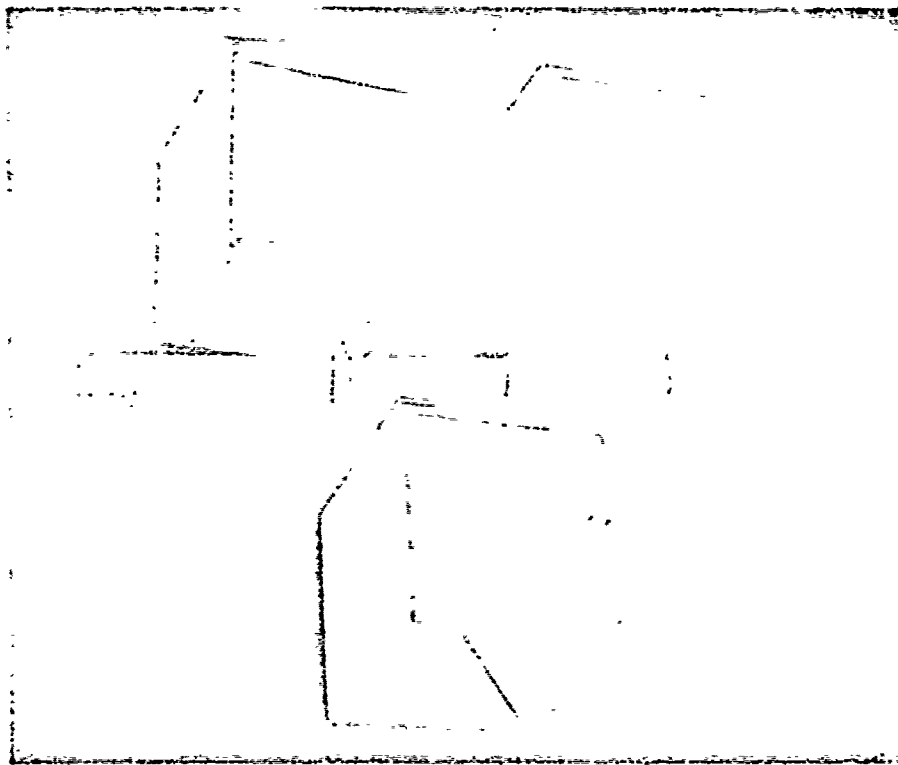


Figure 14. Photoflash Lamps with Fresnel Lenses

Reproduced from best available copy. ©

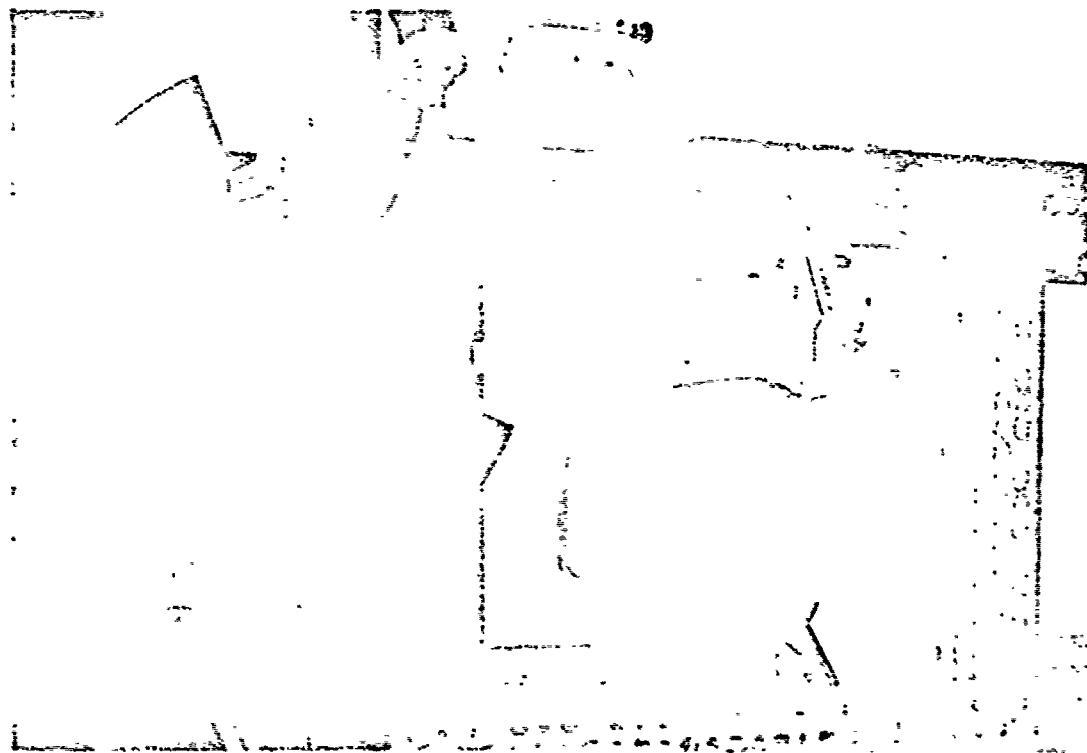


Figure 13. Hycam and Graflex Camera Systems

A system using two, 6.2-v light bulbs fixed behind two convex lenses was used to provide fiducial marks on the film (Figure 15). A painted glass plate with an inscribed cross was mounted behind each lens. Light coming through the cross and lens was focused onto a glass plate mounted in front of the Hycam camera (Figure 13). The resulting crosses were reflected into the camera lens by the glass plate as shown in Figure 16. The glass plate to fiducial lens distance was the same as that from the glass plate to the center of the tank (SGZ), so that the fiducials and the event were simultaneously in focus on the film.

A third set of lights was used to determine ejecta motion with the Graflex camera. A bank of two lamps was installed at each side of the tank to illuminate a very narrow vertical plane above the sand bed. Each lamp consisted of two, high-intensity, quartz bulbs mounted behind a semi-cylindrical, water-filled container used as a lens. A sheet metal cover placed around the lamp allowed a 38 mm-wide, vertical slit of light to shine through, as shown in Figure 17. The light was collimated to provide a maximum, bright-light width of 32 mm at the center of the tank.

Control Equipment. Sequencing control of cameras, lights, and the firing pulse was provided through a single, integrated, electronics control panel. The time sequencing diagram is shown in Figure 18 and a detailed explanation is given in Appendix B. Four pieces of equipment are not in the sequence and are controlled

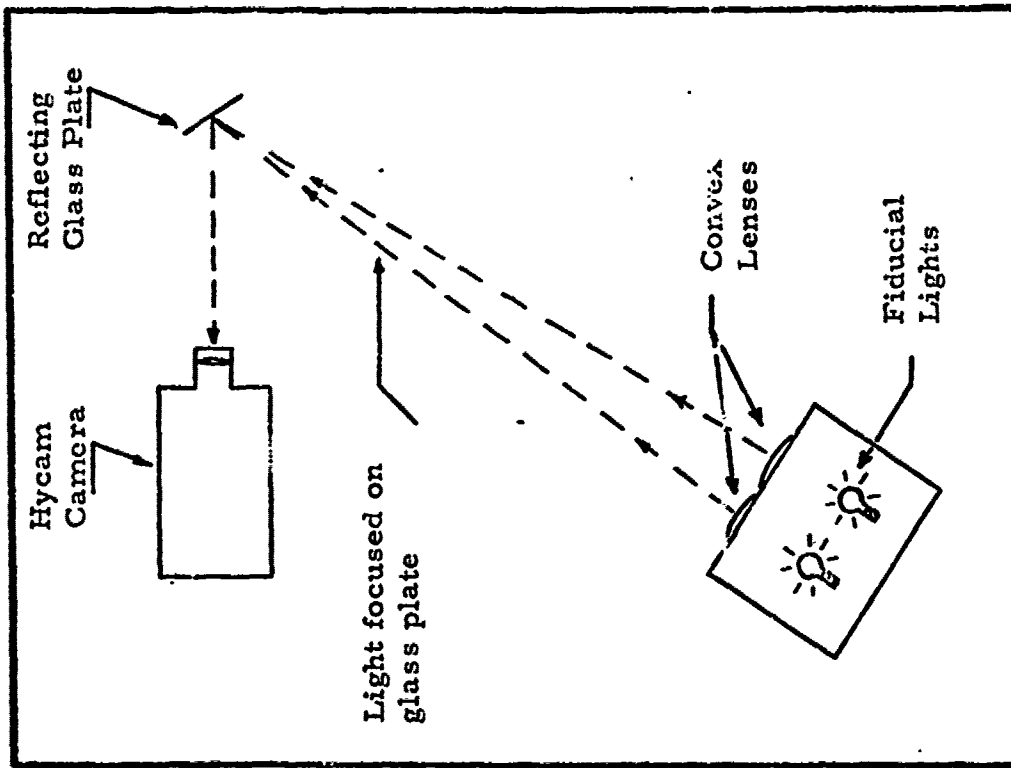


Figure 16. Schematic of Fiducial Light Operation

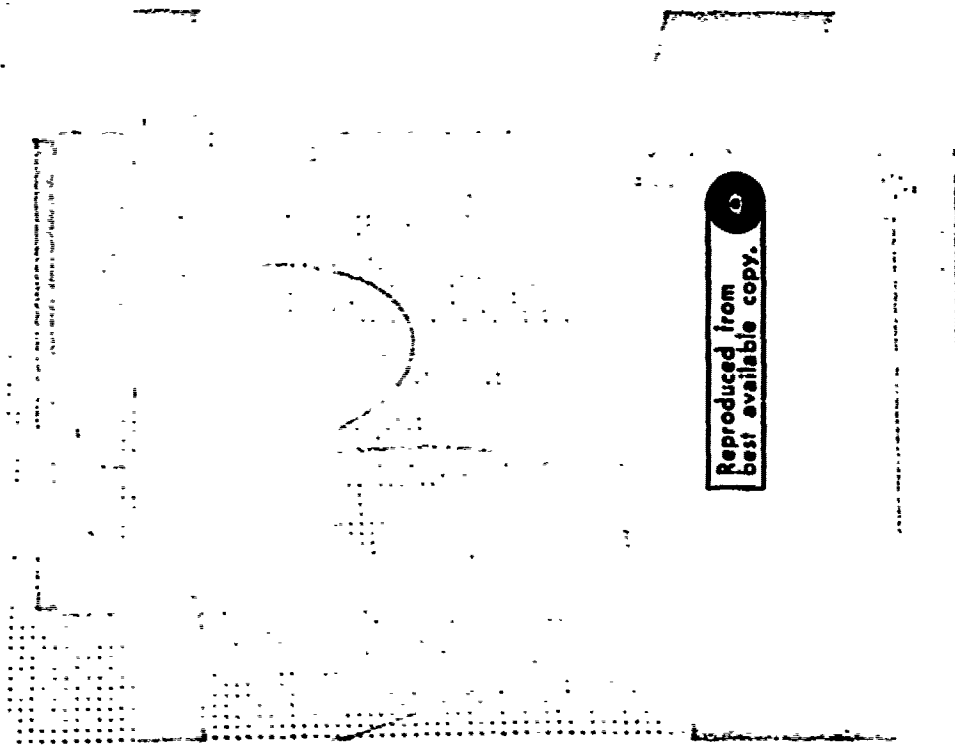


Figure 15. Fiducial Light Assembly

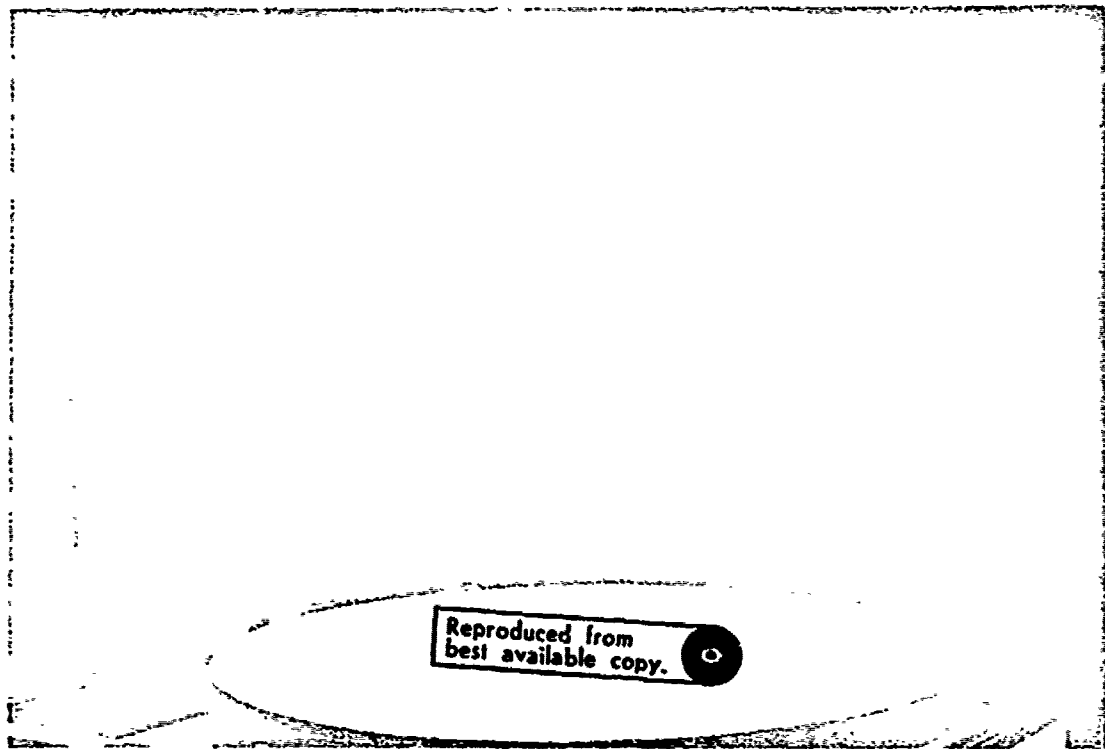


Figure 17. Collimated Light from Side Lights

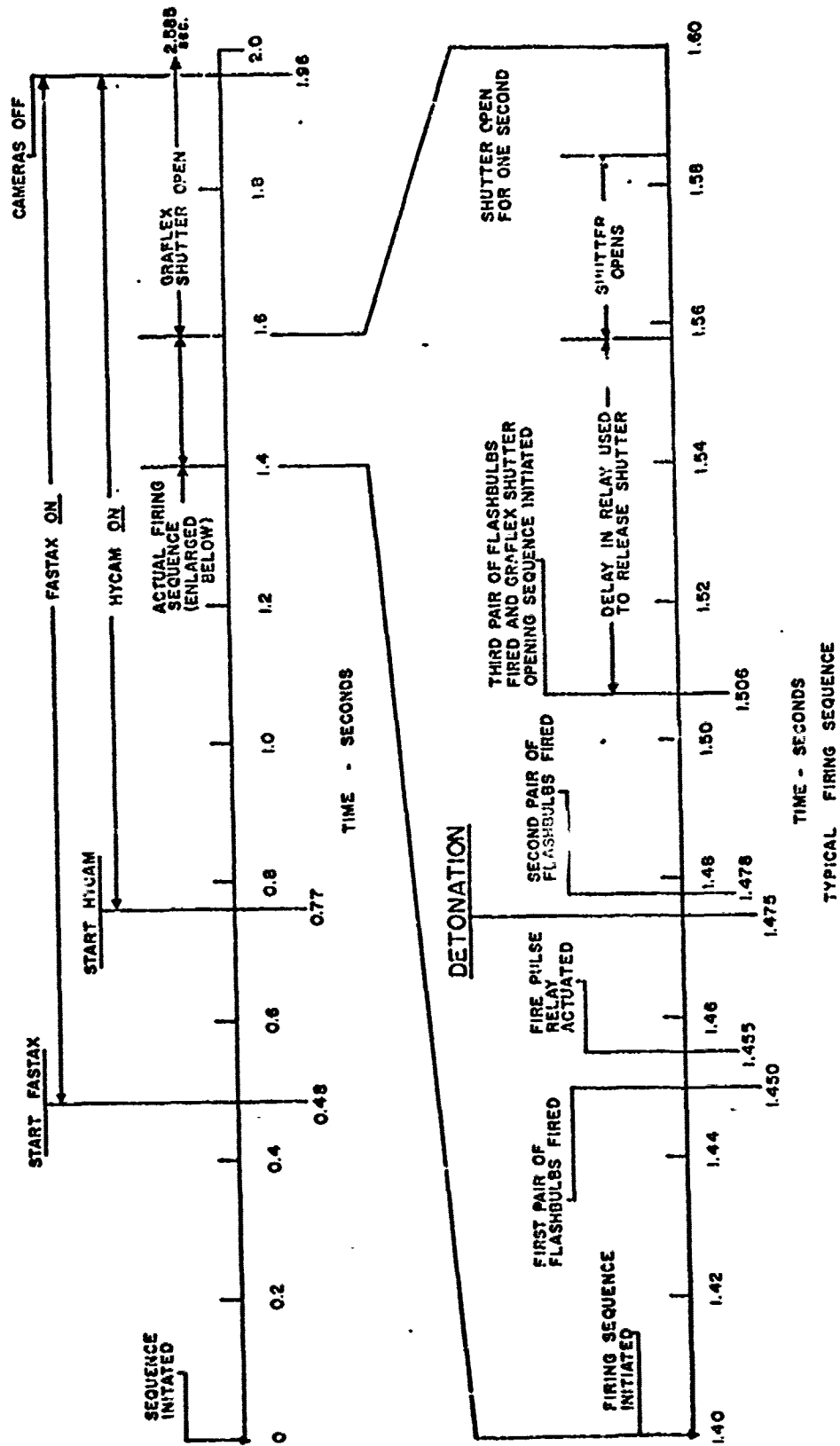


Figure 18. Typical Firing Sequence Diagram

by separate switches, three of which are on the control panel. They are the exhaust fan, the chopper-wheel motor, and the fiducial lights. The collimated side lights are controlled separately because of the high current (50 amps) necessary to power them.

Procedures

Standard procedures were developed for conducting the experiments since above surface bursts were being studied concurrently by the UDRI Staff. The shots were fired at a rate of about four per week, with the subsurface shots averaging about two per week. It was necessary to use the same basic procedures for both types of experiments. A demand-response checklist was devised to insure that all actions were completed properly and safely. See Appendix C.

Safety Precautions. Because of the danger involved with handling high explosives, special procedures were adopted. A storage safe for the lead azide charges was provided in the laboratory office in accordance with federal regulations. The charges were removed from the safe and prepared for firing by authorized personnel only. When handling the charges, protective face-shields were worn and care was taken to avoid any static-electricity-producing materials. A charge placed in the sand bed was not connected to the firing circuit until just before its scheduled detonation.

When sand was being loaded or unloaded, personnel working around the tank wore respiratory masks of pressed fiber to protect against inhalation of silica dust. Excessive exposure to this dust could produce silicosis. The exhaust fan was also used to help eliminate the dust problem.

Preparation of Test Bed. Each experiment was started with an empty tank. The conveyor was positioned under the elevated sand storage bin and a door in the bin was opened to a pre-determined point to control sand flow. Sand was distributed evenly throughout the tank until the surface was approximately 25 mm above the desired DOB. At that time the sand laying was stopped and the scraper was used to level the surface to the prescribed height. An area the width of the blade was scraped to the desired depth of burst. Accuracy of the scraper positioning was determined to be better than ± 0.5 mm (the diameter of a sand grain). Next, the charge was laid and centered with the use of the laser beam. The charge was first suspended by the lead wires from the sides of the tank along the normal to the line of sight of the cameras (90° - 270°). It was then lowered and pressed into the surface of the sand until the wires were tangent to the surface. The lead wires were pulled taut along the sand surface to the side of the tank and a small amount of sand was rained on top of the charge to insure its position. The wires were then taped to the top edge of the tank and more sand was rained into the tank to fill it. Again, the scraper was used to level

the surface over the middle of the tank to a depth of 3.2 mm below the top edge of the tank.

At this time, the aluminum grid was placed on the surface using the laser to identify SGZ. A taut string across the diameter of the tank was used to align the grid with the 90° - 270° radials. After the grid was placed, colored sand, approximately 9 mm deep, was metered into pre-determined squares to produce the desired grid pattern. After the colored sand was placed, white sand was poured over the entire grid and tamped slightly to consolidate it. The grid was then removed by attaching pliers to it and lifting it straight up. More sand was rained on the surface to increase the density of the grid and to fill the tank to just above the top. Once more, the scraper was used to strike the final surface, leaving a grid pattern as shown in Figure 10. The remainder of the surface was struck level with a rigid metal bar.

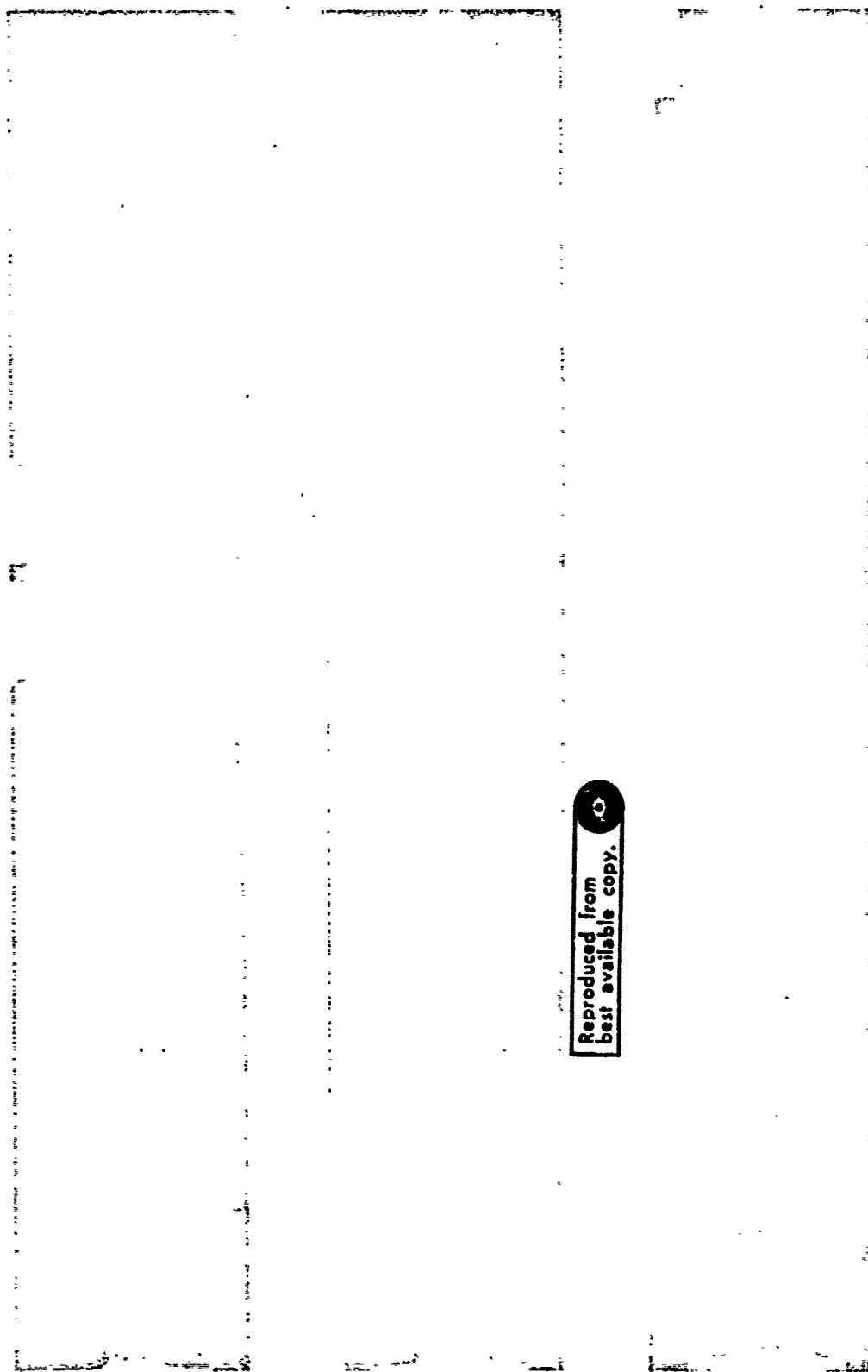
Final Preparations. While the sand bed was being prepared, the fiducials were checked and adjusted when necessary. As soon as the sand surface was completed, the cameras were focused and loaded with film, and the photographic lights were checked and adjusted. The firing circuit was checked for time sequencing with an oscilloscope. When all the systems were found to be satisfactory, the test room was cleared and one man soldered the charge wire to the firing circuit, turned off the room lights and closed the partition between the test area and the control room. The firing sequence was initiated and the shot was fired.

Camera Techniques. The Hycam camera took pictures of the mound growth and initial particle ejection (see Figure 19). The cameras were all located on the center-line of the tank with the grid lines parallel and perpendicular to the line of sight. Different patterns were tried to determine the optimum way to lay the sand grid. The final pattern had stripes, 3 squares long, parallel to the line of sight laid along the 90° - 270° radials (Figure 10). These stripes made it easier to follow the intersections of the colored and white sand as they crossed the horizon of the mound. The resolution was very good throughout the time of light.

The Graflex camera system was designed to record the paths of individual sand grains as they were ejected. Problems were encountered with this system and before they could be resolved, time became too short to include data as a meaningful part of this investigation. There was too much light from the flashbulbs at first and the pictures were overexposed. Also, there were too many particles to follow at the 120 fps of the chopper-wheel, making it difficult to determine which particle to follow, since the origin was unknown.

The Fastax was used primarily as a documentary camera and the film from it was not analysed for particle motion.

Post-Shot Operations. After the smoke and dust was cleared from the test area, the UDRI Staff took stereo pictures from above the crater for documentary purposes and for stereo analysis of



Reproduced from
best available copy.

Figure 19. Film Sequence of Mound Growth

crater dimensions, shape, and scouring phenomena. Ejecta data was also collected using glass catch tubes placed along 6 radials of the tank in the positions indicated in Figure 5. The crater depth was then measured manually with a profilometer designed specifically for the operation. Depth measurements were made at each 10 mm from SGZ along the 8 primary radials of the tank. These measurements were used to determine the crater dimensions. Table III lists the mean apparent dimensions of each of the craters resulting from the explosions studied in this investigation.

Table III

Mean Crater Dimensions for Varying Depths
of Bursts of 1.7 g Charges

Shot Number	Depth of Burst (mm)	Mean Apparent Radius (mm)	Mean Apparent Depth (mm)	Mean Apparent Crater Vol. (cc)
S- 15-23	5.08	113.47	30.94	619
S- 4-20	10.16	122.29	35.00	860
S- 68-15	15.24	120.82	44.75	868
S- 6-29	15.24	126.97	40.13	968
S-101-12	25.40	142.78	52.87	1592
S-104-24	25.40	144.47	51.31	1580
S- 25- 6	35.56	147.78	62.25	1742
S- 5-19	35.56	148.27	62.63	1835
S- 7-28	45.72	150.28	68.06	1950
S- 9- 7	50.80	164.74	71.00	2250

When the measurements were completed, the mixture of white and colored sand on the surface and the explosion residue in the crater were removed with the vacuum cleaner and discarded. The removal of these items maintained a uniform grain size and density for succeeding shots. The tank was then emptied by using the conveyor to fill the storage bin.

Exceptions to Procedure. The first two shots, S-25-6 and S-9-7, were fired under slightly different conditions from those designated above. The sand bed was laid in an octagonal plywood box with the same depth as the circular tank. The width of the box, between opposing sides, was the same as the diameter of the tank. The sand was "rained" into the box by using a mechanically-vibrated, sand distributor. The sand was metered from a hopper onto a slightly inclined metal plate, and the vibrations caused the sand to flow off the plate into the sand bed. The whole unit was moved across the bed via the rolling frame, mentioned previously. This process proved to be too time consuming and the new methods were developed. The only difference noted in the two systems was in-situ density. It was 1.75 g/cc in the old bed and 1.80 g/cc in the new bed.

IV. Data Reduction and Analysis

Data Reduction

After the film was processed it was put on a film reader where mound growth and particle motion were reduced to digital form for computer analysis.

Data Points. The data points were the intersections of the white and colored sand stripes as they crossed the horizon of the mound, as shown in Figure 20. The mounds formed in the experiments were assumed to be symmetrical. Therefore, the intersection lines were assumed to cross the horizon along the radial normal to the line of sight. These intersections were quite distinct until the

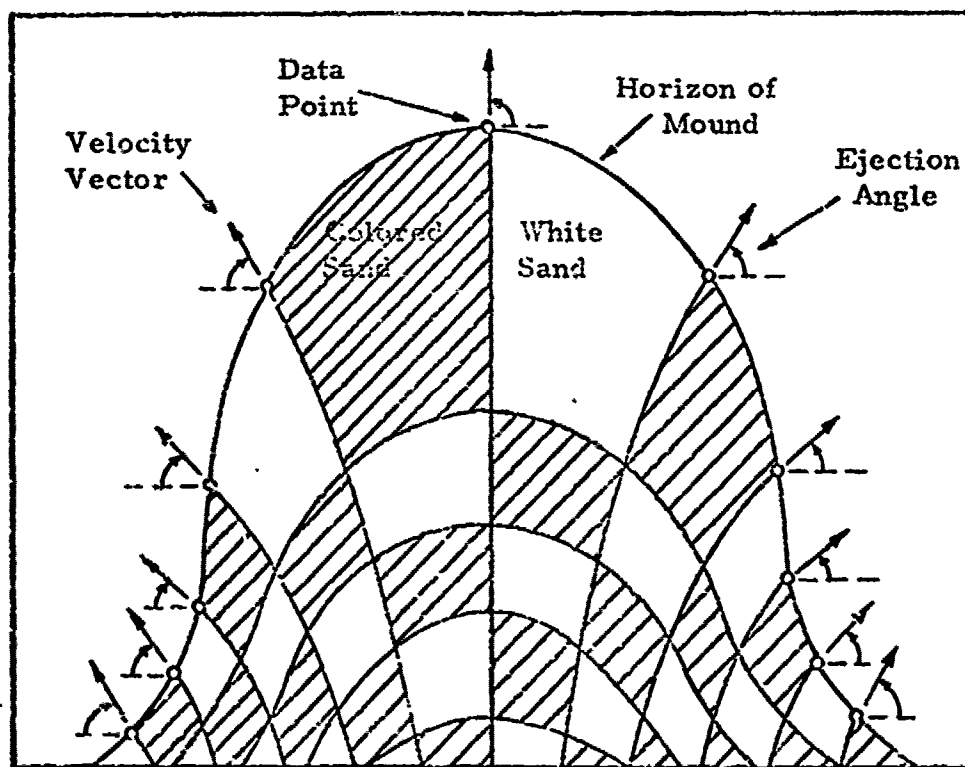


Figure 20. Illustration of Data Points on the Horizon of the Mound Along with the Velocity Vector and Corresponding Ejection Angle for Each Point

gas vented and even then, the outer points were not affected immediately.

The particles were followed from time of detonation to the time when the intersections could not be determined, or when they went off the film frame. When the intersections could no longer be determined, it was assumed that the particles were beginning ballistic flight. It would be at this time when the velocity and ejection angle of the particle would best determine the ejecta impact parameters. An example of the velocity vectors and ejection angles is also shown in Figure 20. The three center points were the only ones which went off the frame before the intersections could no longer be distinguished.

For the shallower shots there were no mounds as the spalling allowed the gases to vent. There was movement of the surface particles outside the region of spall, however, and those particles were followed until the intersections were no longer distinguishable.

Figure 19 shows a portion of the film from one of the deeper buried shots which illustrates the stability of the intersection lines as the mound grows. The accuracy of determining the position of the particles at the intersections is estimated to be within ± 2 sand grains. This was determined by selecting a particular point on the film reader in repeated trials. In the following discussions, "particle" and "line intersection" will be considered the same for all practical purposes when describing particle motion.

Depth of Burst. For ease in identifying various depths of bursts, multiples of the charge radius, $R_c = 5.08$ mm, were used instead of the specified measured depth.

Film Reader. The film reader used was a BOSCAR, a semi-automatic data-reduction machine made by the Benson-Lehner Corporation, Los Angeles, California (Ref 3). The BOSCAR projected the film on a rear-projection screen, which was approximately 53 cm square. The 16 mm film was magnified 31 times. An x-y coordinate system was established to provide position data for the surface motion. One fiducial was used as a zero reference point in each frame. A spot of light was aligned with the desired points on the screen by using a small control stick. Then, a record button was pressed which caused the x and y coordinate positions of the spot of light to be relayed to an IBM key punch which recorded the data on cards. Also recorded on the cards was the particle identification, frame, and shot number. The measuring unit provided an accuracy of $\pm 0.1\%$ at full-scale deflection, and image distortion was less than 0.05% (Ref 3-3).

Computer Programs. The computer data cards were used in two CDC 6600 programs for a least squares curve fit. The computer program which was originally designed to produce a linear fit to the data. It provided x versus time, y versus time, and x versus y plots along with the equation for the curve for each plot, the particle velocity, angle of ejection of each particle, and a summary of the output from all the points. An example of the output is shown in Appendix D. The program was altered slightly to provide for higher order curve fits, and the output included the same information mentioned

above except that the velocities and angles were computed for each frame and the summary was omitted.

Sources of Error. The errors induced in the data analysis should be small. Some error may have been introduced in reading the points from the film since an intersection point could be subject to some amount of arbitrary choice. This error should be minimal and random. Since the error of choosing any particular point is ± 1 mm, the error over a 10 cm trace should be less than 1%. The measuring unit itself induced only a 0.1% error in determining a point.

Magnification of the film reader was calculated from a test film of a meter stick which was placed on the surface of the sand at SGZ. The film was placed on the film reader and the reader coordinate system was converted to real space. The magnification error was less than 0.2%.

Some error could have been involved in the camera and lens, but precautions were taken to minimize these. The camera was set with the axis of the lens parallel to the surface of the sand bed. It was on the centerline of the tank and slightly higher than the surface. Points were read to the top edge of the film, so any lens distortion could have produced an error in reading the film. This error would have been of the same magnitude as mentioned in reading above.

Any errors produced in determining the velocities and angles in the computer programs should have been accounted for by the

standard deviations in the curve fits. It is estimated that the errors induced in the overall process were approximately $\pm 3\%$.

Data Analysis

Particle Velocity. Velocities and ejection angles calculated in the computer programs were analysed to determine relationships between depth of burst and radial distance of the particles from SGZ. Tables IV and V present results from first and second order curve fits based on the unsmoothed data. As the radial distances from SGZ increase, the velocities of the respective intersection points decrease systematically as would be expected. A log-log plot of particle velocity versus depth of burst indicates a linear relationship between the two, as shown in Figures 21 and 22. However, there was a direct relationship of velocity to the depth of burst at which the gas acceleration and spallation changed roles as the primary mechanism for ejecta. Of the shots fired in this study, this change was at a DOB of from $5 R_c$ to $7 R_c$. This is evident from looking at the graphs of Figures 21 and 22 showing results of the first and second order curve fits. For each equi-distance radial point along the surface, the velocity curve "breaks" at a DOB of approximately 30 mm or $6 R_c$ for both graphs. The velocities which had varied from increasing at the outer points to decreasing at SGZ, all began to decrease at this critical depth of burst. This particular depth is at approximately half of the optimum depth of burst.

Table IV
Particle Motion Data (First order least squares fit)

Shot #	DCH mm/R _c	Distance from Surface Ground Zero													
		0 cm	±0.60 cm	±1.27 cm	±1.91 cm	±2.54 cm	±3.18 cm	±3.81 cm	±4.45 cm	±5.08 cm	±5.72 cm				
		Vel m/sec	θ deg	Vel m/sec	θ deg	Vel m/sec	θ deg	Vel m/sec	θ deg	Vel m/sec	θ deg	Vel m/sec	θ deg	Vel m/sec	θ deg
15-23	5.08 1 R _c	718.0	89.9	*	*	99.1	41.0	30.0	42.9	9.9	48.3	10.7	57.1	4.7	60.2
4-20	10.16 2 R _c	393.2	89.6	*	*	86.9	41.0	30.5	44.6	9.2	61.7	8.5	50.6	3.9	73.5
68-15	15.24 3 R _c	294.6	89.6	*	*	53.1	47.5	24.0	44.8	20.7	49.7	10.4	55.0	10.4	55.0
6-20	15.24 3 R _c	232.4	89.7	*	*	54.1	47.0	25.1	46.4	19.6	42.6	11.1	48.0	11.1	48.0
101-12	25.40 5 R _c	104.7	87.2	*	*	54.7	47.1	25.5	46.4	20.7	49.7	12.1	52.2	12.1	52.2
104-24	25.40 5 R _c	109.9	87.5	106.9	72.9	49.3	55.7	26.6	54.3	23.4	52.3	13.1	55.4	13.1	55.4
25-6	35.56 7 R _c	60.1	88.1	47.5	74.3	41.2	55.0	30.2	52.7	18.1	52.3	13.7	56.6	13.7	56.6
5-17	35.56 7 R _c	59.0	89.1	41.7	68.4	54.5	55.9	29.2	52.5	18.8	52.0	14.2	67.5	14.2	67.5
7-28	45.72 9 R _c	30.4	88.9	48.9	71.3	34.0	61.4	23.2	64.4	20.6	59.3	12.9	60.1	12.9	60.1
9-7	50.80	24.2	85.4	49.7	70.7	32.8	63.3	22.4	57.4	20.5	57.9	13.8	54.1	13.8	54.1
				28.8	76.1	22.6	69.8	16.5	61.9	12.4	60.5	10.8	58.1	10.8	58.1
				28.6	77.5	23.2	67.0	17.4	61.3	10.8	58.1	8.9	64.4	8.9	64.4
				21.1	79.5	17.4	72.9	12.5	65.4	8.9	64.4	9.3	60.7	9.3	60.7
				23.1	80.9	18.0	71.4	13.6	68.9	9.3	60.7				

*insufficient data available

Table V
Particle Motion Data (Second order least squares fit)

Shot #	DOJ min/R _c	Distance from Surface Ground Zero														
		0 cm	±0.64 cm	±1.27 cm	±1.91 cm	±2.54 cm	±3.18 cm	±3.81 cm	±4.45 cm	±5.08 cm	±5.72 cm					
		Vel m/sec	θ deg	Vel m/sec	θ deg	Vel m/sec	θ deg	Vel m/sec	θ deg	Vel m/sec	θ deg	Vel m/sec	θ deg	Vel m/sec	θ deg	
15-23	5.05 1 R _c	*	*	118.8 90.9	42.0 46.6			36.6 36.9	40.9 43.6			14.5 13.4	31.6 35.2		5.7 7.1	62.6 8.4
4-20	10.16 2 R _c	409.0	87.6	*	*	45.2 42.4	45.2 52.9			28.2 26.2	43.1 42.5			12.4 15.5	31.0 23.1	
68-15	15.24 3 R _c	*	*	*	*	56.4 63.7	43.8 42.4			15.3 16.5	29.1 31.6			14.6 14.0	21.6 33.2	
6-29	15.24 3 R _c	207.7	39.8	*	*	60.2 59.8	47.3 48.0			25.6 25.1	50.0 45.4			16.1 17.1	35.1 40.5	
101-12	25.40 5 R _c	186.2	86.4	67.3 86.3	48.9 66.5	33.8 53.3	57.4 56.5			26.0 29.4	51.7 52.9			15.9 18.1	50.2 48.2	
104-24	25.40 5 R _c	169.9	85.5	52.4 41.7	58.5 56.3			29.2 28.3	54.1 54.5			19.1 20.0	50.3 45.1		14.5 14.8	41.5 41.5
25-4	35.56 7 R _c	70.3	37.3	44.5 50.9	66.1 70.3	38.4 39.3	53.1 66.6			21.9 29.4	50.9 59.4			14.3 18.0	59.1 40.6	
5-17	35.56 7 R _c	62.3	58.5	51.3 47.4	70.1 69.6	28.9 27.9	59.0 60.7			20.4 23.5	55.4 52.0			15.4 16.9	50.3 46.3	
7-28	45.72 9 R _c	32.7	89.0	29.7 29.4	76.1 75.0	25.4 22.5	66.0 67.5			18.1 17.0	57.6 57.6			11.1 13.7	56.1 48.9	
9-7	50.80 10 R _c	23.0	84.0	23.9	78.0	20.7 21.0	70.5 70.6			16.3 14.8	68.6 63.5			10.9 11.2	64.0 71.2	
† insufficient data available																

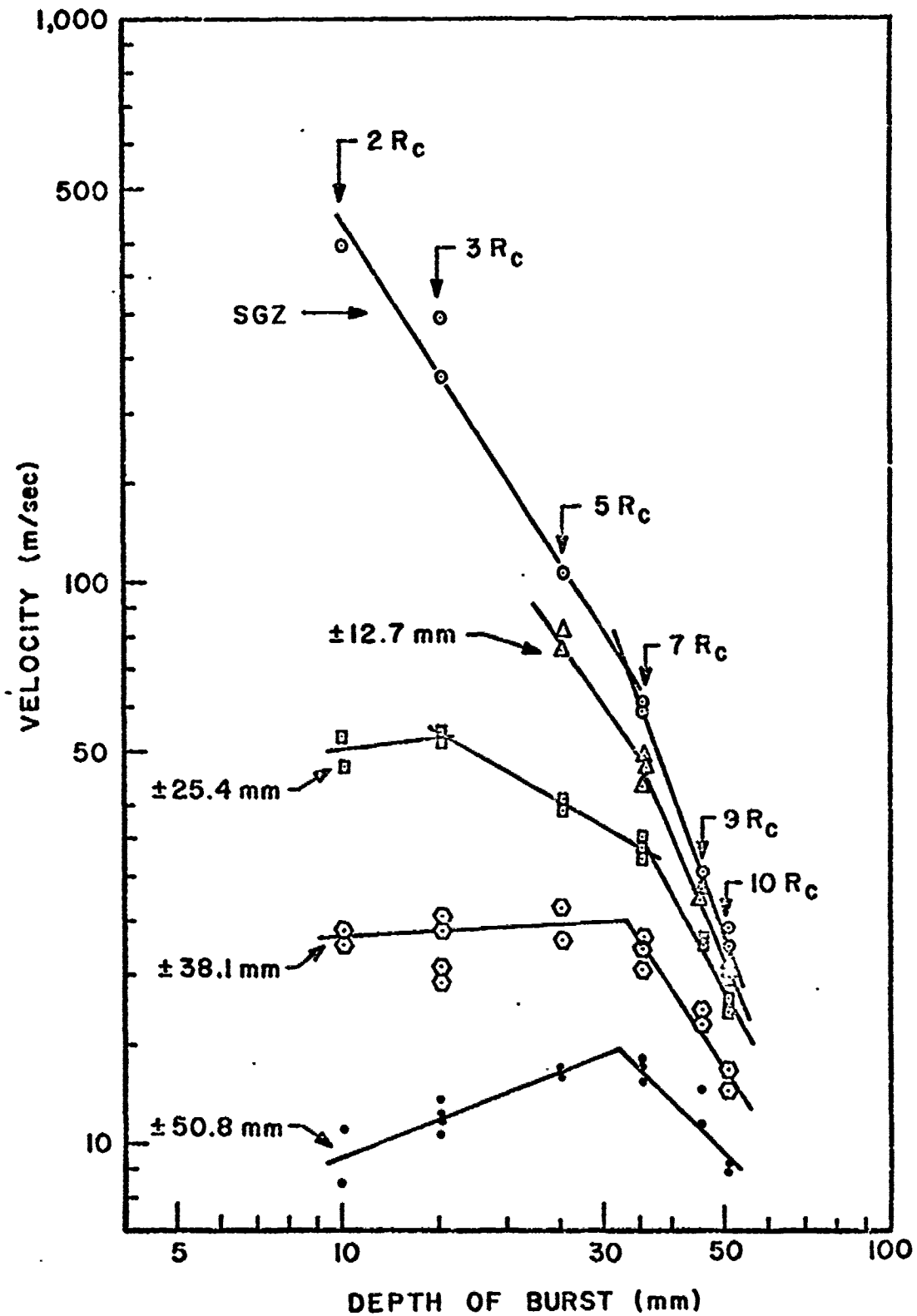


Figure 21. Velocity vs. Depth of Burst for Surface Particles at Specified Distances From Surface Ground Zero (first order curve fit)

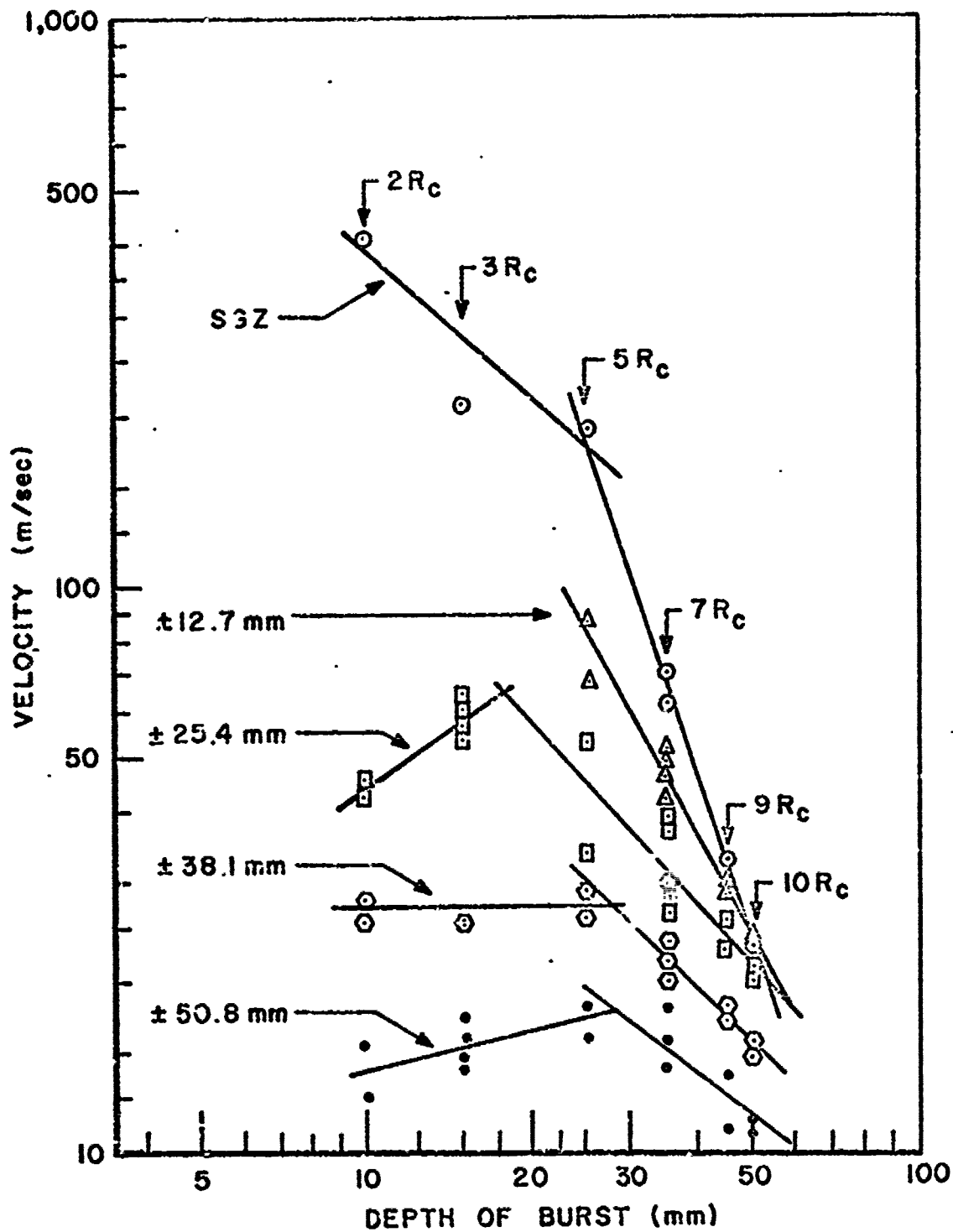


Figure 22. Velocity vs. Depth of Burst for Surface Particles at Specified Distances from Surface Ground Zero (second order curve fit)

(The optimum DOB being that which produces the greatest volume of the apparent crater.) The optimum DOB for these shots is estimated to be at about $10 R_c$, which is similar to that determined by Galbraith and Bessert (Refs 8 and 4).

Ejection Angle. The ejection angles computed were the angles made by the particle trajectories measured from a plane parallel to the horizontal surface. The ejection angle was the angle at the last point read, which, as stated before, was the point where the mound ceased to be intact and ballistic flight was assumed to begin. The general trend of the angle values was to increase with increasing depth of bursts as shown in Figures 23 and 24. The angle at SGZ was nearly 90° for all the shots, as would be expected. For the second order curve fit, the angles at the outer points (-50.8 mm and -57.2 mm) did not necessarily follow the trend. The angles at these points had a tendency to fluctuate.

Since the values listed in Table V are based on unsmoothed data, it was not uncommon to find the angle of a point to increase, decrease, then increase again. In the linear curve fit, the ejection angle was the angle of the assumed straight line fit to all the points and therefore not related to each individual point.

The angles of the points for the deeper shots ($5 R_c$ and below) were not significantly different for first and second order approximations. However, for the shallower shots the angles for the outermost points differed significantly because of the curved trajectories.

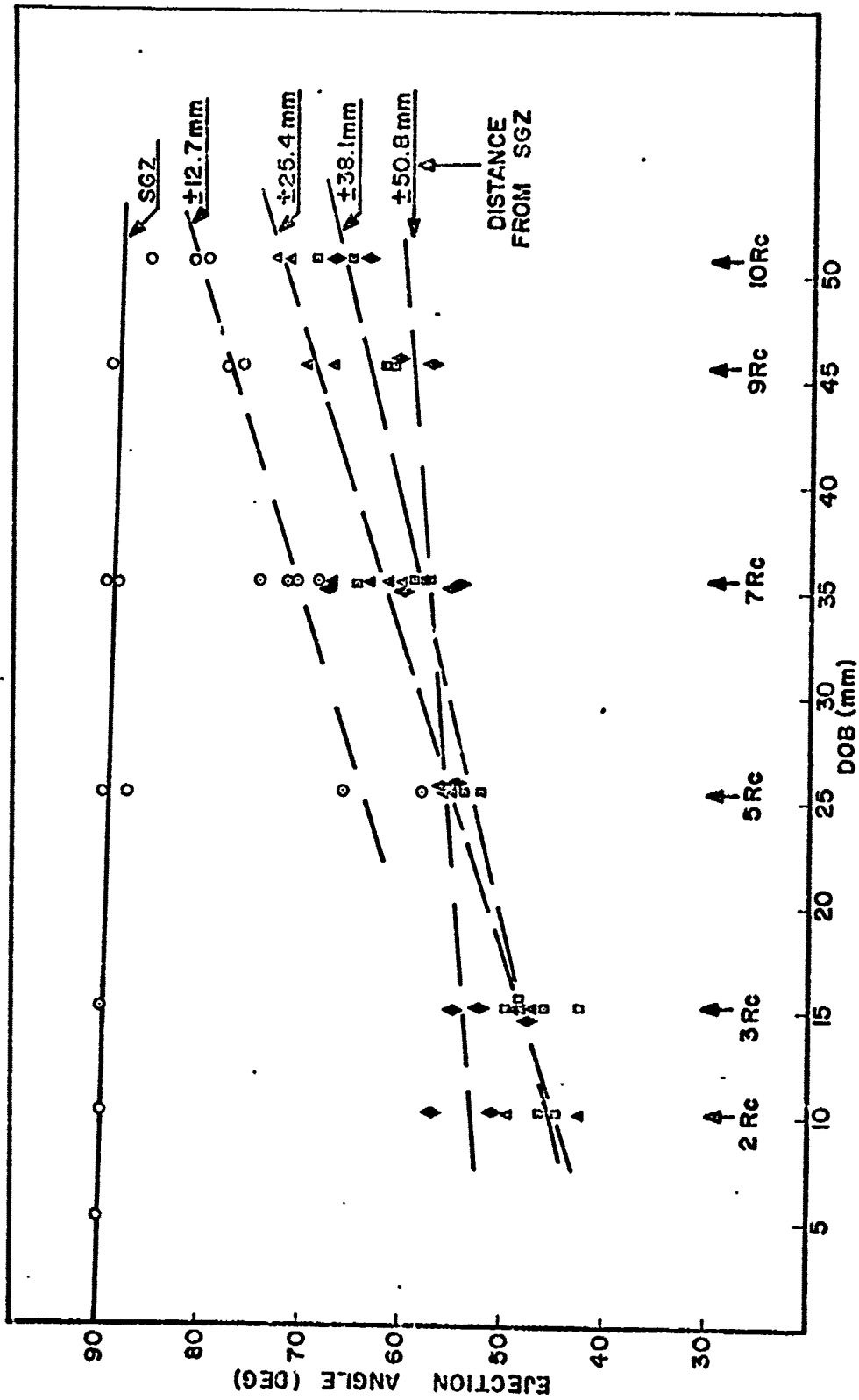


Figure 23. Ejection Angle vs. Depth of Burst for Surface Particles at Specified Distances from Surface Ground Zero (first order curve fit)

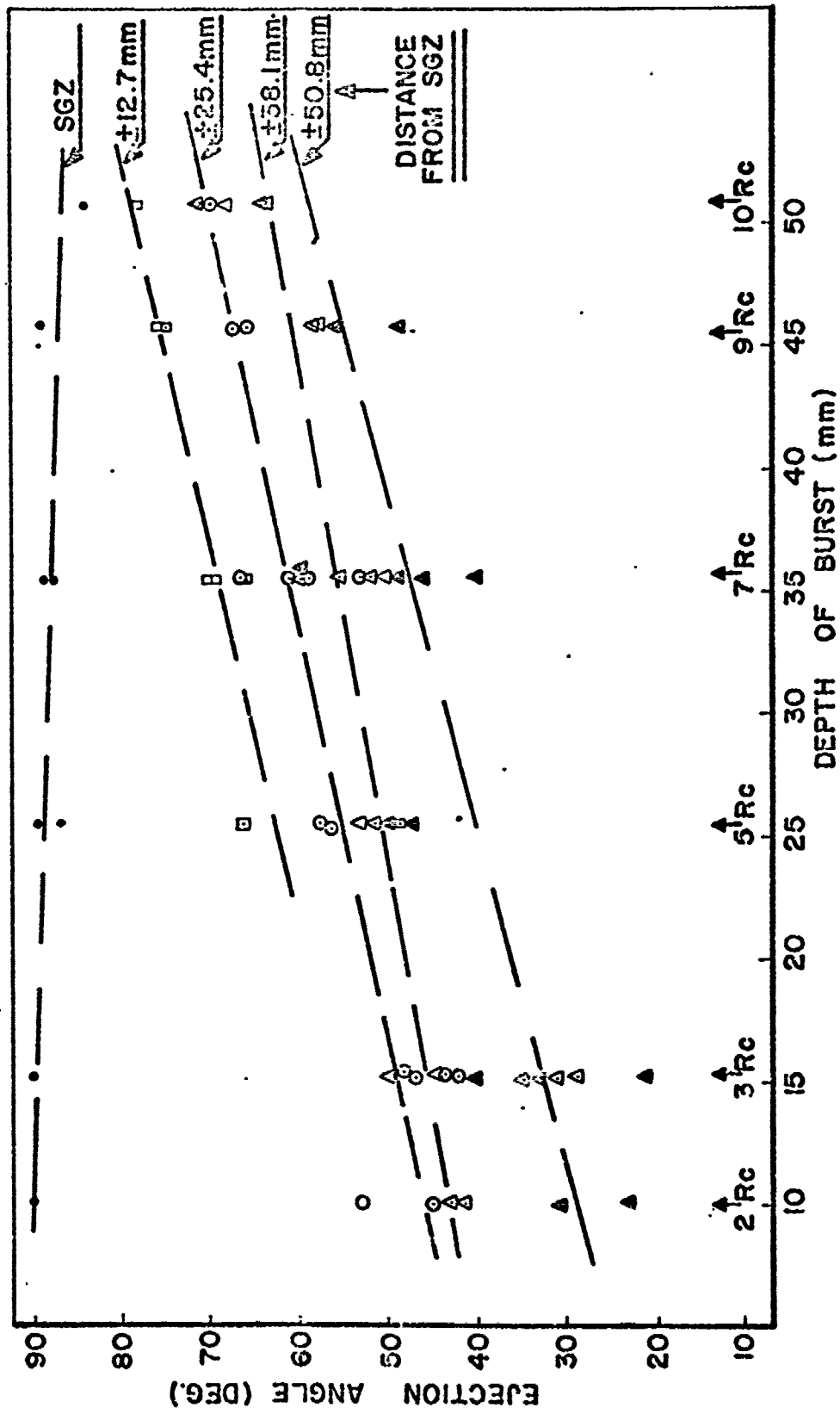


Figure 24. Ejection Angle vs. Depth of Burst for Surface Particles at Specified Distances from Surface Ground Zero (second order curve fit)

Here again, the depth of burst at which the predominant cratering mechanism changed from spallation to gas acceleration is evident.

When each shot is considered, the angles decrease from SGZ to the outermost points as is expected and a pronounced symmetry in the mound growth is observed. There is some scatter in the data points but it seems to be random in most cases. Shot number S-25-6, which appears to be biased throughout, may indicate a slightly off-centered charge.

Ejection Angle vs. Particle Velocity. Graphs were made plotting ejection angle versus particle velocity as shown in Appendix E. The graphs indicate a curved relationship of the points from SGZ out to 5 cm from SGZ, with the outermost points clustered in the angle range of 50° to 70° . If the point for SGZ is disregarded, a straight line can be approximated through the majority of the points indicating a systematic decrease in slope as the DOB decreases. This is not unlike the correlations indicated by Galbraith (Ref 8:37); however, the existence of the curve through all the points cannot be disregarded. There is a linear relationship of the radial distances of the different DOB's as shown in Figure 25, indicating a decreasing slope from SGZ to the farthest point. Again, between the DOB's of $5 R_c$ to $7 R_c$ a change is noted in the patterns from regular to unpredictable. Therefore the shallower shots were not included in the figure.

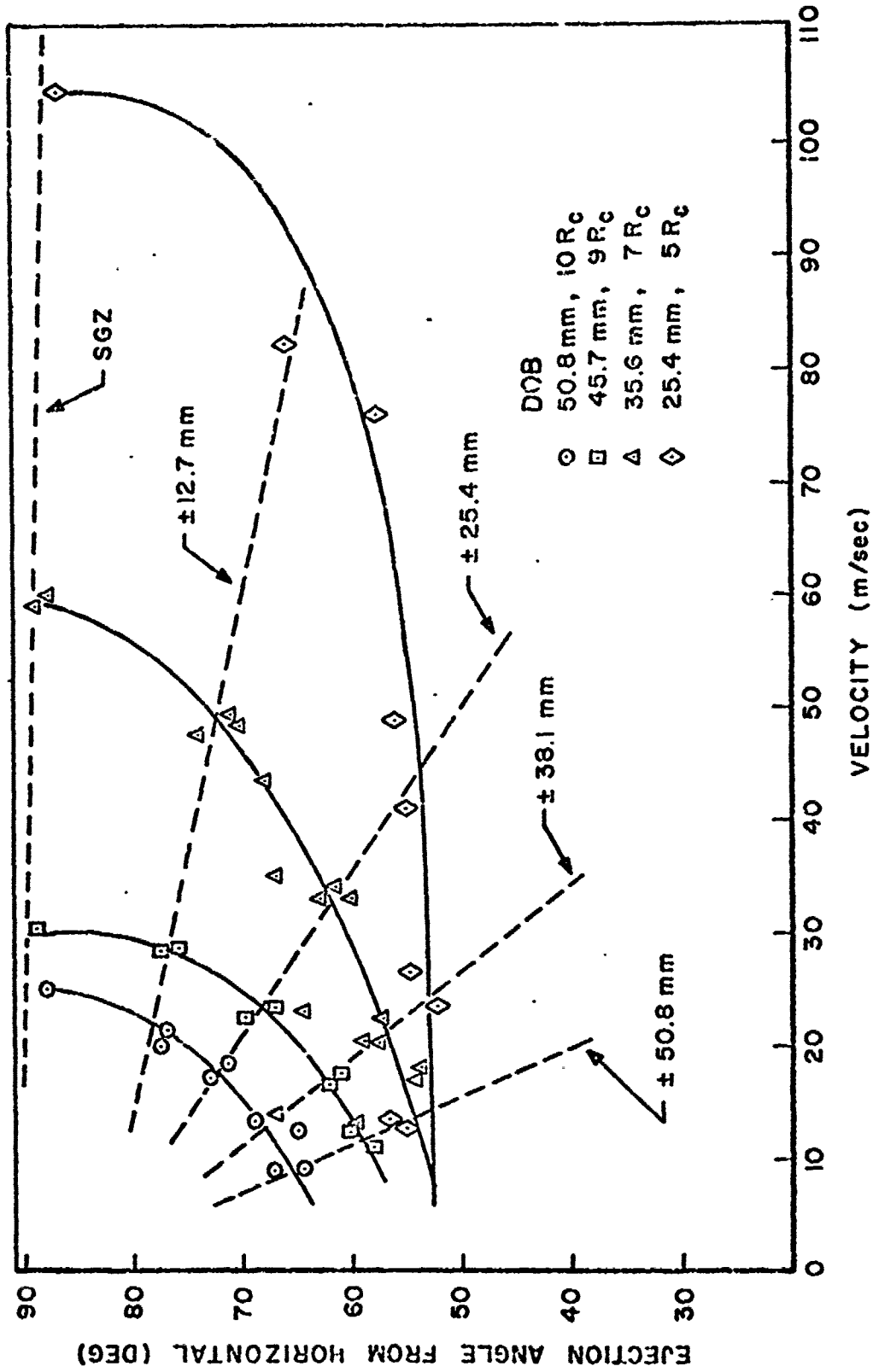


Figure 25. Family of Curves of Ejection Angle vs. Velocity for Surface Particles at Specified Distances from Surface Ground Zero

Mound Growth. A study of the mound growth produced by the deeper buried charges was made using the shape factor introduced by Galbraith (Ref 8:61). This shape factor, H/W , is the ratio of maximum height of the mound to the base of the largest triangle which will fit inside the mound as shown in Figure 26. Mound shapes were plotted using the data from the shots which had a DOB sufficient to form a definite mound. Time intervals of approximately 0.5 msec or 1 msec were used to form a reasonable response. An example of these plots is shown in Figure 27 and the remainder are included in Appendix F. Shape factors were then computed and plotted against time as shown in Figure 28. These plots appear to be linear for each particular shot with the slopes decreasing

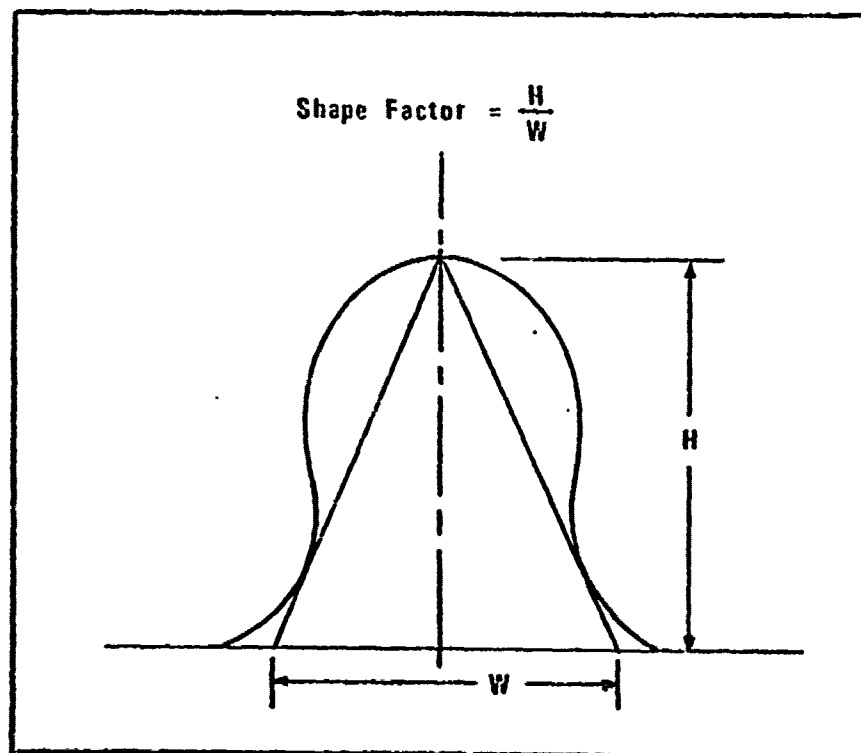


Figure 26. Definition of Shape Factor

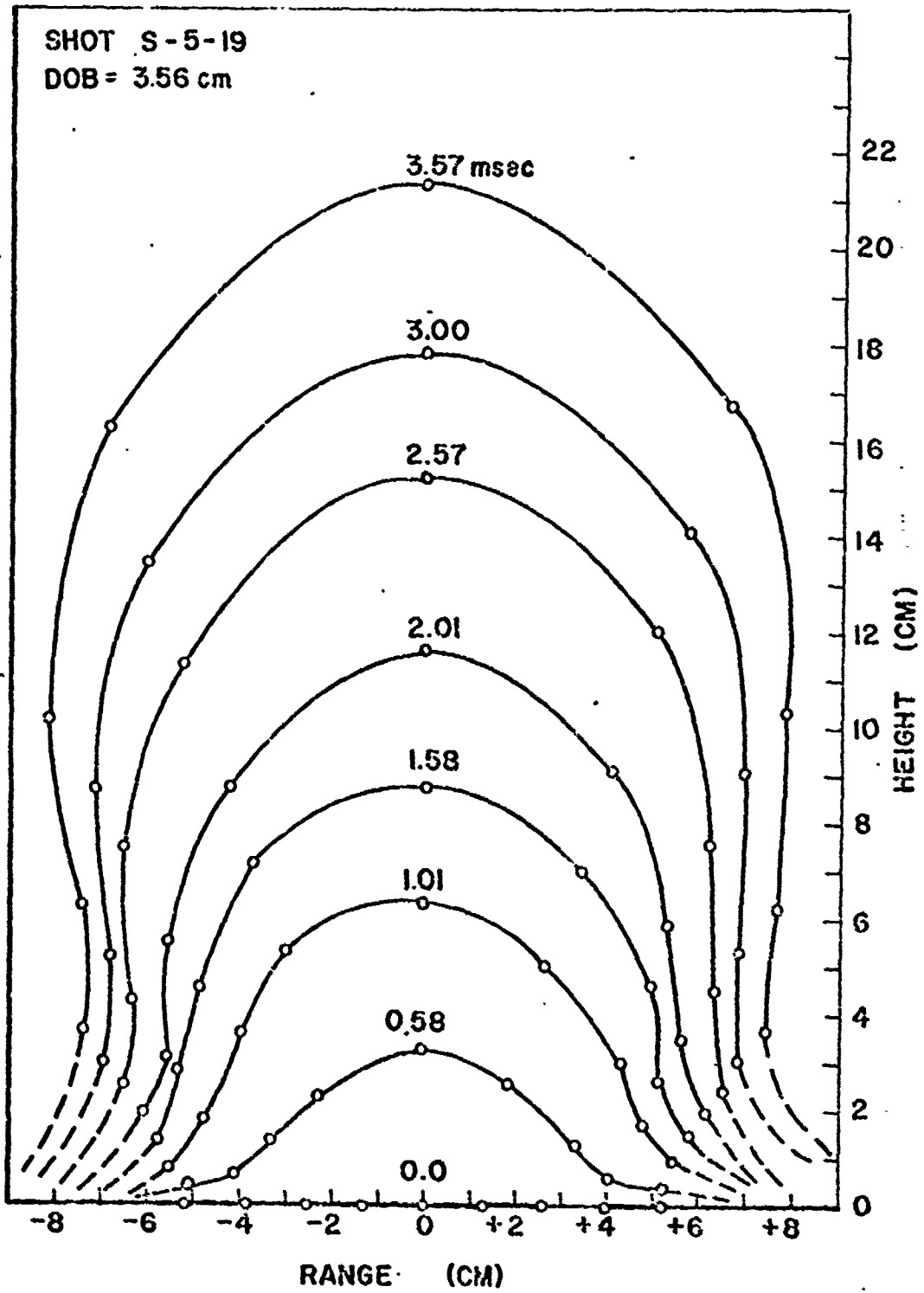


Figure 27. Example of Mound Growth for Shot S-5-19

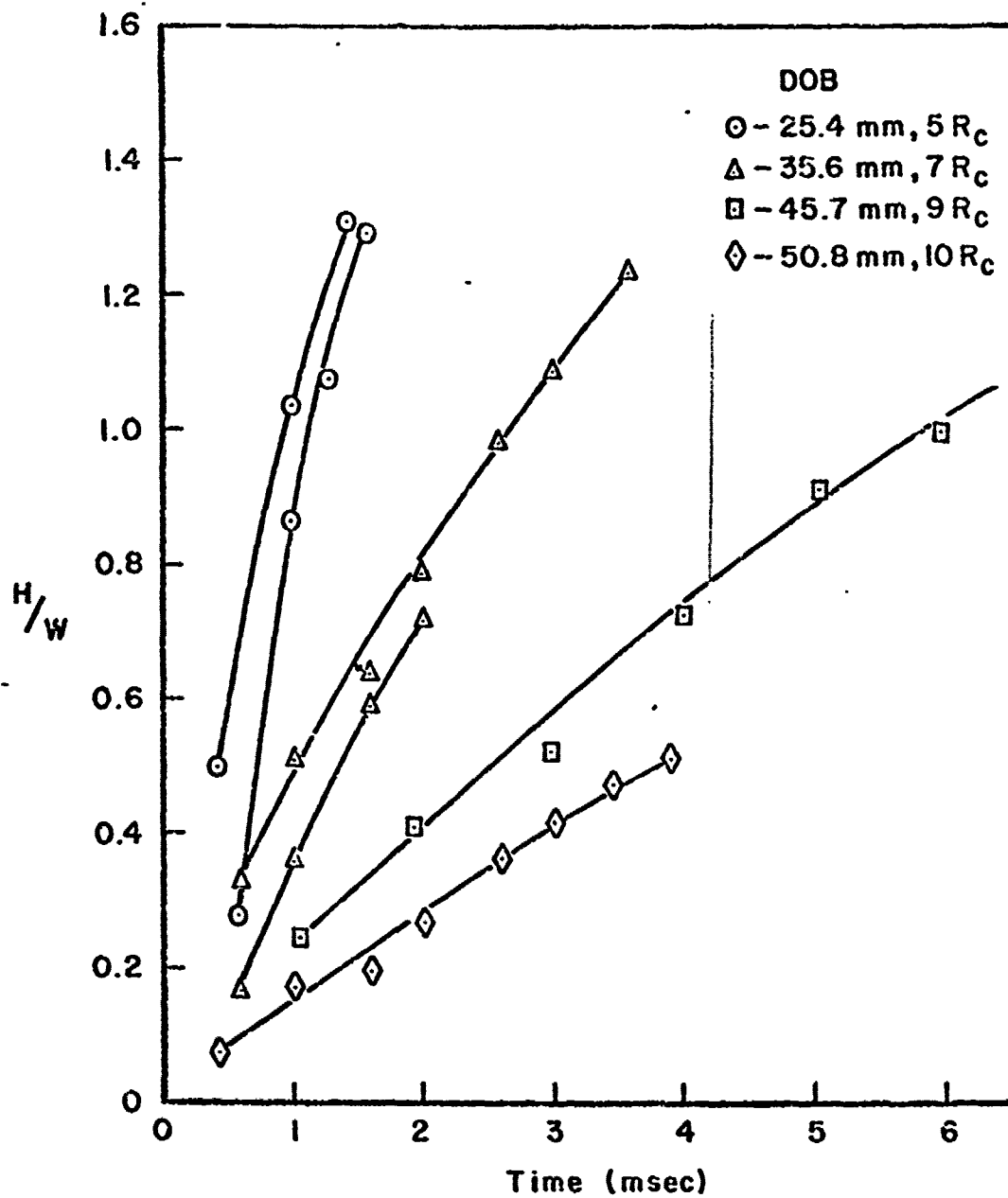


Figure 28 Shape Factor (H/W) vs. Time for 1.7 gm Charges at Varying Depths of Burst

systematically with DOB. The slope decreased by a factor of approximately 0.5 times the previous slope for each $2 R_c$ increase in depth. For example, the depths and slopes are as follows: $5 R_c - 1:1.5$, $7 R_c - 1:3$, $9 R_c - 1:6$, $10 R_c - 1:8$. The slope for the last depth decreased by 0.25 or 0.75 times the previous slope.

Comparison Analysis. In comparing the results with those calculated by Galbraith (Ref 8:49-50), the velocities in this investigation were 1.5 times the previous velocities for the points within 3 cm of SGZ, but correspond reasonably well for the outer points. Conversely, the ejection angles corresponded reasonably for the interior points, but for those points 3 cm from SGZ and beyond, Galbraith's angles were higher by 10° . A comparison of values is shown in Table VI. This indicates that the angles and velocities calculated from targets which do not match the size and density of the cratering medium do not produce the same results. However, further analysis of these results may indicate some systematic correlation which is not recognizable at this time.

One factor which may be the key is that the densities of the two studies were not the same. Galbraith used a sand bed with a density of 1.88 g/cc (117.5 pcf) (Ref 8:12), and most of the present data was taken from a sand bed of 1.80 g/cc. Two of the shots in the present data were made in sand which was at a density of 1.75 g/cc. Only one of these is comparable to another shot at the same depth and it does not show a trend like that which is apparent with Galbraith's data.

Table VI

Comparable Motion Data from Galbraith's and Present Studies

Data	Shot	DOB (min)	Dist from SGZ (cm)								
			±1.27 cm		±2.54 cm		±3.175 cm		±5.08 cm		
			Vel m/sec	θ deg	Vel m/sec	θ deg	Vel m/sec	θ deg	Vel m/sec	θ deg	
Present	-28 ^a	45.7	28.55	77.5	23.24	67.0	*	10.80	58.1	12.41	60.5
			28.76	76.1	22.56	69.8					
	-28 ^b	45.7	29.70	76.2	25.43	66.0	*	11.05	56.1	13.72	49.0
			29.41	75.1	22.51	67.5					
	-12 ^a	25.4	*		41.15	55.0	*	13.73	56.6	13.11	55.4
					49.27	55.7					
	-12 ^b	25.4	67.31	49.0	33.84	57.4	*	15.91	50.2	18.08	48.2
		86.33	66.5	53.30	56.5						
-24 ^a	25.4	*		*		29.23	52.5	*			
						30.23	52.7				
-24 ^b	25.4	*		*		29.26	54.2	*			
						28.31	54.5				
Galbraith's (Ref 8:49-50)			±1.0 cm		±3.0 cm		±5.0 cm				
			Vel	θ	Vel	θ	Vel	θ			
			m/sec	deg	m/sec	deg	m/sec	deg			
	21	46.5	*		*		9.27	65.8	9.71	64.3	
	22	46.5	19.30	82.6	15.43	71.5	8.52	66.7	10.10	66.4	
23	23.2	*		28.68	55.1	11.77	50.7	11.85	50.1		
				28.26	54.1						
24	23.2	*		27.80	55.2	12.06	51.2	12.80	53.3		
				28.17	57.8						

^a First order curve fit^b Second order curve fit

* Insufficient or no data available

Another factor to be considered is the fact that the velocities and ejection angles computed by Galbraith were calculated back in time for a particle at the original surface of the sand (Ref 8:37). This calculation would produce some variance since it was noticed in the present study that the surface particles tended to rise vertically for as long as 0.5 msec before the trajectory curved outward with the mound.

V. Conclusions

Laboratory Procedures

The equipment and procedures used in this study have improved the ability for data collection significantly over those of Galbraith and Bessert. It is felt that the method for filling the sand bed produced a more uniform repeatable density throughout the tank, than the method used by the previous investigators. The use of the grid pattern provided excellent reference points for following the surface particles. The fiducial lights made excellent reference markers which are easily focused on the film. The use of color film in the movie cameras provided better contrast for following the grid intersections on the mound. The collimated side lights reduced the bright-light area across the sand bed to about 0.08 that of the other experiments, providing an excellent section of the ejecta patterns. The problem of following the sand grains by this procedure still needs to be resolved, however.

Particle Velocity

The velocities imparted to the sand grains vary linearly with depth of burst when plotted on a log-log scale. As the DOB decreases from the optimum depth to a depth where gas acceleration and spallation change roles in the cratering process, $6 R_c$, the velocities increase for each point along the surface. At this indicated depth,

the slopes of the velocity curves for all the points begin to decrease with the outlying points decreasing faster than those closer to SGZ.

Ejection Angle

The ejection angles decreased systematically from 90° at SGZ to approximately 30° to 40° at the farthest points. The values increased for each point as the DOB increased. There was also an influence on the ejection angle observed at the 6-R DOB. The angles for equi-distant radial points on the surface indicated symmetry in mound growth.

Velocity vs. Ejection Angle

Particle velocity was plotted against ejection angle for each of the designated line intersections. A curve for each of the DOB's greater than $4 R_c$ indicated a linear relationship when the point for SGZ was neglected. The slopes of these lines decreased systematically with a decrease in DOB. Another linear relationship of the same point at different DOB's was apparent. The slopes of these lines also decreased as the points got farther away from SGZ.

Mound Growth

Mound growth was determined analytically by a shape factor, H/W. The shape factor was plotted against time, and a linear relationship for each DOB was apparent. The slope of the resulting line

decreased by a factor of approximately 0.5 times the previous slope for an increase of depth of $2 R_c$.

Comparison Observations

It is felt that the data and results from some areas presented in this study do not correlate well with those presented by Galbraith. There are significant differences in velocities of points within 3 cm of SGZ, and the ejection angles differ for the points beyond 3 cm from SGZ. The fact that the ejecta angles and velocities were affected by the DOB where gas acceleration and spallation changed roles to be the primary cratering mechanism was not observed by Galbraith because of the large changes in DOB in his study. This phenomenon caused a definite change from the linear calculations obtained from only the deeper shots in his study to at least a second order curve fit for the shallower shots. Velocity versus ejection angle did not yield an overall linear relationship, but the relationship of equi-distant radial points from SGZ are in fact linear for depths of burst where mounds result from the explosion.

VI. Recommendations

It is suggested that follow-on studies be continued in the small-scale cratering facility to better formulate the observations discussed in this study. The following recommendations are made concerning future investigations.

1. Reduce the number of and/or size of the holes in the chopper blade to decrease the number of sand grain trajectories visible in the Graflex film.
2. Make the chopper into a color wheel and use color film in the Graflex.
3. Use color film for all the movies, since it provides a better and easier film to read.
4. Try a few shots using both the grid pattern and some surface targets, such as glass beads, to try to correlate a definite relationship between them.
5. Re-evaluate the trajectory data from the gram-sized events using higher order least squares or Fourier series approximations.
6. Make a quantitative analysis of the results from laboratory experiments fired after the conclusions of this study.
7. Attempt to formulate the relationships discussed in this study for velocity vs. depth of burst, ejection angle vs. depth of burst, shape factor vs. time, and ejection angle vs. velocity.
8. Determine the significance of sand density in the results of these studies.

Bibliography

1. AFM 88-52. Control of Soils in Military Construction. Washington: Departments of the Air Force and the Army, September 1954.
2. American Society for Testing and Materials. ASTM Standards. Vol. 10. Baltimore: ASTM, 1968.
3. Benson-Lehner Corporation. Operations Manual for BOSCAR. Los Angeles: Benson-Lehner Corp., February 1956.
4. Bessert, Galen C. The Effects of the Variation of Charge Size and Depth of Burst in Laboratory Scale Cratering Experiments in Sand. Unpublished Thesis, Wright-Patterson Air Force Base, Ohio: Air Force Institute of Technology, June 1970.
5. Chabai, Albert J. "On Scaling Dimensions of Craters Produced by Buried Explosives," Journal of Geophysical Research, 70: 5075-5098 (October 15, 1965).
6. Christopher, William G. Analysis of Surface Motion Phenomena of One-Pound Zulu II Charges of Varying Depth of Bursts. NCG Technical Memorandum 66-14. Livermore, California: U. S. Army Engineer Nuclear Cratering Group, Lawrence Radiation Laboratory, July 1966 (revised May 1967).
7. Cook, M. A. The Science of High Explosive. New York: Reinhold Publishing Corporation, 1958.
8. Galbraith, Buren G. Motion Analysis of Small Explosion Cratering Events in Dry Ottawa Sand. Unpublished Thesis, Wright-Patterson Air Force Base, Ohio: Air Force Institute of Technology, June 1970.
9. Hansen, Spent M., et al. Recommended Crater Nomenclature. UCRL-7750. Livermore, California: University of California, Lawrence Radiation Laboratory, March 1964.
10. Herr, Robert W. Effects of the Atmospheric-Lithostatic Pressure Ratio on Explosive Craters in Dry Soil. NASA Technical Report R-366. Hampton, Virginia: National Aeronautics and Space Administration, September 1971.

11. Hess, Wilnot N. and Nordyke, M. D. "Throwout Calculations for Explosion Craters." Journal of Geophysical Research, 66:3405-3412 (October 1961)
12. Johnson, Stewart W., et al. "Gravity and Atmospheric Pressure Effects on Crater Formation in Sand." Journal of Geophysical Research, 74:4838-4850 (September 15, 1969).
13. Nordyke, M. D. "An Analysis of Cratering Data from Desert Alluvium." Journal of Geophysical Research, 67:1965-1974 (May 1962).
14. Nordyke, M. D. "Nuclear Craters and Preliminary Theory of the Mechanics of Explosive Crater Formation." Journal of Geophysical Research, 66:3439-3459 (October 1961).
15. Sogge, R. L. Transient Crater Ejecta Analysis. AFWL Working Paper. Albuquerque, New Mexico: Air Force Weapons Laboratory, June 1968.
16. United States Department of Commerce. Engineering Design Handbook, Explosive Series, Properties of Explosives of Military Interest. AMCP 706-1777, Washington, D. C.: Headquarters, U. S. Army Material Command, 1967.
17. Vortman, L. J. Surface Motion Photography. SC-RR-64-1703, Albuquerque, New Mexico: Sandia Corporation, 1965.
18. Westine, B. S. "Explosive Cratering." Journal of Terramechanics, Vol. 7, No. 2:9-19 (1970).
19. Wisotski, John. Technical Photography from Mine Under and Mine Ore Events of the Mine Shaft Series. DASA 2268 and DRI 2495, Denver: Denver Research Institute, University of Denver, May 1969.

Appendix A

MaterialsCratering Medium

Flint-Sno. Ottawa sand was chosen for the cratering medium primarily for correlation of data with previous experiments. It has been used by four or five different investigators and has demonstrated excellent predictability and symmetry in cratering experiments. As stated in Section III, there were other physical characteristics which made the use of Ottawa sand desirable. Its uniform size and lack of cohesion helped to produce a uniform density in the sand bed. These are also important factors in producing symmetric craters. The high reflectivity was important for the photographic techniques which were used. The measurements of the physical properties were primarily determined by using standard soil tests as described in Reference 2. The methods and results are described in the following discussions.

Grain Size Distribution. The grain size distribution of both the white and colored sand was determined by using the procedures in ASTM test C-136-67 (Ref 2:95). The sieve analysis performed utilized the U.S. Standard Sieve Numbers 20, 30, 40, 50, and 100. Six samples of white sand and four samples of colored sand were tested. The average values of white sand passing the sieves were: 99.5% passing #20, 59.6% passing #30, 3.7% passing #40, and 0.2%

passing #50. The average values for the colored sand was: 99.7% passing #20, 57.3% passing #30, 3.7% passing #40, and 0.1% passing #50. The values are depicted on the grain size distribution diagrams in Figures 29 and 30. The values indicate very little difference in the grain size distribution between the white and colored sand. Both types are classified as poorly graded medium sands, also known as uniformly graded sands.

Information taken from the two figures was used to determine the uniformity coefficient, C_u , and the coefficient of gradation, C_g . The terms are defined in the following equations:

$$C_u = \frac{D_{60}}{D_{10}} \quad (1)$$

$$C_g = \frac{(D_{30})^2}{D_{10} \times D_{60}} \quad (2)$$

where D_{10} = grain diameter at 10% passing

D_{30} = grain diameter at 30% passing

D_{60} = grain diameter at 60% passing (Ref 1:17).

The white sand had an average C_u of 1.39 and an average C_g of 0.95.

The colored sand had an average C_u of 1.37 and an average C_g of 0.94.

These values also designate the sand as uniformly graded. A uniformly graded sand is specified as one with a C_u less than 4 and a C_g less than 1 or greater than 3 (Ref 1:19).

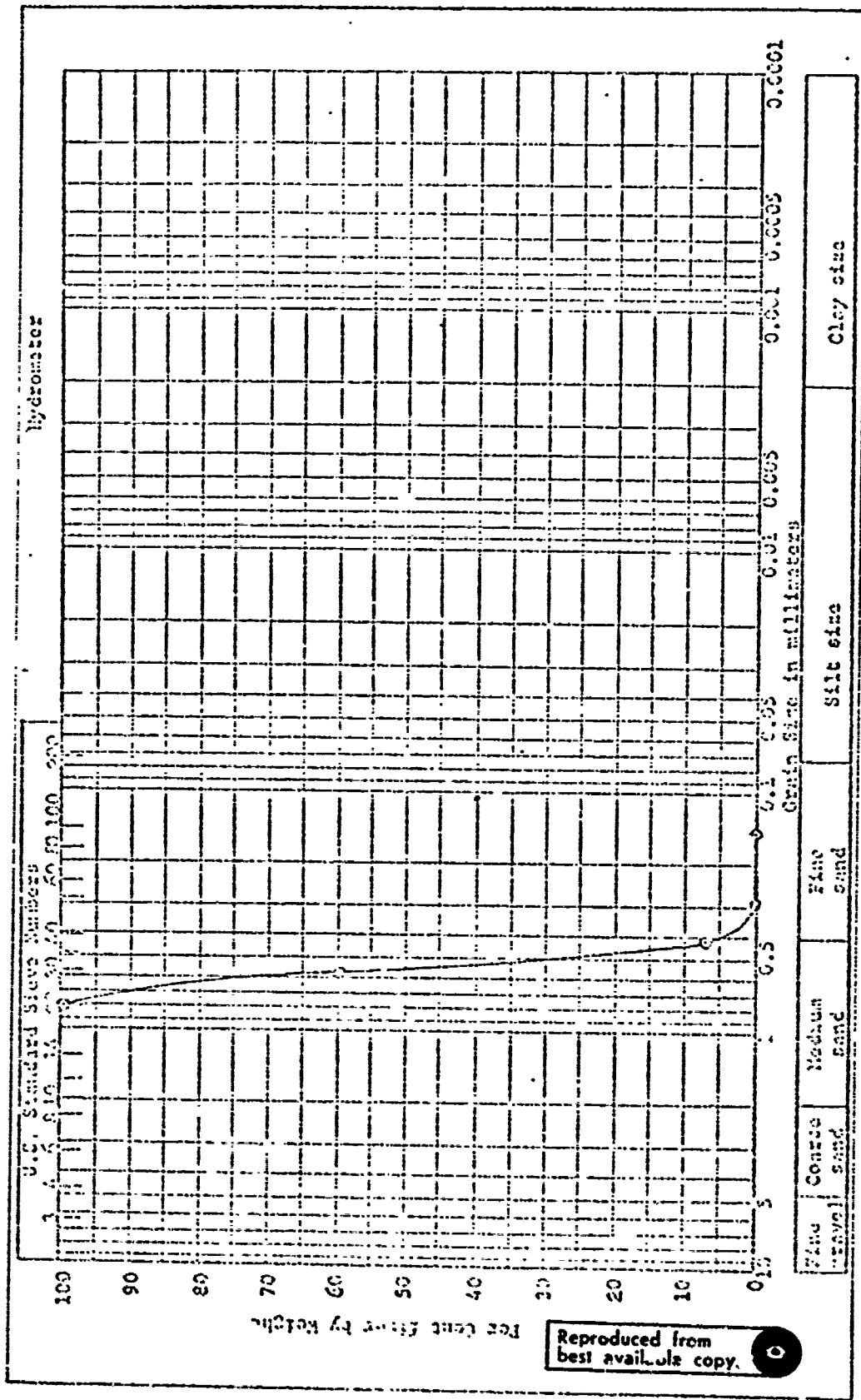
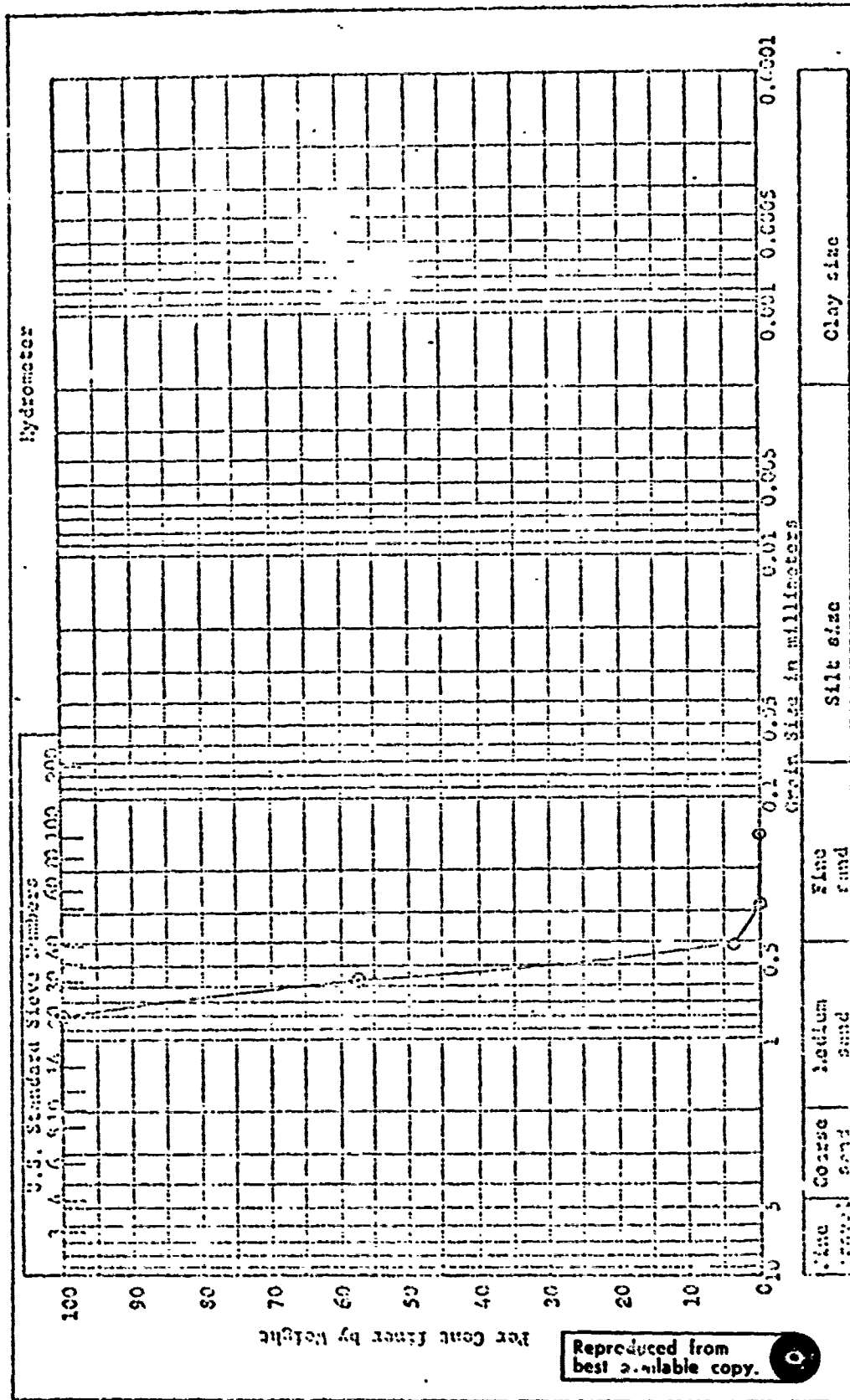


Figure 29. Average Grain Size Distribution for White Sand

Reproduced from best available copy.



Moisture Content. Moisture content was determined to be 0% by performing ASTM test D-1964-63 (Ref 2:510).

Specific Gravity. Specific gravity was determined by performing ASTM test C-128-68 (Ref 2:89). Using 6 samples, the average value was calculated to be 2.65 ± 0.01 .

Void Ratio and Porosity. Void ratio and porosity were determined from equations (3) and (4)

$$e = \frac{V_v}{V_s} = \frac{V(G_s)}{W_s} - 1 \quad (3)$$

$$n = \frac{e}{1 + e} (100\%) \quad (4)$$

where e = void ratio

n = porosity

V_v = volume of voids in a sample

V_s = volume of solids in the same sample

V = total volume of the sample

W_s = weight of the solids in the sample

G_s = specific gravity of the solids (Ref 1:23)

Void ratio is defined as the ratio of the volume of the voids to the volume of the solids, but it was easier to calculate using the second form of the equation. The calculated values were $e = 0.47$ and $n = 31.97\%$ in the dense samples and $e = 0.72$ and $n = 41.86\%$ in the loosest state.

Density. The density of the in-situ sand bed was determined by raining sand into metal containers placed at selected intervals and heights inside the tank. The containers were cylindrical in shape, 165 mm high and 127 mm in diameter, with an average volume of 1940 cc. Three tests were performed in the tank using 9 cans in each test. The cans were placed 36.8 cm from the side of the tank at successive 45° intervals around the tank. The first two cans were placed on the bottom of the tank on opposing radials. Sand was rained into the tank until the next level was reached, and then two more cans were placed 45° from the first set. This procedure was continued until the tank was full. The cans were carefully removed, struck level, and weighed. The volumes of the cans were determined by weighing the can full of water. The density of the sand was then calculated by equation (5)

$$\text{Density} = \frac{W_s}{V_s} (\gamma_w) \quad (5)$$

where W_s = weight of sand

V_s = volume of sand

γ_w = specific gravity of water

The calculated value of density at the surface was 1.80 g/cc for the circular tank. The density only increased by + 0.006 g/cc at the bottom of the tank.

The density of the sand in the plywood box was determined in the following manner. Eight cans were placed at 30 cm intervals along the centerlines of the box parallel and perpendicular to the direction of travel of the sand vibrator. Two cans were placed on the floor of the box and the other cans were set on pedestals of varying heights. The sand was then rained into the box until the cans were full; however, the entire box was not filled. This may have affected the determination of in-situ density slightly. The heights of the cans in each position were varied in the three tests to get an average density throughout the box. The cans were removed, struck level, and weighed and the density was determined as before. It was 1.75 g/cc.

Angle of Internal Friction. The angle of internal friction of Ottawa sand has been determined in previous investigations to be 37.5° . A direct shear test was accomplished on samples of the sand and the internal friction angle was found to be the same.

Explosives

The lead azide charges were manufactured by R. Stresau Laboratory, Inc., Spooner, Wisconsin. They were spherical charges with a diameter of 10.16 mm and a nominal weight of 1.7 g. The actual weight of each charge used, provided by the manufacturer, is listed in Table VII. The nominal density of the charges was 3.1 g/cc. The charges were coated with a 2 mil

Table VII
Weights of Lead Azide Charges Used in Experiments

Shot #	Weight (g)	Shot #	Weight (g)
S- 25- 6	1.7055	S- 4-20	1.7069
S- 9- 7	1.7037	S- 15-23	1.7052
S-101-12	1.6960	S-104-24	1.6947
S- 68-15	1.6946	S- 7-28	1.6927
S- 5-19	1.7014	S- 6-29	1.7069

layer of nitrocellulose and packaged in aluminum foil to provide protection from moisture, abrasion, and static electricity. A notched tungsten wire, 0.203 mm in diameter was used to centrally detonate each charge. The physical properties of lead azide at the charge density are listed in Table VIII.

Photographic Materials

Three types of film were used in the experiments. Both black-and-white and color film were used in the high-speed cameras. The black-and-white film was Kodak 2496 RAR, ASA 125, in 38.1 m (125 ft) reels. The color film was Kodak 7242, ASA 125, Ektachrome in 30.5 m (100 ft) reels. The Graflex camera used Kodak 6146 Super Panchro-Press, ASA 250, Type B film. This film was cut into 82.5 mm x 58.1 mm strips and loaded into a back-type cassette with a dark slide front. The results from all these films were excellent.

Table VIII

Physical Properties of Lead Azide

Composition:	Pb 71.2%, N 28.8%
Molecular Wt: (PbN ₆)	291
Density:	3.1 g/cc
Detonation Velocity:	4680 m/sec
Trauzel Test, % TNT:	39
Heat of Combustion:	630 cal/g
Heat of Explosion:	367 cal/g
Gas Volume:	308 cc/g
Heat of Formation:	-346 cal/gm
Specific Heat:	0.110 cal/g/°C
Thermal Conductivity:	1.55×10^{-4} cal/sec/cm/°C
Activation Energy:	23.74 kcal/mole
Sensitivity of Static Discharge:	0.007 Joules

(Ref 16:182-184)

Appendix B

EquipmentSand Laying Equipment

Tank Assembly. A circular steel tank, 9.5 mm thick, 76.2 cm high, and 148.6 cm in diameter was made for the sand bed container. The tank was set up and leveled to the nearest 0.13 mm by using a surveyor's level. The bottom of the tank was filled with 15.2 cm of concrete. The remainder of the tank was filled with sand. An angle iron frame was welded to the outside of the tank at the four primary radials. Figure 3 shows shows the relative positions of the tank and frame assembly. This frame had 23.1 mm circular rails mounted on the top of the side members to allow another frame to roll over the tank. The rolling frame, shown in Figure 3 in the stored location, was made of 11 mm x 102 mm, rectangular, steel tubing, 6.4 mm thick. This frame was used to hold the vibrator assembly, used in the old method of laying sand, and the scraper blade assembly discussed below.

Conveyor Unit. A special conveyor was used to fill and empty the tank. The unit consisted of a cleated rubber belt, a hopper at each end of the belt for controlling sand flow and a flexible plastic hose with a nozzle and control handle attached to it. The belt was driven by a 1/4-hp, AC motor mounted on the unit. The belt was 9.75 m long and 20.3 cm wide, with 5.1 cm-high cleats spaced at 30.5 cm intervals. It also had 5.1 cm-high

side panels along the entire length. The effective width was 10.75 cm. The pulley at the top of the conveyor was used to drive a flexible shaft which turned a small "squirrel cage" in the nozzle (Figure 8). The squirrel cage was 20.3 cm long and 15.2 cm in diameter and made of heavy gauge, 6.35 mm-square, wire screen. It turned at 140 rpm, breaking up the flow of sand coming through the nozzle. This action provided a uniform density of sand throughout the tank. The flexible hose was 1 m long and 10.1 cm in diameter. It had an aluminum handle, 1.5 m long, attached to it to provide for moving the nozzle across the tank. The hopper at the bottom of the conveyor fed the sand onto the belt and the hopper at the top fed the sand into the hose. The top of the conveyor was usually set at a height of 3 m above the floor which set the open end of the nozzle approximately 1 m above the top of the tank. The hose unit was detachable for ease in emptying the tank.

Surface Leveling Unit. A scraper was designed and built to accurately determine the height of the sand surface (Figure 9). The unit consisted of a triangular steel plate, 9.5 mm thick, a honed steel blade and a connecting rod. The triangular plate was clamped to the previously mentioned rolling frame and served as a stable base for the unit. The connecting rod, 45.6 cm long and 28.6 mm in diameter, fit through a sleeve in the base plate and was fitted with a screw clamp to provide elevation adjustments to the blade, which were accurate to within 0.2 mm. The blade was firmly bolted to

the end of the connecting rod. It was 50.8 mm wide, 60.2 cm long, with a 76.2 mm back plate. The blade had a 3° relief on the bottom so that only the leading edge scraped the sand. The blade was sloped on the top so that the thickness beveled up to 3.2 mm at the thickest part of the blade.

Aluminum Grid. The aluminum grid used for laying the grid pattern was 30 cm square and 12.7 mm high. The squares of the grid were 12.7 mm on each side.

Cameras

The two high-speed cameras were adequately described in Section III. The Graflex still camera was used to record particle trajectories at late time in the experiments. A chopper wheel was made to revolve in front of the Graflex, "chopping" the particle trajectories at 120 fps. The wheel was made by partitioning a circular metal plate into eight equal sections of arc. Every other section was cut out forming a fan-like wheel. The wheel was turned by an 1800 rpm, synchronous motor which was mounted in front of the camera stand as shown in Figure 13. The wheel was positioned at approximately 2.5 cm in front of the camera lens. A 1 sec time exposure of the particle movement was taken to produce the chopped trajectory on the film.

Photographic Light Fixtures

Photoflash Lamps. Two banks of three, synchronized, photoflash-lamp units were used to provide light for the movie cameras. The units were designed and built especially for this project. Each lamp was housed in a cubical aluminum box 27 cm on a side. The front of the box was cut out and a 26.7 cm -square fresnel lens was mounted to form the front. Each lens had a focal length of 216 mm. A socket was mounted inside the box at the focal point of the lens to provide for Press-22 and Press-50 flashbulbs. An access door for replacing bulbs was provided at the rear of each box. A two position switch was wired to the sockets to allow a choice of 24 v DC or 110 v AC at each box. The 110 v position was used in conjunction with a 100 w light bulb to focus the light onto the center of the tank before each shot. Once the lamp box was adjusted the bulb was removed and the switch was returned to the 24 v position for the normal firing sequence.

Fiducial Lights. Two fiducial marks were recorded on the Hycam film. These marks were the result of the fiducial light system which included a light source, lenses, and a reflecting glass. Two, small, 6.2 v, light bulbs were mounted behind two convex lenses which were attached to a metal frame. Each lens was 113 mm in diameter and had a 165 mm focal length. Two, thin, glass plates 120 mm by 140 mm were painted black. A narrow cross was scratched through the paint in the center of each, and one was mounted directly

behind each lens on the frame. The light coming through each cross and lens was focused onto a circular clear-glass plate mounted in front of the Hycon camera. The resulting crosses were reflected into the camera lens as shown in Figure 16. The reflecting glass was 15.2 cm from the camera lens and the distance from the glass to the fiducials was 3.99 m, the same as that from the glass to the center of the tank (SGZ). Thus, the fiducials and the event were both in focus on the film.

Collimated Side Lights. A bank of two lamps was installed at each side of the tank to illuminate a narrow vertical plane above the center of the sand bed (Figure 17). Each lamp consisted of two, high-intensity, 1500 watt, quartz lamps mounted behind a semi-cylindrical, water-filled, glass container used as a lens. Thus, a total of 12,000 watts of light was available for sand trajectory photography. The lens was 60.8 cm long and had a diameter of 8.9 cm. A sheet metal cover was bolted around this assembly. The cover had an opening 38.1 mm wide, the length of the lens. The distance from the face of the lens to SGZ was 1.60 m. The collimated light shining through the opening provided a vertical plane of bright light 30 mm wide at the center of the tank. These lights were designed to be able to follow particle trajectories captured on the Graflex camera. It took approximately 50 amps of current to power these lights, so they were wired into a separate circuit which was sufficient to carry the load.

Control Equipment

The control of the majority of the equipment items was accomplished from a single, integrated control panel. This panel was adjusted to control the automatic sequencing of the firing operation as shown in Figure 18. A typical sequence follows:

1. The sequence was initiated by manually turning a keyed activation switch and pressing a "Fire" button.
2. The Fastax camera started.
3. The Hycam camera started.
4. At 1.4 sec into the test sequence the firing sequence started.
5. The first pair of flashbulbs fired.
6. The fire pulse relay activated.
7. Detonation occurred.
8. The second pair of flashbulbs fired.
9. The third pair of flashbulbs fired and the Graflex shutter opening was initiated.
10. The shutter opened for 1 sec.
11. The Fastax and Hycam cameras turned off automatically.
12. The Graflex shutter closed.
13. The firing circuit was deactivated manually with the keyed switch.

Before each shot was fired the circuit timing was checked with an oscilloscope to insure control. In the firing sequence, the fire pulse was generated by the discharge of a bank of eight, 200 uf,

electrolytic capacitors wired in parallel. Electrical charge was allowed to build-up on the capacitors until a voltage drop of 160 v was measured. Then the capacitors were discharged causing the bridge wires to initiate the detonation.

Appendix C

CRATERING FACILITY CHECK LIST -- BEFORE FIRING!

Phase I -- in room #23

1. All doors CLOSED and LOCKED; fire extinguisher REMOVED
2. HIGH INTENSITY NARROW BEAM LAMPS
CHECKED for focus and power input -- all switches on back of lamps in UP position; lever Z3 in UP position.
3. PHOTOFLASH LAMPS
Switches at RIGHT HAND POSITION (24 v) and fresh lamps INSTALLED
4. GRAFLEX CAMERA
FOCUSED; F stop SET; shutter speed SET; shutter release mechanism COCKED; dark slide PULLED
5. HYCAM CAMERA
FOCUSED with focusing prism; LOADED; viewing slide SHUT; F stop SET
6. FASTEX CAMERA
FOCUSED with focusing film; LOADED with film tight on microswitch; viewing lever SHUT; F stop SET; on-off switch on camera top to ON position
7. Room lights OFF

Phase II -- in room #24

8. Power ON to fastex pulse generator; signal output ON
9. Voltage SET on fastex power box; rear door SHUT TIGHT against microswitch

GSF/MC/72-6

10. Power ON to hycam pulse generator; signal output ON
11. Hycam voltage regulator SET; switch ON
12. STANDBY on panel breaker #15 for high intensity lamps

Phase III -- fire control panel

13. AC power ON; keyed power ON
14. Charge continuity TESTED
15. Fire position PLUGGED IN
16. Sequence knob SET
17. 110V lamp focus switch OFF
18. Graflex light chopper ON
19. Overhead exhaust fan ON
20. Fiducial light switch ON
21. Charge to desired voltage and signal for breaker #15 to ON before initiating firing sequence

Appendix D

Examples of Computer Printouts for One

Particle Trajectory

Program Hycam (first order least squares fit)

HYCAM
 REDUCED DATA
 SHOT NO. S-68-15
 ITEM NO. 8

A = 12.1079 VELOCITY 11.307 M/SEC STANDARD DEVIATION .1237 CM
 THE VELOCITY DEVIATION IS .311 M/SEC (2.75 PERCENT)

FRAME NO.	X POS. CM	TIME MSEC	DEVIATION CM
0	12.514	0.000	0.000
1	12.486	.143	.215
2	12.486	.285	.055
3	12.571	.429	-.021
4	12.571	.572	-.183
5	12.686	.715	-.231
6	13.029	.853	-.050
7	13.229	1.002	-.012
8	13.371	1.145	-.032
9	13.486	1.290	-.080
10	13.800	1.434	.071
11	14.000	1.573	.103
12	14.257	1.722	.202
16	14.771	2.301	.062
20	15.314	2.882	-.052
24	15.971	3.465	-.054

Figure 31. Computer Tabular Print for x-Velocity

SHOT NO. 5-50-15 ITEX 0

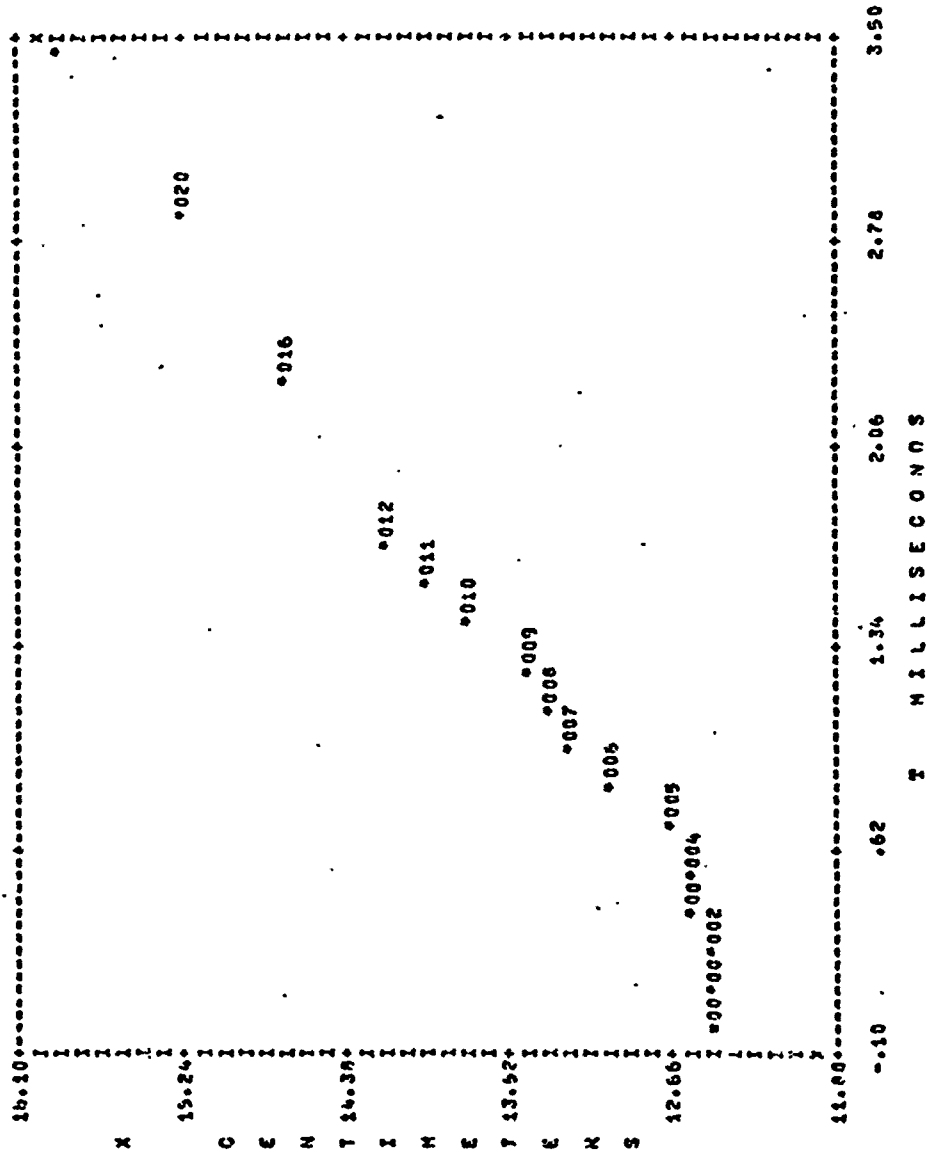


Figure 32. Computer Graph Plot for x-Velocity

HVCAM
 REDUCED DATA
 SHOT NO. S-69-15
 ITEM NO. 8

A = -14.0037 VELOCITY 13.220 M/SEC STANDARD DEVIATION .1821 CM
 THE VELOCITY DEVIATION IS .427 1/SEC (3.23 PERCENT)

FRAME NO.	Y POS. CM	TIME MSEC	DEVIATION CM
0	-14.006	0.000	-.062
1	-14.029	.143	-.214
2	-13.829	.285	-.202
3	-13.600	.429	-.163
4	-13.314	.572	-.065
5	-13.057	.715	.091
6	-12.829	.859	.040
7	-12.629	1.002	.050
8	-12.371	1.145	.113
9	-12.057	1.290	.242
10	-11.857	1.434	.251
11	-11.657	1.573	.261
12	-11.571	1.722	.156
16	-10.885	3.301	.075
20	-10.314	2.882	-.120
24	-9.771	3.465	-.363

Reproduced from
 best available copy.

Figure 33. Computer Tabular Print for y-Velocity

SHOT NO. S-66-15 ITEM 8

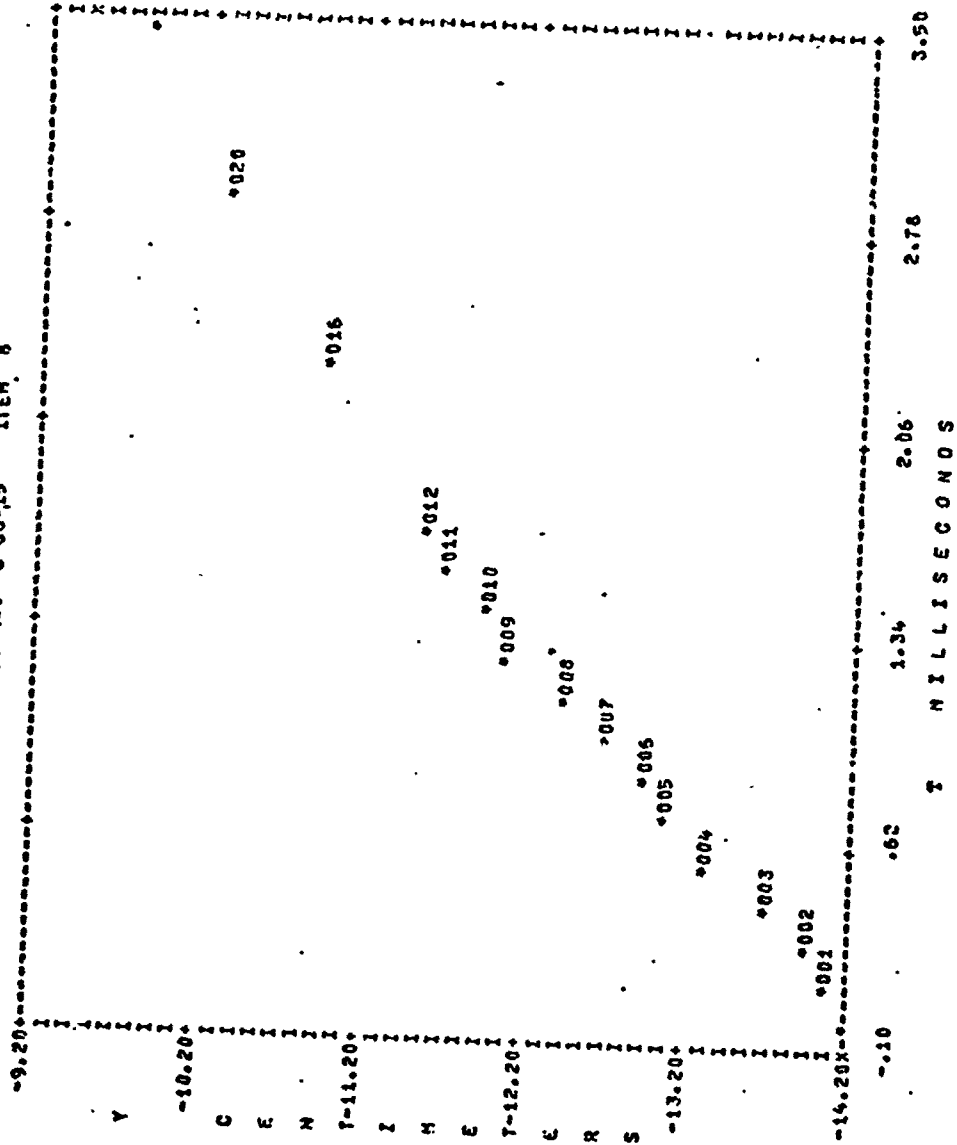


Figure 34. Computer Graph Plot for y-Velocity

HYGAM
 REDUCED DATA
 SHOT NO. S-68-15
 ITEM NO. 3

A = -27.880 ANGLE 48.967 DEG STANDARD DEVIATION .2210 CM
 THE ANGLE DEVIATION IS 1.342 (2.74 PERCENT)

FRAME NO.	Y POS. CM	X POS. CM	DEVIATION CM
0	-14.086	12.514	0.000
1	-14.029	12.446	-.495
2	-13.829	12.435	-.295
3	-13.600	12.571	-.165
4	-13.314	12.571	.121
5	-13.057	12.686	.247
6	-12.822	13.029	.092
7	-12.629	13.229	.052
8	-12.371	13.371	.145
9	-12.057	13.485	.328
10	-11.857	13.800	.167
11	-11.657	14.000	.137
12	-11.571	14.257	-.073
16	-10.886	14.771	.022
20	-10.314	15.314	-.030
24	-9.771	15.371	-.243

Figure 35. Computer Tabular Print for Ejection Angle

SHOT NO. S-88-15 ITEM #

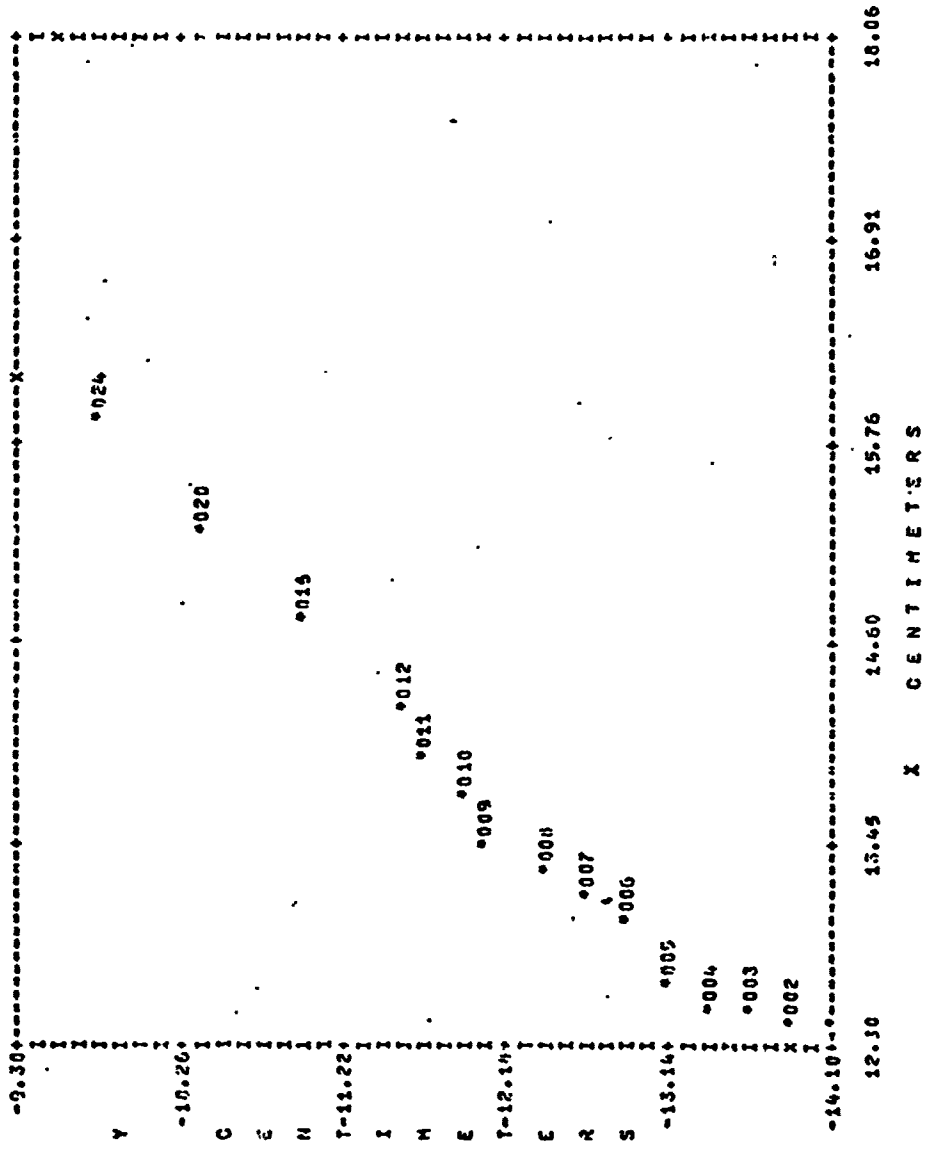


Figure 36. Computer Graph Plot for Ejection Angle

Appendix E

Graphs of Ejection Angle vs. Velocity for

Depths of Burst from 5.08 mm to 50.8 mm

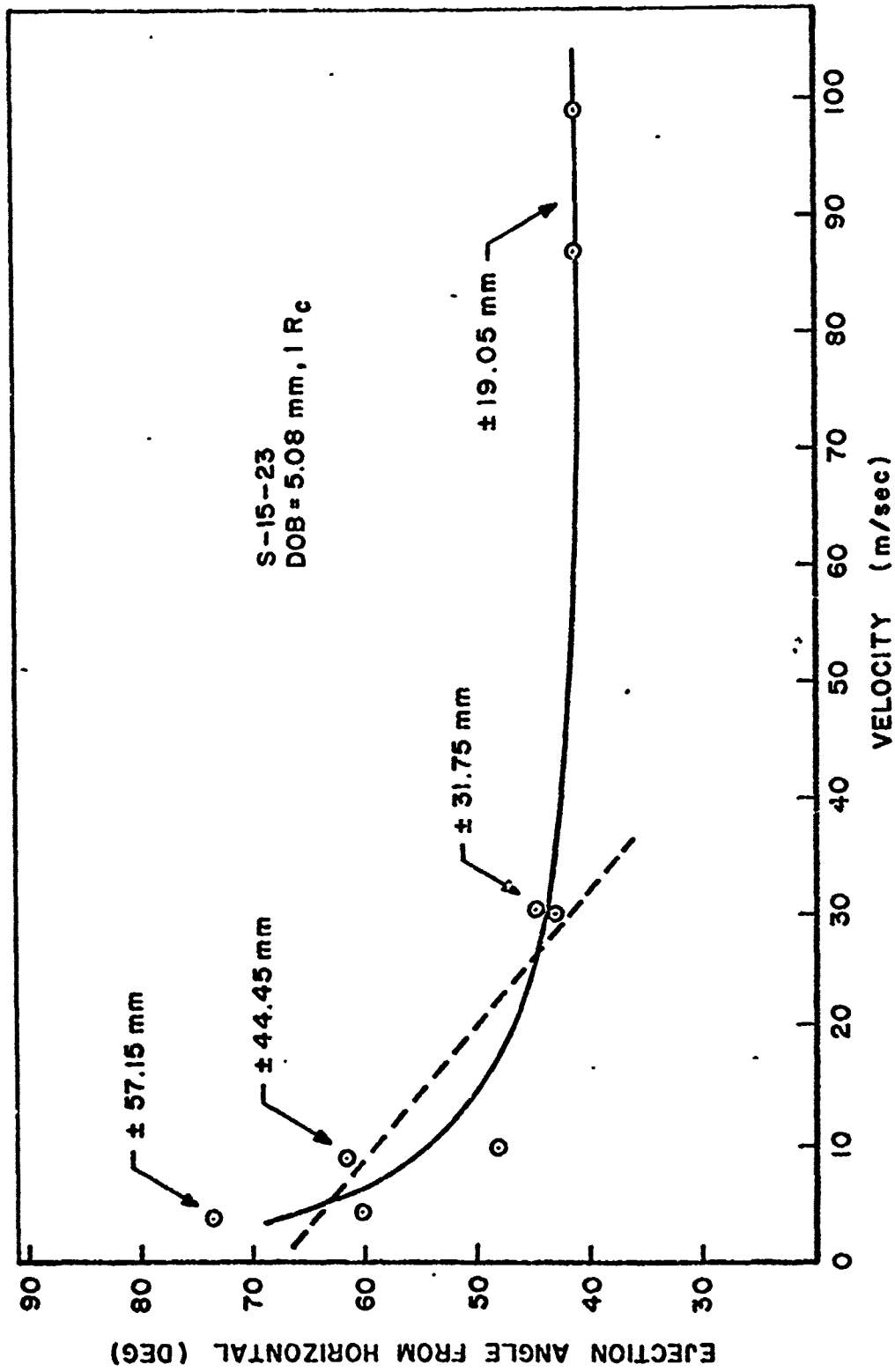


Figure 37. Ejection Angle vs. Particle Velocity for DOB of 5.08 mm

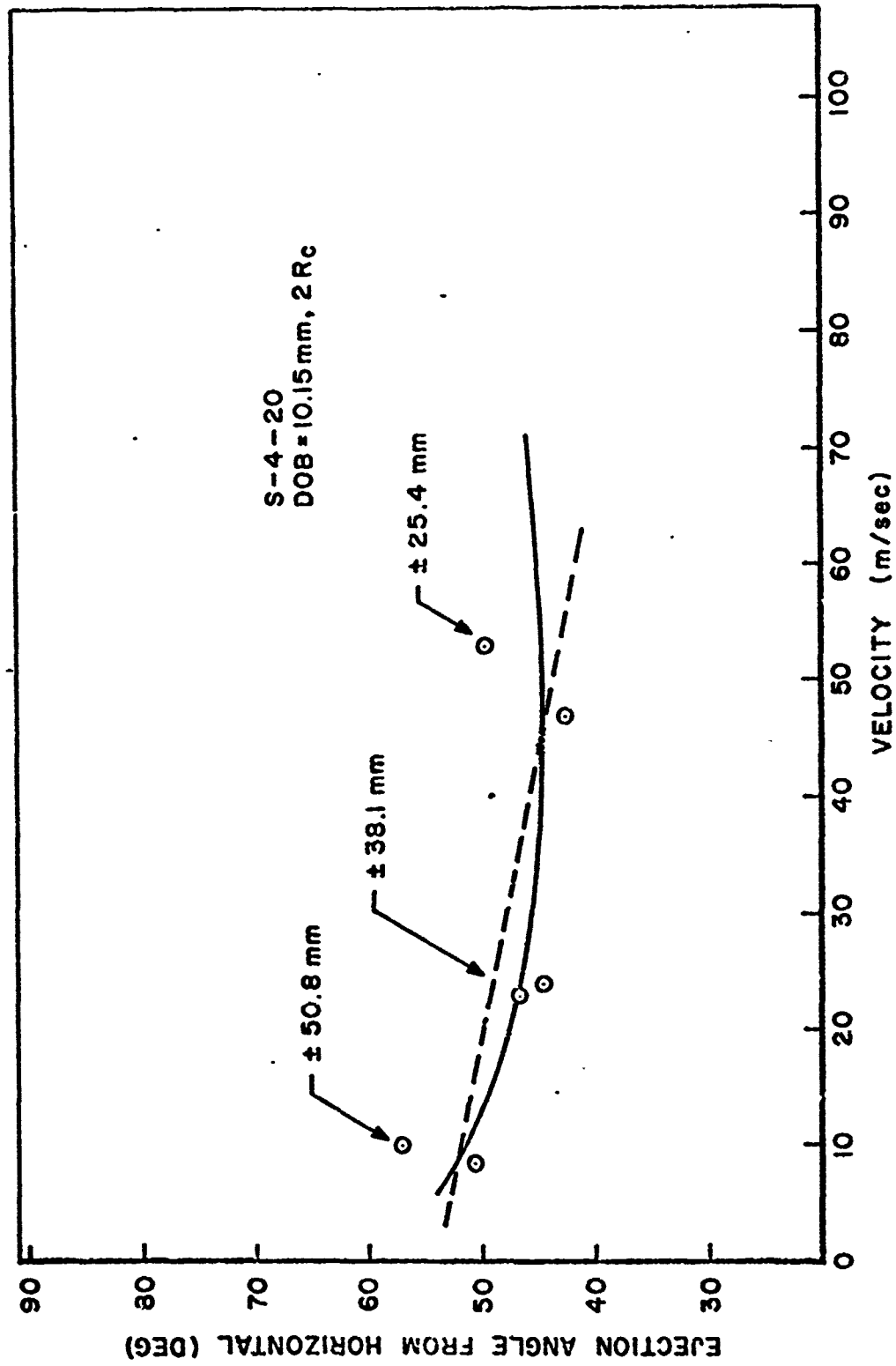


Figure 38. Ejection Angle vs. Particle Velocity for DOB of 10.15 mm

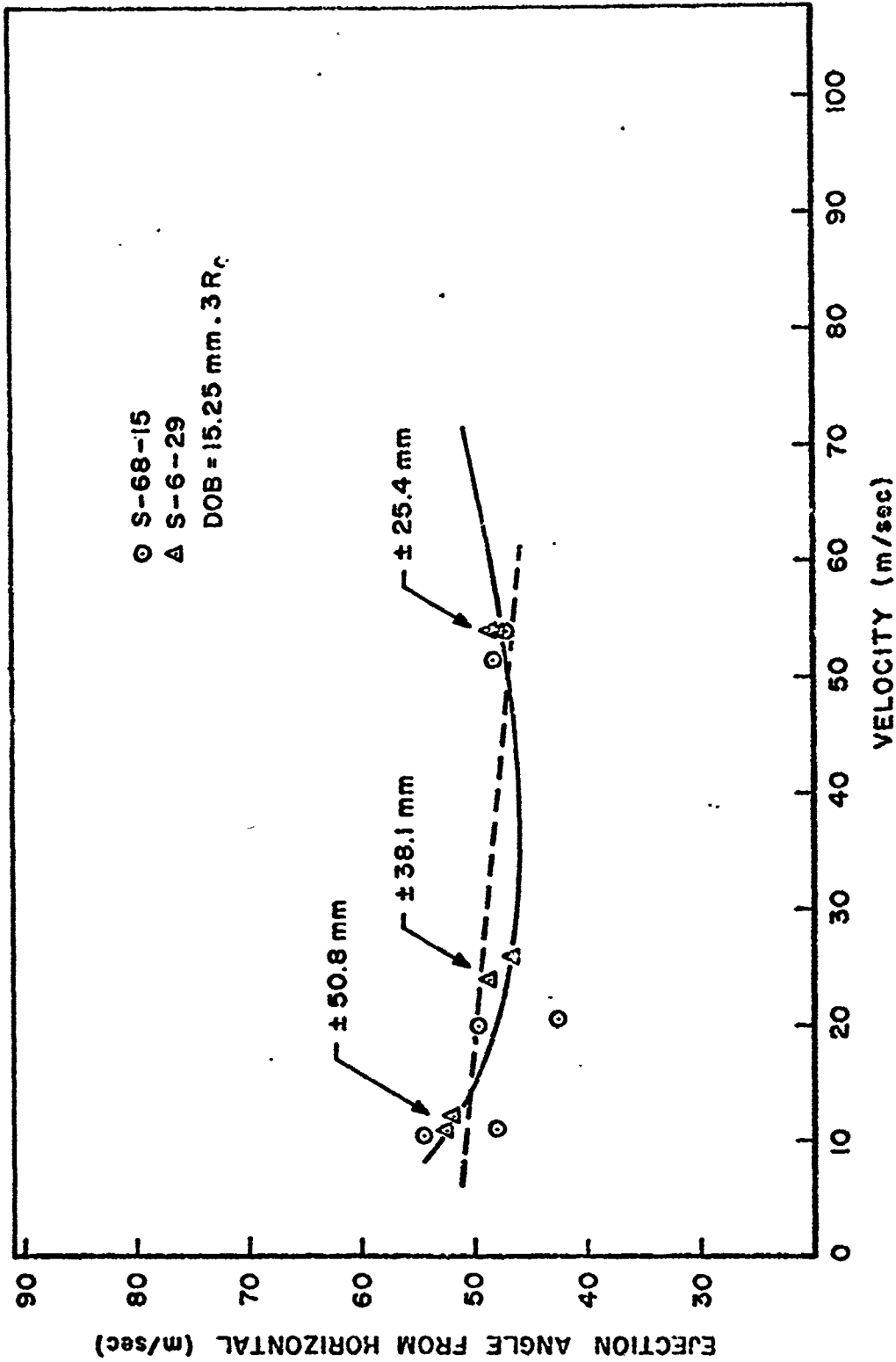


Figure 39. Ejection Angle vs. Particle Velocity for DOB of 15.25 mm

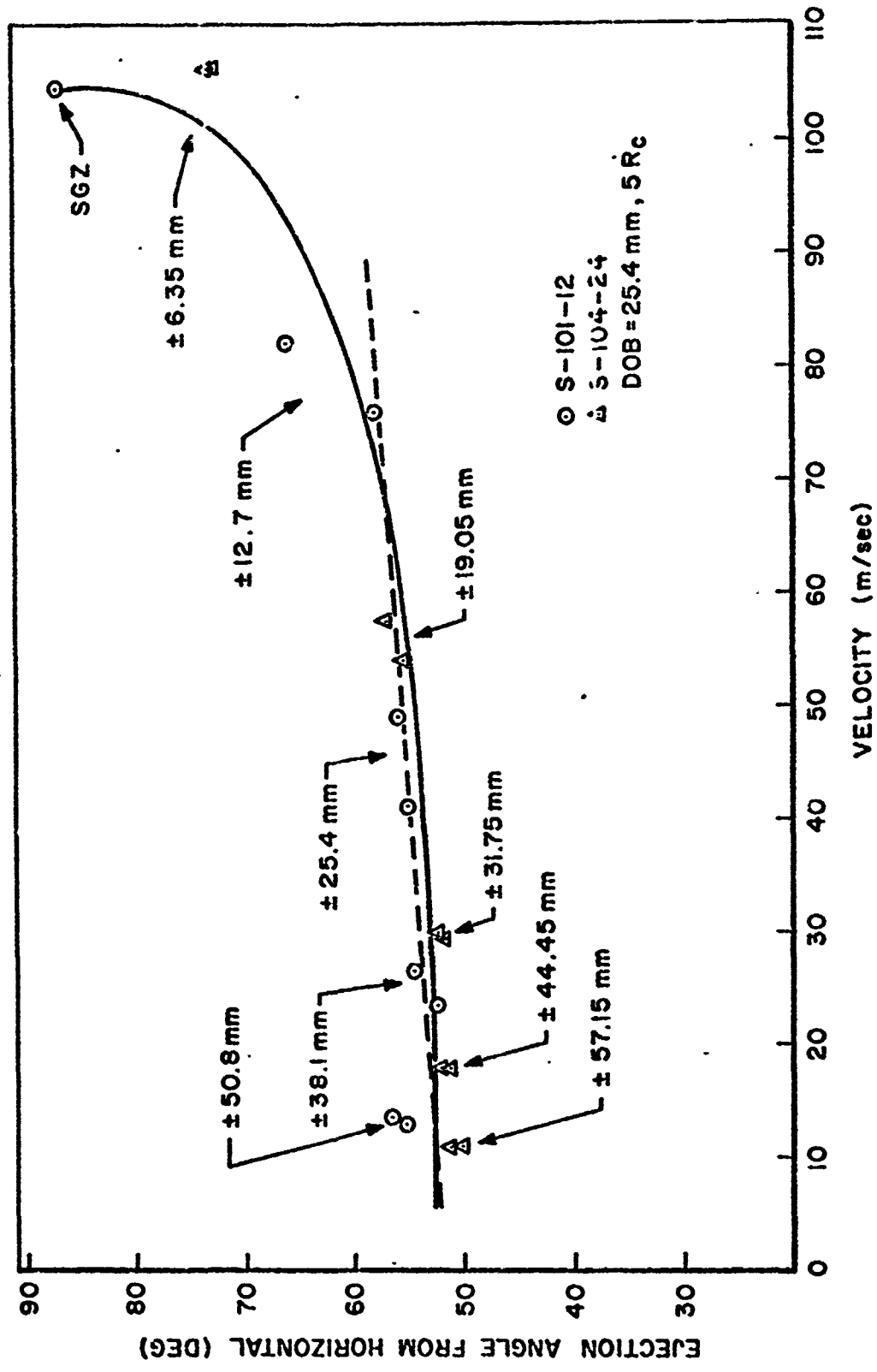


Figure 40. Ejection Angle vs. Particle Velocity for DOB of 25.4 mm

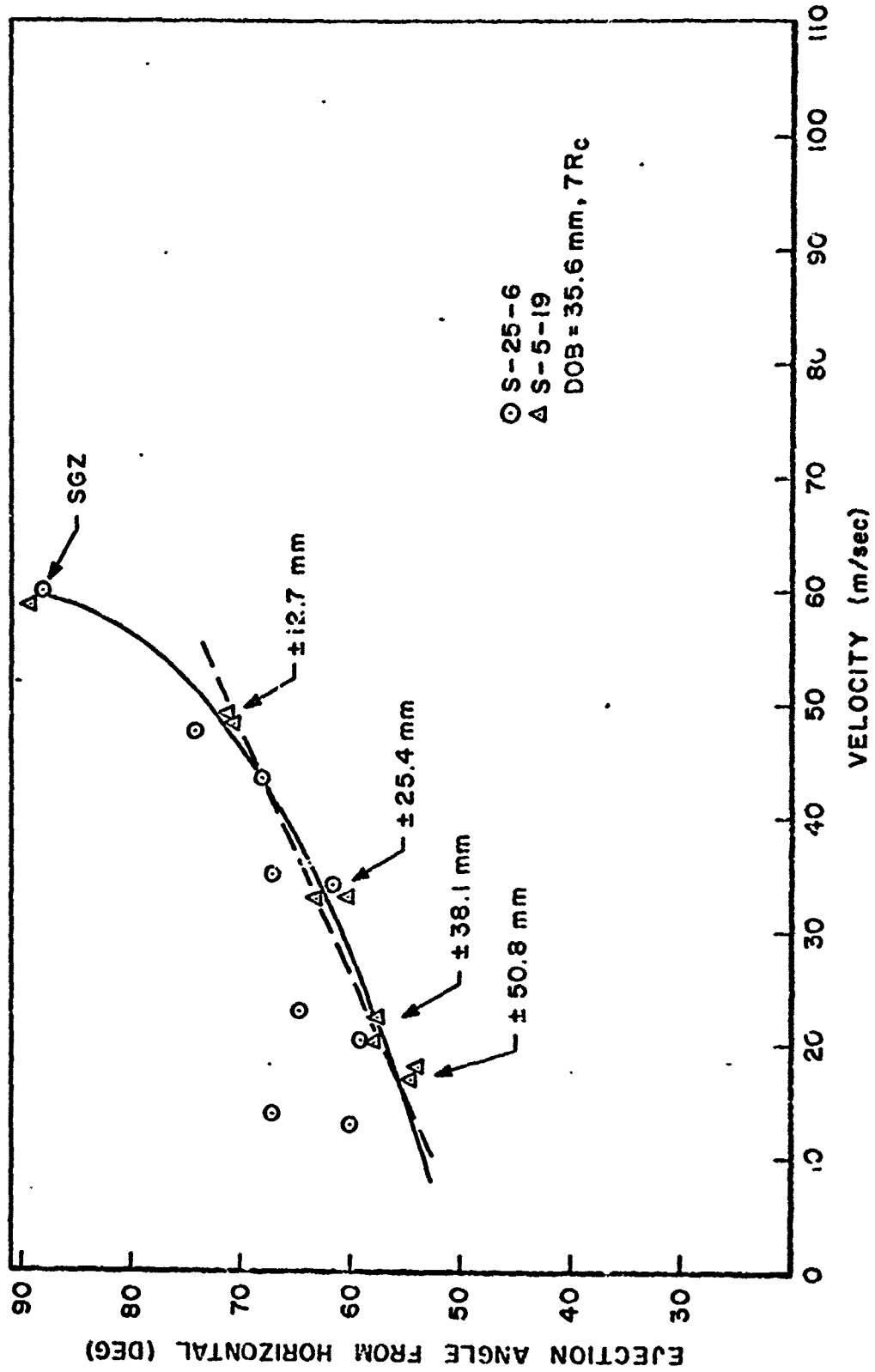


Figure 41. Ejection Angle vs. Particle Velocity for DOB of 35.6 mm

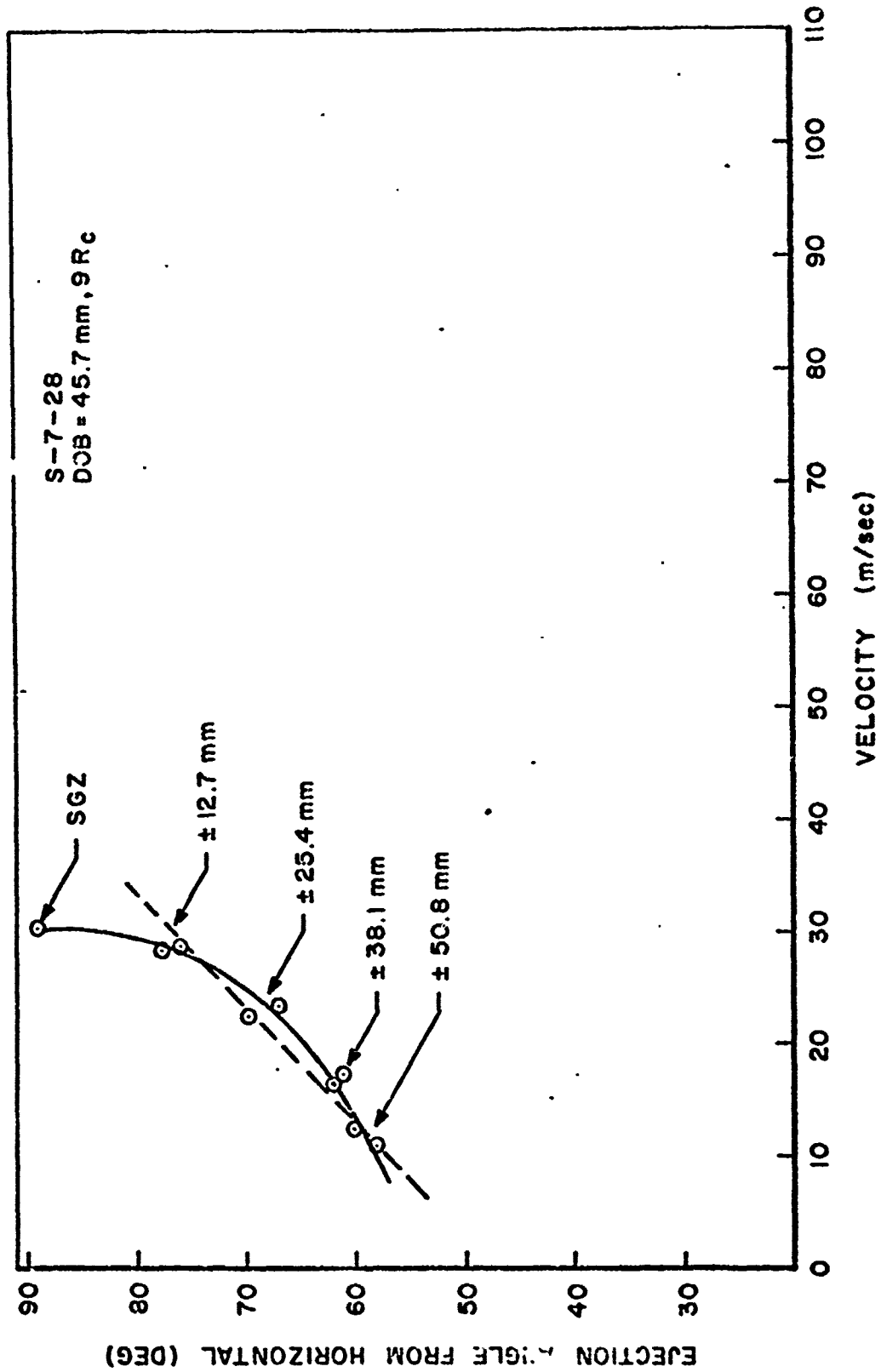


Figure 42. Ejection Angle vs. Particle Velocity for DOB of 45.7 mm

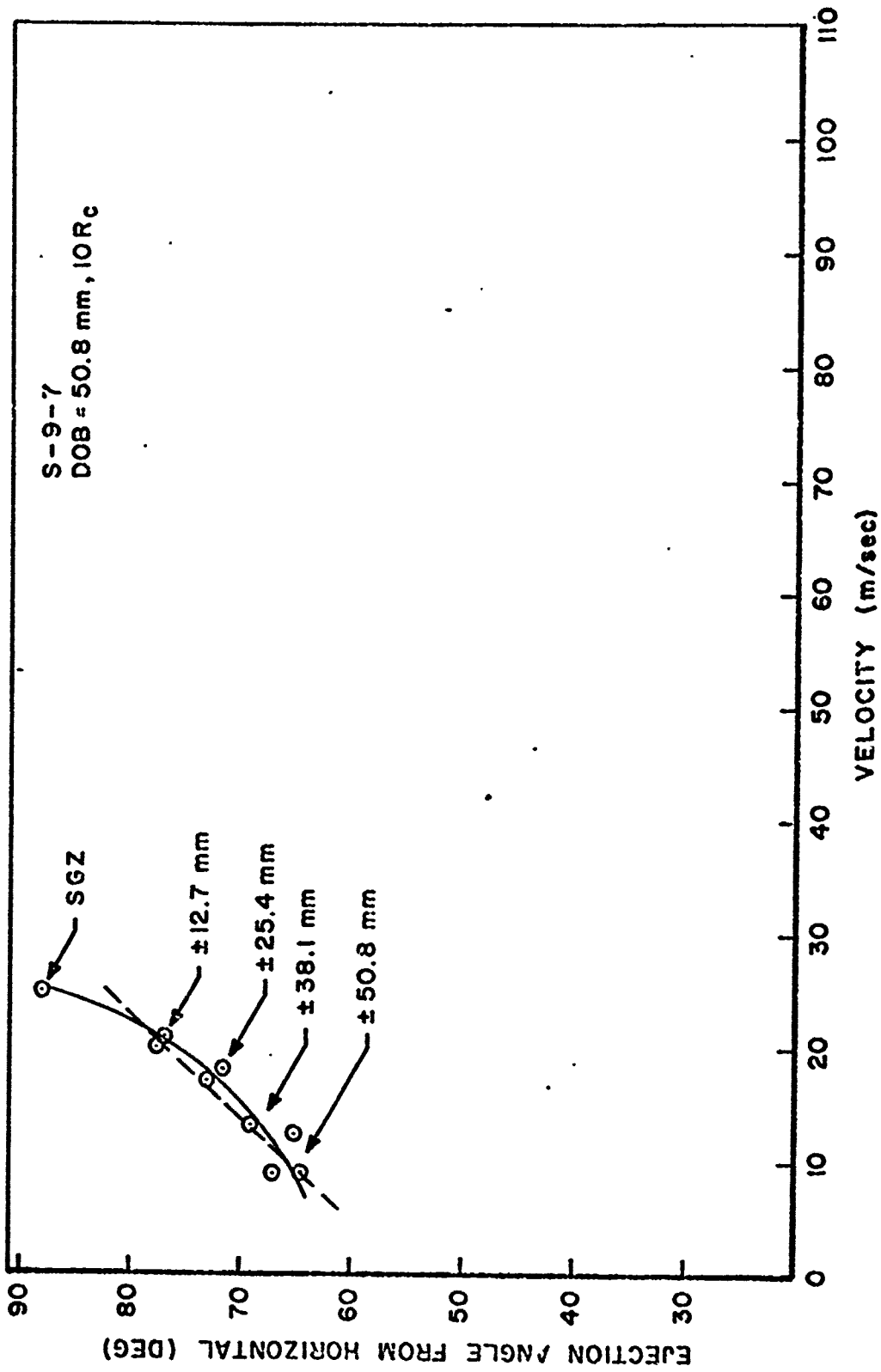


Figure 43. Ejection Angle vs. Particle Velocity for DOB of 50.8 mm

Appendix F

Graphs of Mound Growth for Shots at Depths

of Burst from 2.54 cm to 5.08 cm

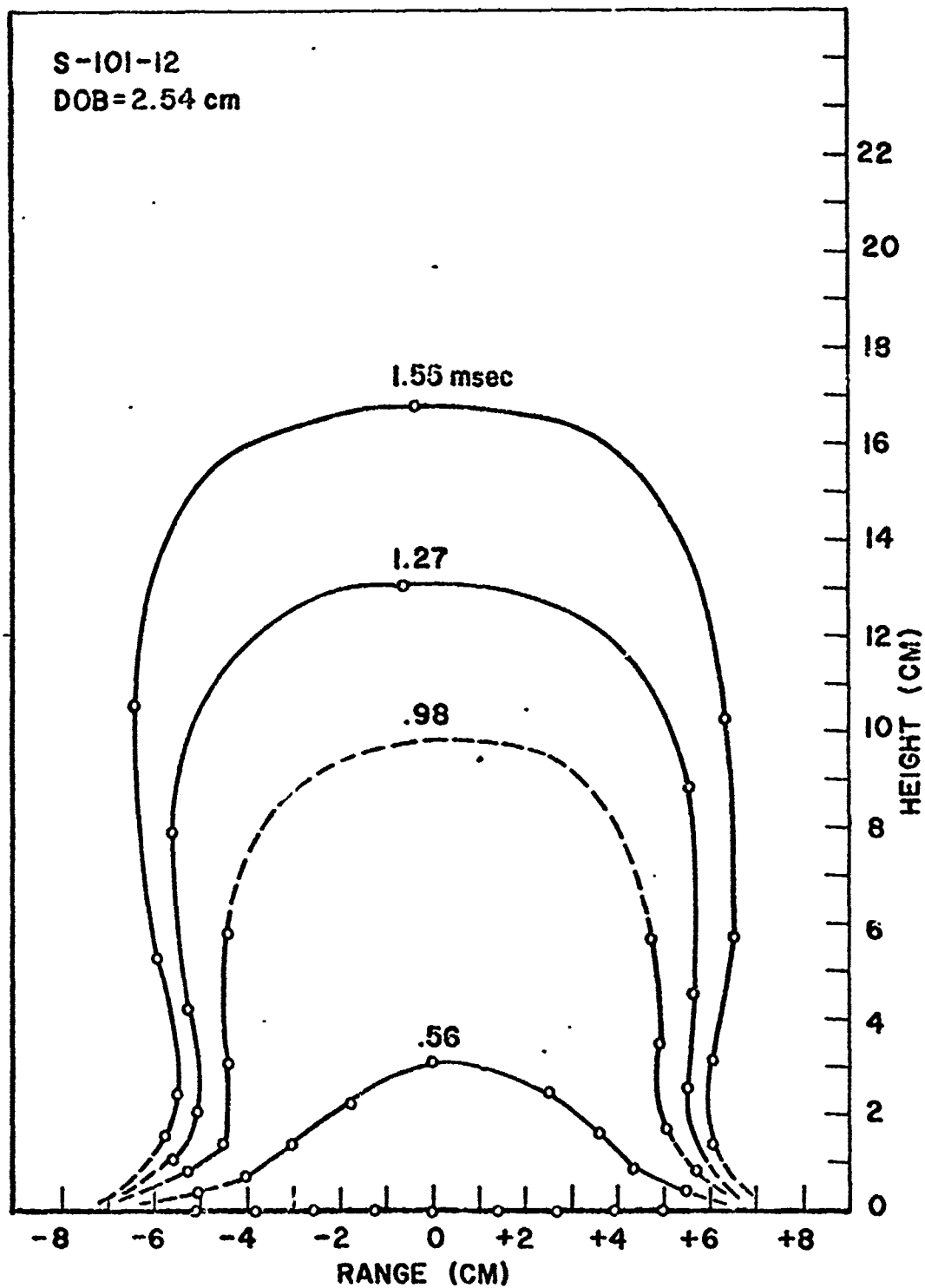


Figure 44. Mound Growth of Shot S-101-12

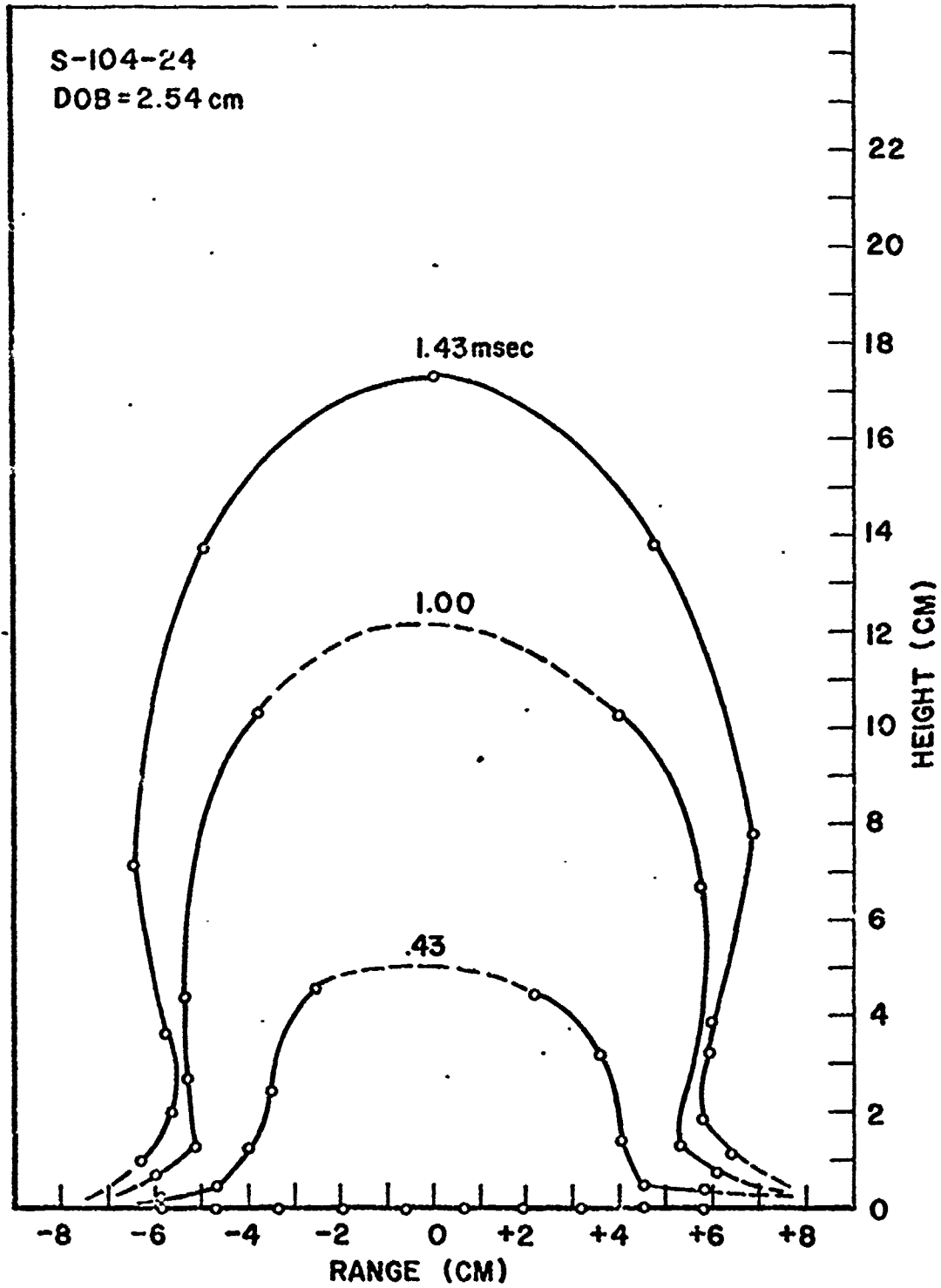


Figure 45. Mound Growth of Shot S-104-24

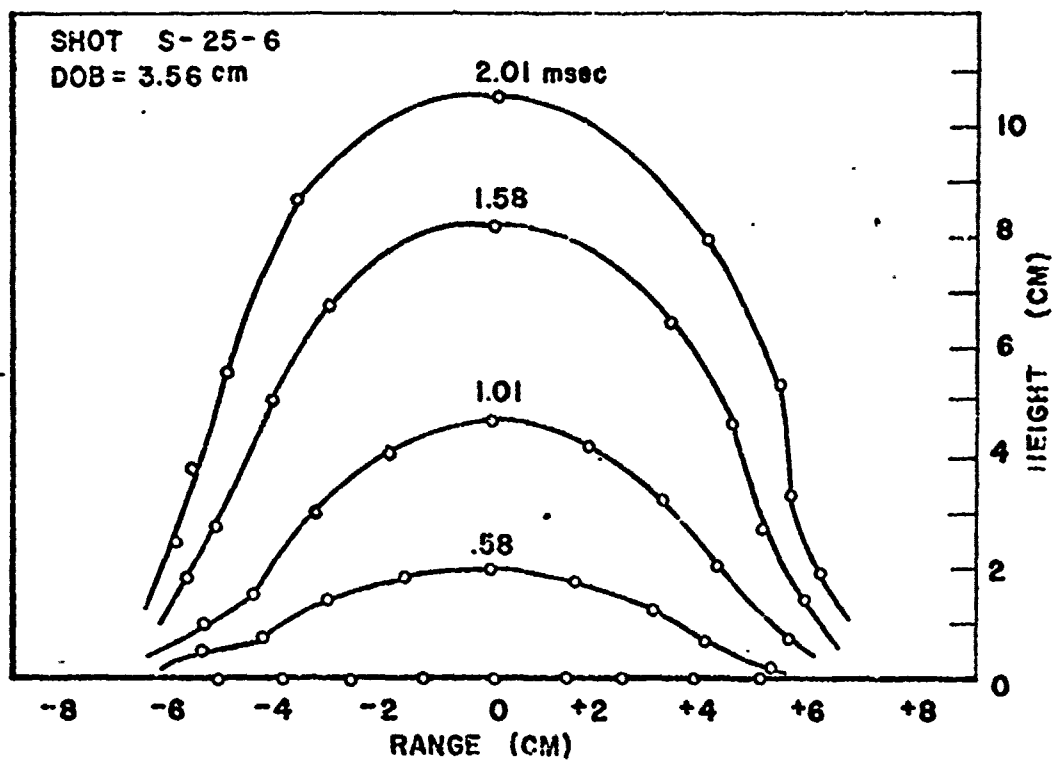


Figure 46. Mound Growth of Shot S-25-6

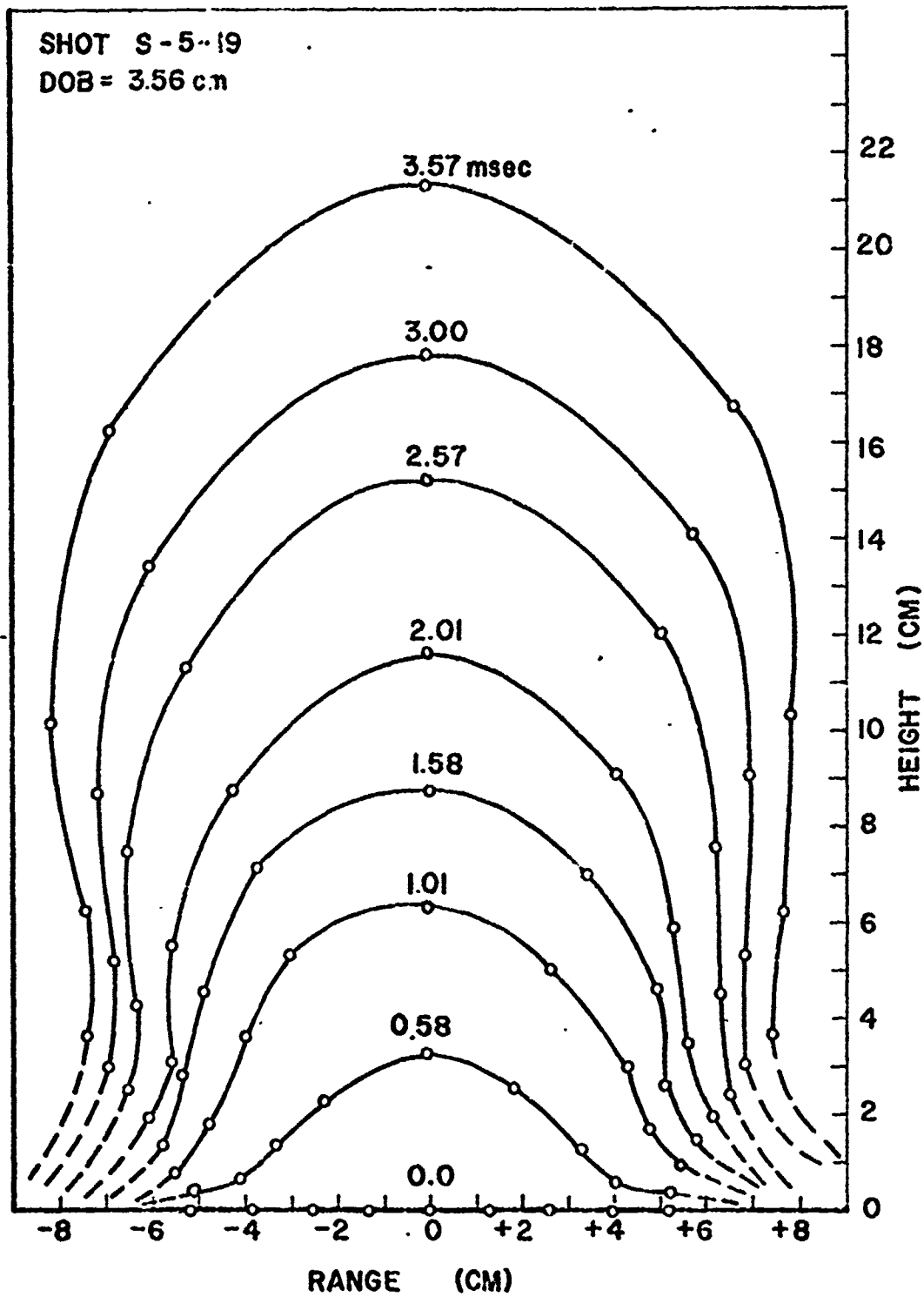


Figure 47. Mound Growth of Shot S-5-19

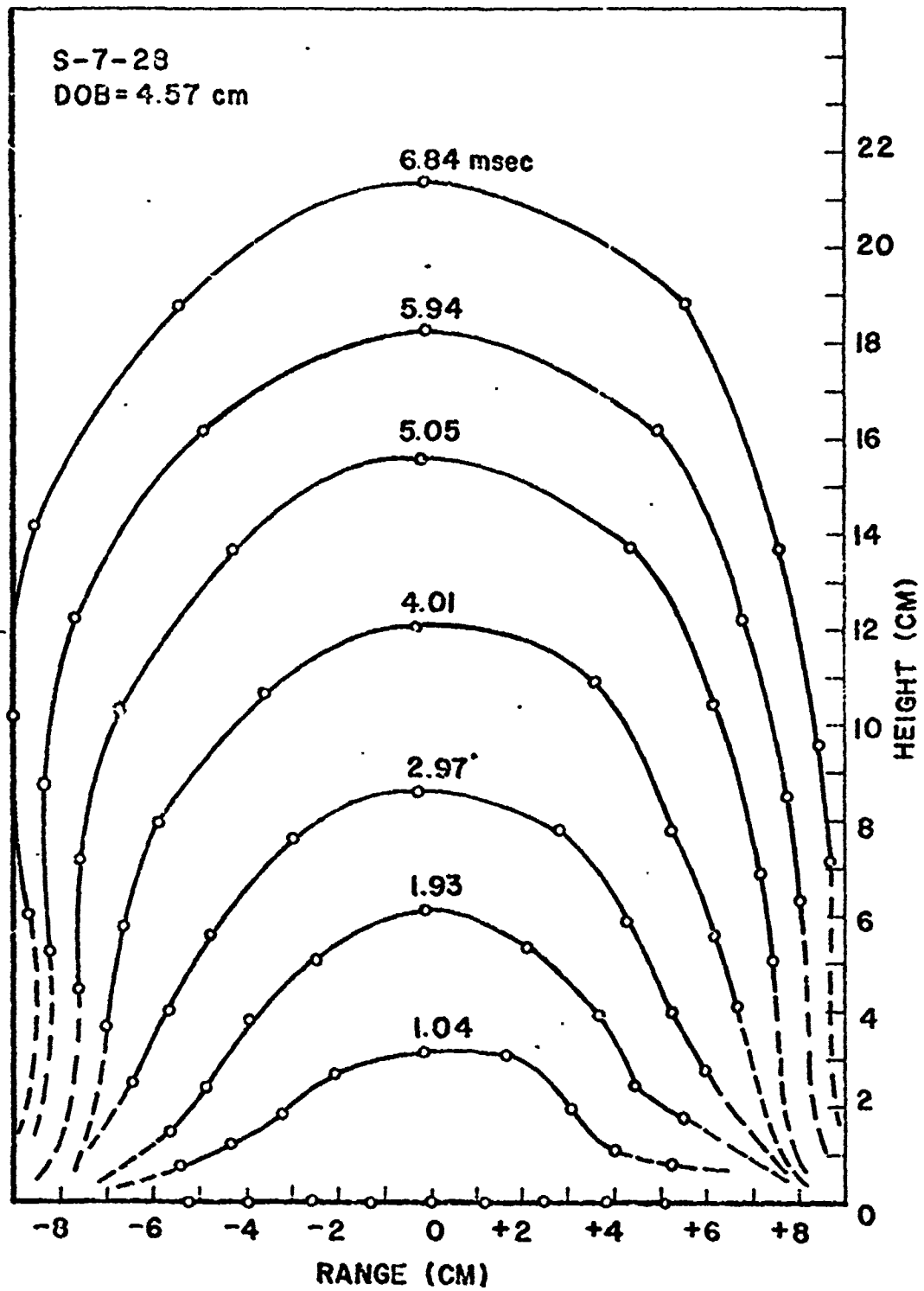


Figure 48. Mound Growth of Shot S-7-28

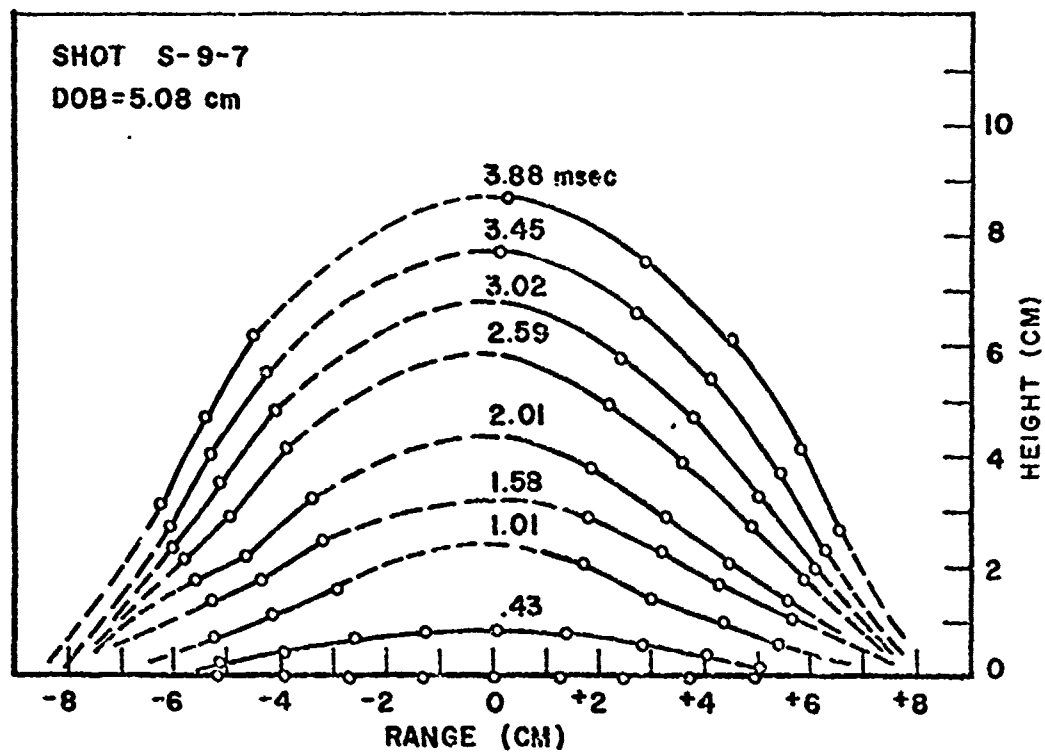


Figure 49. Mound Growth of Shot S-9-7

Vita

Floyd V. Kimberly was born on 30 August 1937 in McKeesport, Pennsylvania. He attended the public schools there and graduated from high school in June, 1955. He then attended the University of Pittsburgh where he received a Bachelor of Science degree in Civil Engineering and a commission in the United States Air Force in 1959. He entered active duty as a pilot trainee in January, 1960, and received his wings in March, 1961. For the next 8 years he was a KC-135 pilot and aircraft commander with the Strategic Air Command. During this time, he attended Squadron Officer's School at Maxwell Air Force Base, Alabama, and he also earned his Senior Pilot's Wings. In May, 1969, he went to Vietnam where he was an O-2B, Psychological Warfare Pilot and a Wing Commander's Executive Officer. Upon his return from Vietnam, he entered the Air Force Institute of Technology in June, 1970, in the Graduate Space Facilities Program.

Permanent address: 32A Crawford Village
McKeesport, Pennsylvania 15132

This thesis was typed by Mrs. Susan Peak.